3D *in situ* Chemical Synthesis: Additive Manufacturing of Functional Polymeric Materials via Vat Photopolymerization

Thesis by
Amylynn C. Chen

In Partial Fulfillment of the Requirements for the
Degree of
Doctor of Philosophy

Caltech

CALIFORNIA INSTITUTE OF TECHNOLOGY
Pasadena, California

2023
Defended July 14th, 2022

ACKNOWLEDGEMENTS

Thank you to my parents, Tina and Mike, for their continuous love and support.

ABSTRACT

As additive manufacturing gains popularity in rapid-prototyping, manufacturing, and customized production, there is a continuous demand in seeking new materials with advanced functionalities to satisfy the wide range of applications in aerospace, construction, optics, actuation, dentistry, biomedical practices, and even food industry. Vat photopolymerization (VP), a light-enabled AM technique, is particularly promising due to its ability to achieve good surface quality, high resolution, and large volumetric throughput. The vast majority of materials obtained by VP are covalently-crosslinked thermosets with nondegradable carbon backbones. This highly crosslinked polymer structure gives rise to stiff and brittle materials, limiting the structural functionality in desired applications.

This thesis explores a variety of polymer network structures for new VP photopolymers: a) dynamically-crosslinked compliant polymer, b) interpenetrating network (IPN) hydrogel, and c) covalently-crosslinked polymer with labile group (ex. ester) insertion to polymer backbone. With the dynamic crosslinking system, we demonstrate tunable mechanical behaviors of the metal-coordinated supramolecular polymers. These materials display a range of failure strain of 450%–940% and ultimate tensile strength (UTS) of 12.4–2.2 MPa with varying resin compositions. To incorporate multifunctionality, we design thermoresponsive IPN hydrogels by fabricating a hydrophilic host polymer network via VP and a subsequent formation a thermoresponsive 2nd network (poly(N-Isopropylacrylamide)). The architected IPNs consistently display strong polymer-liquid phase separation behavior and a tunable water release behavior with volumetric shrinkage between 30% and 70% upon heating at 50^{o}C. Finally, to promote the degradability of the acylate-based photoresin, we demonstrated successful incorporation for ester functional groups into the polymer backbone via radical ring opening polymerization of cyclic ketene acetals. The obtained polymer undergoes 84% mass loss within 7 hours under hydrolytic degradation condition. Overall, we demonstrated VP as a powerful technique to achieve one-pot synthesis and fabrication of functional materials. Our explorations on the development of degradable photopolymers, thermoresponsive double-network hydrogels, and metal-coordinated supramolecular polymers provide valuable insights into the impact of resin formulation on mechanical properties. From analyzing the molecular weight of 3DP materials to finetuning of phase separation behavior and degradability, we demonstrate that VP provides a new platform to inspire advanced photoresin design strategies for desirable mechanical performance.

PUBLISHED CONTENT AND CONTRIBUTIONS

[1] Amylynn C. Chen, Zane W. Taylor, Akash Dhawan, and Julia R. Greer. “Additive manufacturing enabled thermally responsive double network hydrogels (*In preparation*).” 2022.

Contributions: A.C.C. conceptualized the project, developed the photoresin chemistry, fabricated samples, characterized the samples, designed and conducted experiments, analyzed the data, and wrote the manuscript.

[2] Amylynn C. Chen, Widianto P. Moestopo, Zane W. Taylor, Seola Lee, Daryl W. Yee, and Julia R. Greer. “Vat polymerization of compliant and tough metal-coordinated polymers with tunable mechanical properties (*In preparation*).” 2022.

Contributions: A.C.C. participated in the conception of the project, developed the photoresin chemistry, fabricated samples, characterized the samples, designed and conducted experiments, analyzed the data, and wrote the manuscript.

[3] Hengyi Lu, Wen Shi, James H. Zhang, Amylynn C. Chen, Weixin Guan, Chuxin Lei, Julia R. Greer, Svetlana V. Boriskina, and Guihua Yu. “Tailoring the desorption behavior of hygroscopic gels for atmospheric water harvesting in arid climates (*Submitted*).” 2022.

Contributions: A.C.C. participated in the conception of the project and development of the polymer system.

TABLE OF CONTENTS

LIST OF ILLUSTRATIONS

LIST OF TABLES

NOMENCLATURE

3DP. 3D Printed or 3D Printing.

AA. Acrylic Acid.

AM. Additive Manufacturing.

AWH. Atmosphere Water Harvesting.

CAD. Computer Aid Design.

CGP. Chain growth polymerization.

CKA. Cyclic Ketene Acetal.

DLP. Digital Light Processing.

DMD. Digital Micro-mirror Device.

DMF. Dimethylformamide.

DSC. Differential Scanning Calorimetry.

FRP. Free radical polymerization.

IPN. Interpenetrating Polymer Networks with PNIPAM.

LCD. Liquid Crystal Display.

LCST. Lower Critical Solution Temperature.

MA. Methacrylate.

MDO. 2-Methylene-1,3-Dioxepane.

MPDL. 2-Methylene-4-Phenyl-1,3-Dioxolane.

MPEC. Metallo-polyeletrolyte Complex.

MW. Molecular Weight.

OMP. Olefin Metathesis Polymerization.

PμSL. Projection Micro-stereolithography.

PAA. Polyacrylic Acid.

PINPAM. Poly(N-isopropylacrylamide.

PLA. Polylactide.

rROP.	Radical Ring Opening Polymerization.
SA.	Sodium Acrylate.
SLA.	Stereolithography.
TGA.	Thermogravimetric Analysis.
UCST.	Upper Critical Solution Temperature.
UTS.	Ultimate Tensile Strength.
VAc.	Vinyl Acetate.
VP.	Vat Photopolymerization.

Chapter 1

INTRODUCTION

1.1 Overview on Additive Manufacturing

Additive Manufacturing, also known as three-dimensional printing (3DP) or rapid prototyping, is a technology that is used to create 3D objects from computer-aided designs (CADs) in a layer-by-layer fashion without the need for molding or machining. As AM gains popularity in rapid-prototyping, manufacturing, and customized production, there is a continuous demand in seeking new materials with advanced functionalities to satisfy the wide range of applications in aerospace, construction, optics, actuation, dentistry, biomedical practices, and even food industry. [1–5]

AM technologies can be categorized in terms of the energy source used for material binding during printing, such as laser, electron beam, heated nozzle, or UV light. To ensure sufficient melting and sintering, it is essential for the feedstock materials to have good thermal conductivity to attain good quality parts and sustainable energy input. Another way to categorize AM technologies is through the sizes of feedstock material. As shown in Table 1.1, the six technologies listed are roughly in the order of decreasing feedstock size, which goes from sheets though filaments, powders, droplets of viscous solutions to liquid resin. There is a correlation between the feedstock size and the feature size obtained by these technique. Due to flowability, size distribution of particles, and particle aggregation, the feature size is often expected to be even bigger than the size of the feedstock.

Laminated Object Manufacturing (LOM) uses sheet materials supplied by rolls, which are coated with suitable adhesives just before bonding to ensure effective bonding of two sheets of materials. The 3D objects are fabricated through a process called consecutive lamination in LOM, which is achieved using a laser beam to cut a 2D profile with cutting depth being the same as the feedstock layer thickness, to eliminate the destruction of the previously laminated layers. [6]

Direct Energy Deposition (DED) is an AM technique that directs the energy source; it is usually a laser or electron beam to focus on designated areas to heat and/or melt the feedstock materials (commonly powders made of metals, ceramics, or polymers) as they are being deposited.

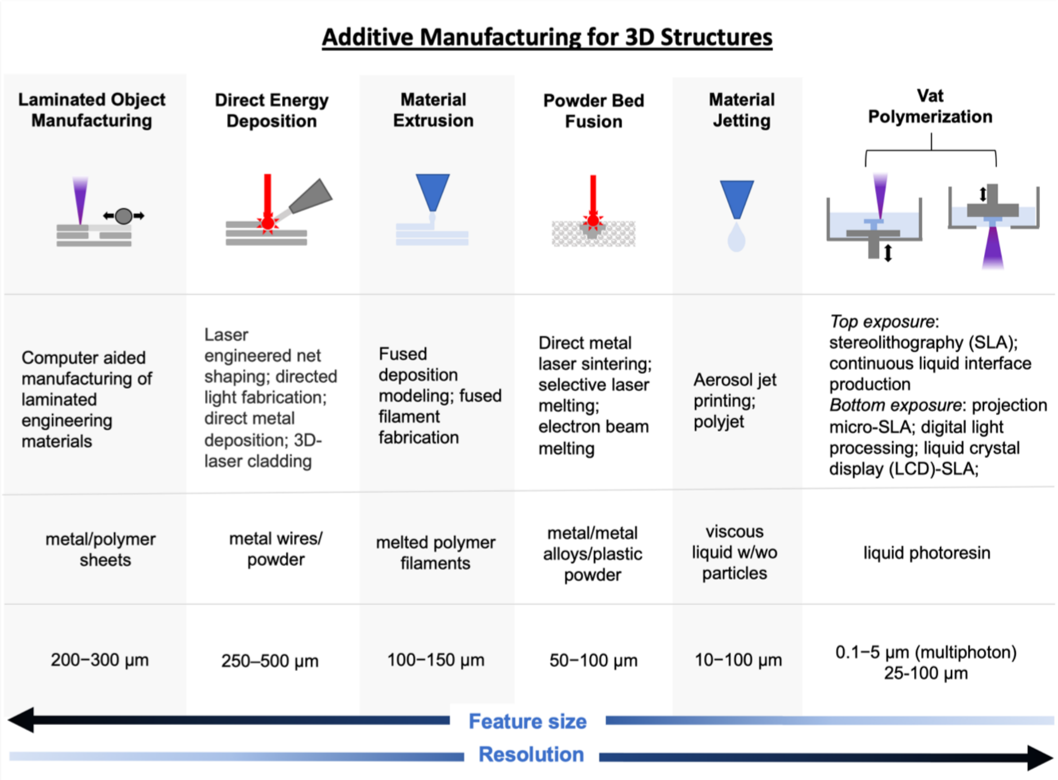

Additive Manufacturing for 3D Structures

Laminated Object Manufacturing	Direct Energy Deposition	Material Extrusion	Powder Bed Fusion	Material Jetting	Vat Polymerization
Computer aided manufacturing of laminated engineering materials	Laser engineered net shaping; directed light fabrication; direct metal deposition; 3D-laser cladding	Fused deposition modeling; fused filament fabrication	Direct metal laser sintering; selective laser melting; electron beam melting	Aerosol jet printing; polyjet	*Top exposure*: stereolithography (SLA); continuous liquid interface production *Bottom exposure*: projection micro-SLA; digital light processing; liquid crystal display (LCD)-SLA;
metal/polymer sheets	metal wires/ powder	melted polymer filaments	metal/metal alloys/plastic powder	viscous liquid w/wo particles	liquid photoresin
200–300 μm	250–500 μm	100–150 μm	50–100 μm	10–100 μm	0.1–5 μm (multiphoton) 25-100 μm

← Feature size

Resolution →

Table 1.1: Table of various additive manufacturing techniques and their minimum feature sizes.

Powder Bed Fusion (PBF) is another AM technique that utilizes thermal energy (laser or electron beam); it selectively melts or/and fuses powered materials in a metallic powder bed and constructs solid 3D objects layer by layer. Similar to DED, PBF requires the constituent of feedstock material to have good thermal conductivity for the energy source to enable sufficient melting and fusing to form solid parts. Poor thermal conductivity of the feedstock material would not only require more energy input, but it also becomes more challenging to control on the feature size and surface morphology.

Material Extrusion (ME) deposits a continuous filament of composite or thermoplastic material through a heated extruding nozzle to a platform to build solid parts layer by layer.

Material Jetting (MJ) is an AM process similar to ME that extrudes feedstock from nozzles. Operating in a similar fashion to 2D printers, MJ dispenses droplets of a photosensitive material through a nozzle, which can be solidified under ultraviolet (UV) light, constructing a part layer-by-layer. The materials used in MJ are thermoset photopolymers (acrylics) that come in a liquid form. Without the support of the power bed as mentioned for DED and PBF, MJ requires viscosity of the feedstock to be carefully optimized to achieve flow and ensure structural integrity before the UV curing procedure to solidify the entire structure.

All of the feedstock materials for these AM techniques mentioned above require some degree of processing. It can be energy intensive to process the fine and high purity power or wires for printing. The materials obtained by 3D printing techniques are limited by the available feedstocks. Moreover, many of these techniques also face challenges when printing very complicated 3D geometries, such as overhanging features or horizontal beams; some of the obtained structures are characterized as 2D or 2.5D. In the next section, I will discuss more in depth the last techniques in Table 1.1, vat polymerization. Different from the above-mentioned AM techniques, the size of the feedstock is no longer a constraint on the fabricated feature size; the high-resolution 3D printing process can be realized through localized photopolymerization that precisely turns liquid polymer resin into solid materials. Since all the projects in my thesis are realized by VP processes, I will dedicate the following section to discuss it in depth.

1.2 Vat Photopolymerization

Vat photopolymerization (VP), 3D photopolymerization or resin 3D printing, is an AM technique that cures liquid resin into solid polymers with complex 3D structures enabled by computer-aided designs (CADs).[7] Unlike other AM processes where the minimum feature size and the overall geometry and resolution of the 3D printed (3DP) parts are often limited by the combination of the size of feedstock materials and the energy source for material binding, VP is capable of fabricating a wide range of functional materials and enables prints with complex 3D design, smooth surface finish, high volumetric throughput, fast printing speed as well as sub-micron feature size.[8–11] Vat polymerization technologies can be divided into different categories depending on the light source employed on the printer: stereolithography, digital light processing, and liquid crystal display-based 3D printing.

Stereolithography (SLA) or laser SLA is one of the earliest VP techniques, where a rastering UV laser controlled by a scanning mirror coupled with a galvanometer moves across the plane to induce spatial photopolymerization of the desired 2D pattern (Figure 1.1a). Such scanning laser mechanism results a slow printing process as the UV beam locally photopolymerizes the polymer resin based on point-light-source illumination. [12]

Digital light processing (DLP) employs a digital micromirror device (DMD) to provide a dynamic mask that allows for the rapid photopolymerization of an entire patterned layer upon UV illumination (Figure 1.1b). Once the pattern is formed, the stage drops the structure by a predefined layer thickness, and the DMD reconfigures itself to display the image to be projected onto the next layer until the structure is complete. There have been many recent advancements on DLP-based 3D printing techniques, including projection micro-stereolithography (PμSL) for high resolution printing (up to 0.6 μm) and continuous liquid interface production (CLIP) for fast-speed 3D printing (1000 mm h^{-1} in the z-direction).[13–15] Compared to laser-SLA, DLP enables high resolution printing with fast speed and high volumetric throughput since it can pattern an entire plane simultaneously. [11]

Liquid crystal display (LCD)-based 3D printing or LCD-SLA is a cost-effective alternative to DLP and the main difference exists in the light source to cure photopolymer resins. Instead of a complicated and costly DMD, it employs an inexpensive monochromatic LCD where the UV light of a specific wavelength transports through LCD, selectively projects on the surface of the liquid photosensitive resin, and then initiates the photopolymerization reaction.[16] The feature size of LCD-SLA printing is determined by the pixel size of the LCD (35-50μm).[17, 18] Taking advantage of the advanced LCD technology, LCD-SLA is recognized for its high resolution and cost effectiveness and has become a popular technique for mass manufacturing of large and detailed functional parts.

In comparison to laser/electron-beam melting and heated extrusion-based AM technologies, VP consumes less energy, is compatible with customized photoresin, enables prints with complex geometries and smooth surface finish, and can be quite cost effective considering the printer cost and reusability of the feedstock resin. All of this help VP to become a more widely-used prototyping and even mass manufacturing method. It is more pressing than ever to search for new novel polymers for VP for a broader range of applications.

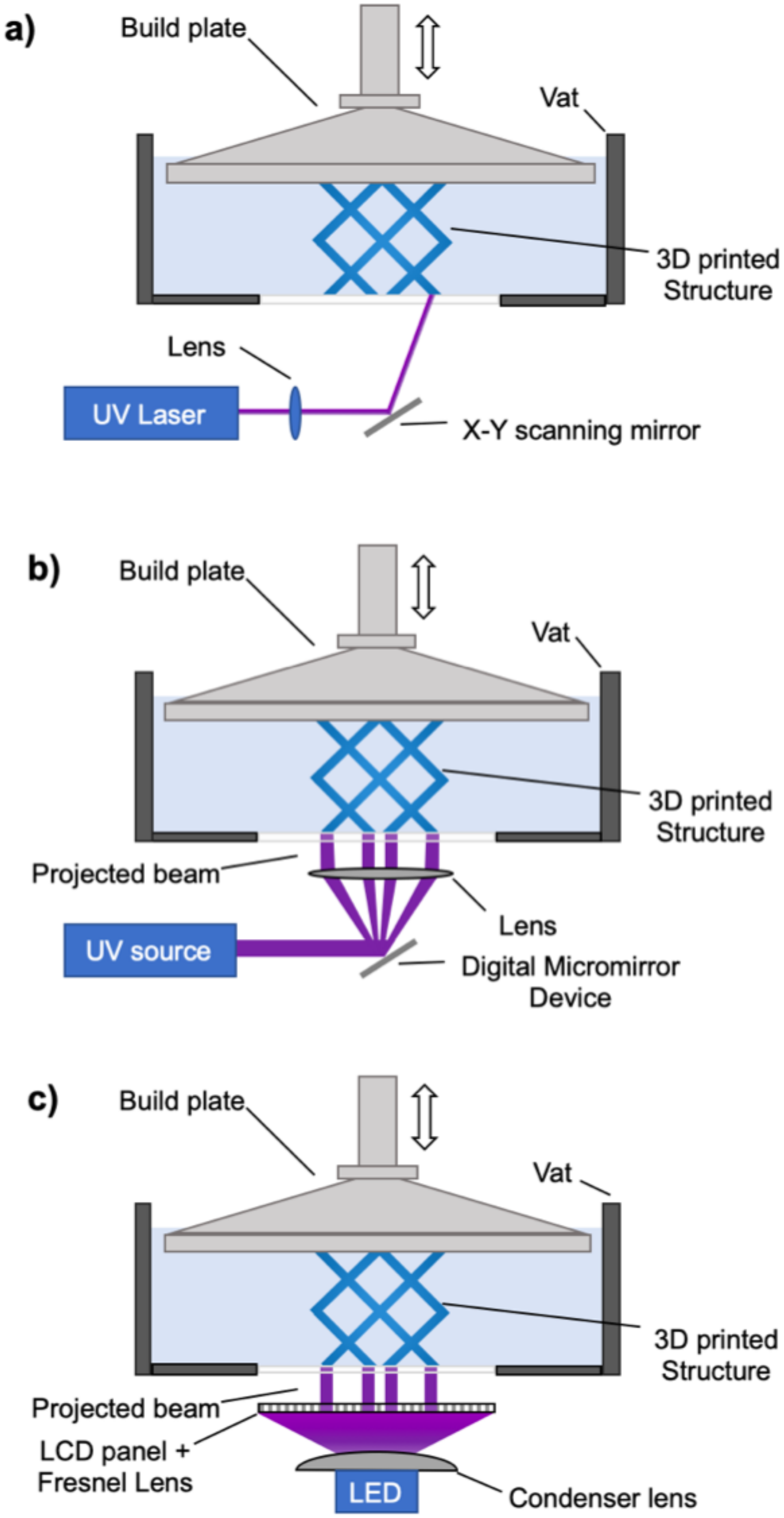

Figure 1.1: Schematics of different categories of vat polymerization techniques: a) laser stereolithography, b) digital light processing, and c) LCD-based 3D printing.[10]

1.2.1 State-of-the-art Photopolymers for VP

Most 3D printable photopolymers are thermosetting polymers or thermosets, which are a class of polymers that are insoluble and nonmelting. Currently, some commercially available UV curable elastomers can consistently reach moderate failure strain 160%–220% and ultimate tensile strength ranging from 0.8–3.3 MPa with absence of mechanical tunability (Figure 1.2, data [a]).[19, 20] Another one of the widely-used commercially available photoresins made by Autodesk Inc is PR48 standard clear resin. This multifunctionalized acrylate-based resin enables polymeric material that is decently stiff but extremely brittle with a failure strain of 5% (Figure 1.2, data [b]). [21] A recent research development demonstrates that a tunable elastomeric system consists of commercially available components, aliphatic urethane diacrylate and epoxy aliphatic acrylate. The fabrication using VP is achieved with the assistance of a heated vat to overcome the processing issue from the highly viscous resins; the obtained material shows elongation at breakage of approximately 240-1100% and UTS of 0.5–7.5 MPa (Figure 1.2, data [d]).[22] Although this work demonstrates that some commercially available photopolymers show great compliance, it is not very useful for researchers in academia without knowing the exact chemical structures of material for further improvement and research development. To broaden the material choices for AM, there is a continuous search for new materials, particularly functional materials that exhibit properties such as high strength and high compliance, stimuli responsiveness, degradability, and recyclablility, to accommodate the rapid growth of AM technology in the medical, dental, and engineering fields.

1.3 Polymer Molecular Structures Enabled by VP

Traditional polymer synthesis can be quite an involved process including, but not limited to, heating to speed up the reaction, refluxing to trap volatile organic precursor molecules, cooling to quench the reaction, removing solvents using a heated device like rotary evaporator, and finally purifying several times to get the polymer products. Though such processes give rise to pure materials for accurate characterization of the material of interest, often time it is challenging to bring these materials to use due to cost, processing time, sensitivity to reaction conditions, and other limitations for scaling up. As a result, the properties of the material made in small batches do not match the ones made in bulk.

VP-based 3D printing techniques provide a new path for material scientists, chemists and researchers with different backgrounds to create and discover new and novel

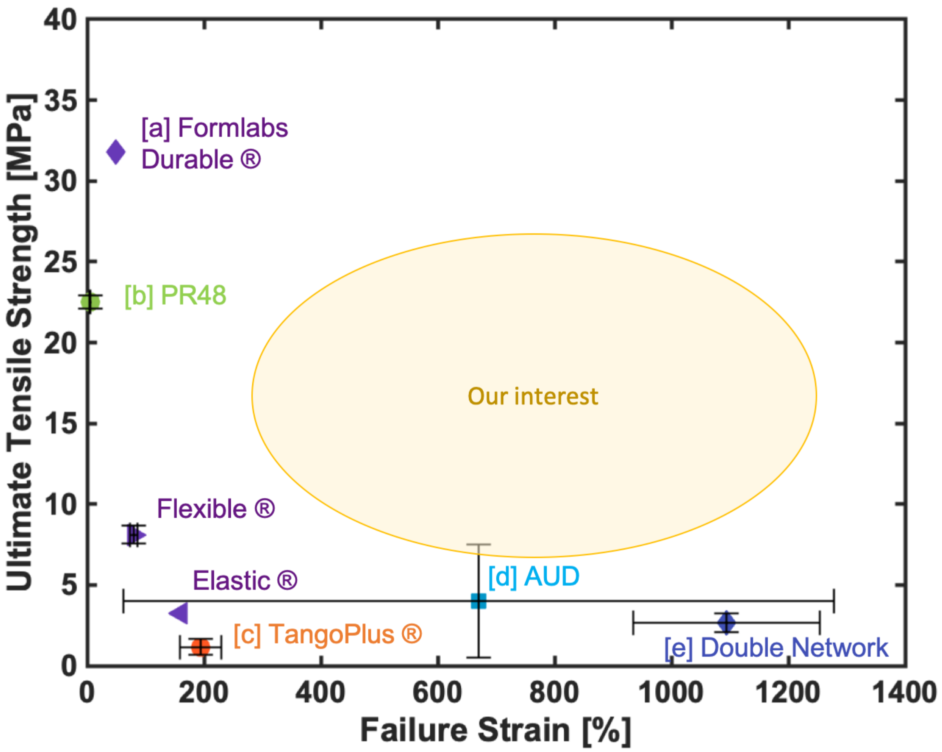

Figure 1.2: Ultimate tensile strength and failure strain of state-of-the-art photopolymers obtained by vat polymerization.[23]

materials by varying composition, optimizing processing parameters, and characterizing material properties to obtain desirable performance. Despite the light source used in the VP-based 3D printers, they all undergo a similar printing process. As illustrated in Figure 1.3, the gap between the interface of the printed structure and liquid resin and an illuminated pixel enabled by the light source is where the ’magic’ of vat polymerization happens, which is called a voxel in 3D printing. Within the voxel, the photochemical components of the resin can generate reactive species to kickstart the polymerization process from liquid resin to solidified voxels. At the start of each layer of printing in a VP process, the buildhead with previously printed object would move down towards the vat window until a preset distance is reached. This preset distance determines the thickness, which is usually on the order of the tens of microns. Upon the buildhead reaching the designated position, the light source would illuminate at certain pixels to create 3D printing voxels where photopolymerization occurs to form a solid layer. The buildhead then moves up to separate the printed layer from the vat window. As the liquid resin recoats the vat window, the buildhead would proceed to move back down to repeat the process to

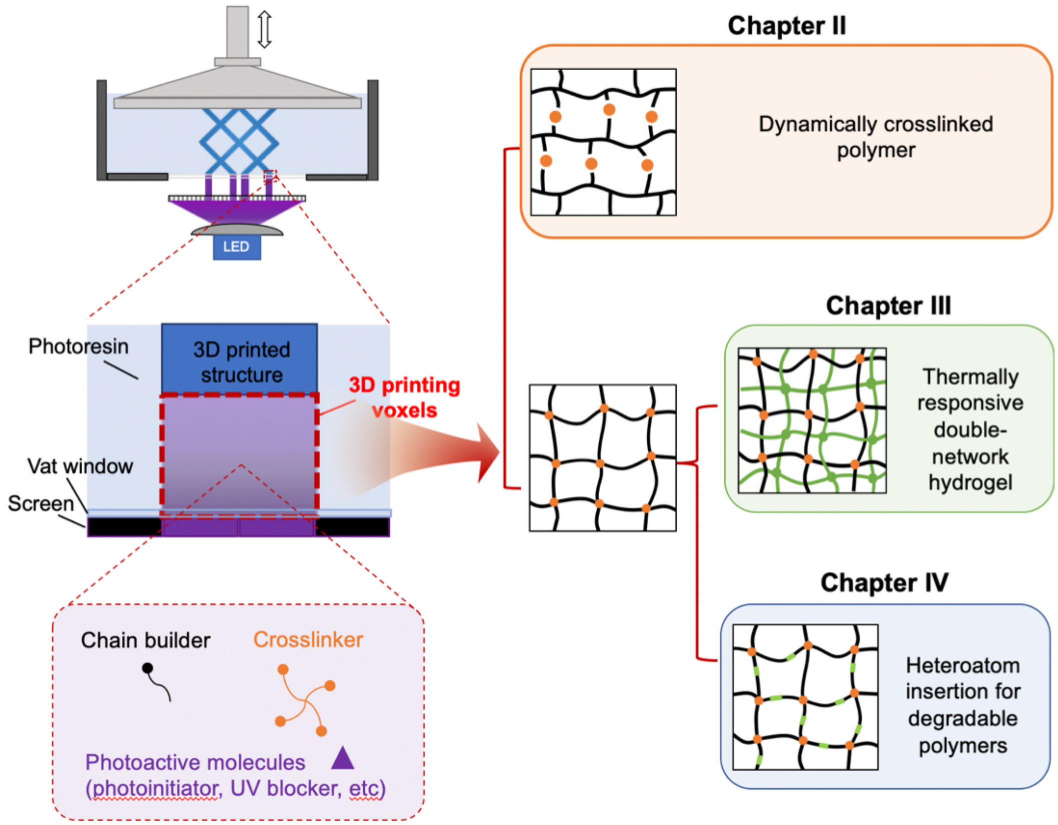

Figure 1.3: VP-enabled Molecular Structures and Thesis Outline.

form the subsequent layer.

My Ph.D. thesis consists of three projects which are discussed in great details in the following chapters. All projects focus on fabricating new functional materials using VP-based 3D printing techniques, but fundamentally the three projects differ in the molecular structures of materials being synthesized *in situ* during the printing process.

The majority of photopolymers enabled by VP-based techniques are covalent crosslinked acrylic or expoxy resins that are stiff and brittle and have poor degradability. In Chapter 2, I will introduce a dynamically crosslinked material via electrostatic interactions that exhibits high compliance and high toughness, as well as mechanical tunability. For the next two chapters, I revisit to covalently crosslinked system and attempt to alter the material properties by introducing different functional monomers into the photoresin. For Chapter 3, I will discuss our efforts on 3D printing hydrophilic hydrogels as a host network for thermoresponsive polymer. The fragility of hydrogels poses a challenge for the layer by layer AM fabrication process, but resolving the problem could potentially introduce an entire class of new materials with mechanical properties in the kilopascal regime. Finally, to address the potential problems of new plastic wastes generated by the fast growing AM industry, Chapter 4 focuses on incorporating cyclic ketene acetal (CKA), a class of small cyclic molecules, into acrylic photoresins to introduce degradable functional groups to the polymer backbone and achieve complete degradation.

Chapter 2

ADDITIVE MANUFACTURING OF METAL-COORDINATED SUPRAMOLECULAR POLYMER WITH TUNABLE MECHANICAL PROPERTIES

Chapter Abstract

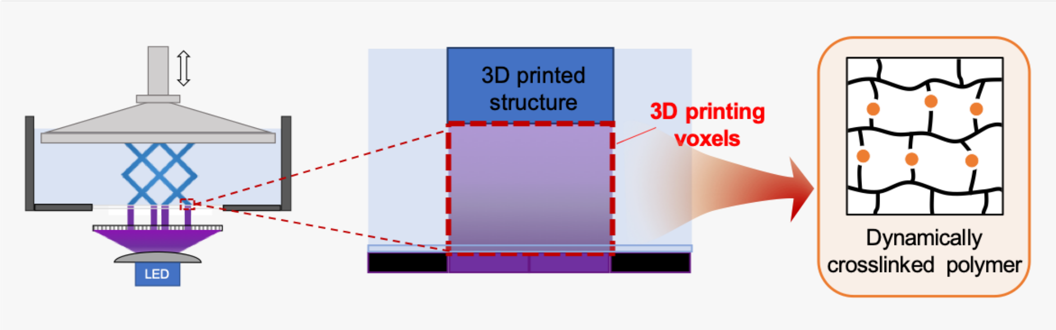

Figure 2.1: Schematic Overview of Chapter 2.

Most vat polymerization (VP)-based additive manufacturing techniques utilize acrylate-containing liquid photoresins and the resulted 3D-printed (3DP) polymers are highly crosslinked materials that are stiff and brittle. Although some recent developments have demonstrated promising resin formulations to obtain compliant materials, the lack of advanced functionalities, such as self-healing, stimuli responsiveness, and recyclability in such material systems, limits their potential applications. Metallo-polyelectrolyte complex (MPEC) is a class of smart material that consists of negatively charged polyanions crosslinked by metal cations via electrostatic interactions. In this work, we demonstrate a simple and inexpensive one-pot synthesis and fabrication of MPEC materials with complex geometry, submillimeter resolution, high printing speed, and tunable mechanical properties using a low-cost 3D printer ($300). After equilibrating in ambient conditions, the 3DP MPECs display a range of failure strain of 450%–940% and ultimate tensile strength of 12.4–2.2 MPa with varying resin compositions. This simple one-pot approach enables the fabrication of ambient-stable 3DP materials with high compliance and high toughness. Due to the supramolecular nature of MPEC, this system is also capable of providing valuable insights on the effect of resin formulation on the molecular

weight of 3DP materials, thus inspires advanced photoresin design strategies for desirable mechanical performance.

Adapted from:

Amylynn C. Chen et al. “Vat polymerization of compliant and tough metal-coordinated polymers with tunable mechanical properties (*In preparation*).” 2022.

2.1 Introduction

2.1.1 Compliant Materials for AM

The state-of-the-art photopolymer resins suitable for VP are generally multifunctional vinyl- or epoxy-based systems with high degrees of crosslinking that lead to the stiff and brittle 3DP polymers.[5] The vast expansion of VP in the mass manufacturing and mass customization (e.g. dental retainers and footwear) inspires academic and industrial researchers to develop new 3D printable elastomers. Currently, some commercially available UV-curable elastomers can consistently reach moderate failure strain of 160%–220% and UTS ranging from 0.8-3.3 MPa with absence of mechanical tunability.[19, 20] A recent research development demonstrates a tunable elastomeric system consisting of commercially available components, aliphatic urethane diacrylate, and epoxy aliphatic acrylate, fabricated via VP with the assistance of a heated vat to overcome the processing issue from the highly viscous resins; the obtained material shows elongation at breakage of approximately 240–1100% and UTS of 0.5–7.5 MPa.[22]

2.1.2 Metallo-polyeletrolyte Complex

As opposed to the conventional covalently-crosslinked photopolymers, metallo-polyelectrolyte complexes (MPECs) consist of negatively changed polymers also known as polyanions coordinated by electrostatic crosslinks via charged metal ions. MPECs are known to display mechanical compliance, self-healing, and stimuli responsivity which lead to their applications in soft-robotics, recyclable materials, reparable systems, sensors, electronics, and biomedical field.[24–26] The properties of MPECs arise from the dynamic nature of electrostatic and hydrogen bonds allowing MPECs to partially unravel, change configuration, and reform bonds that are once broken.

Generally, MPECs are synthesized via a two-step approach where the first step is the polyanion synthesis and the subsequent step involves submerging the polyanions in a metal cation solution to form the metal ion crosslinks. (Figure 2.2) The synthesized MPEC then requires to be further shaped and processed into functional parts or specimens for mechanical characterization. Previous works have described polyacrylic acid (PAA) -based systems crosslinked by divalent metal ions, trivalent metal ions, or insoluble metal salts to induce polymer gelation.[27–29] These systems are notable for their high compliance, plastic deformation and rapid self-healing at the hydrated state but require multistep processes that are unsuitable for VP. Using a similar multistep process, PAA-containing double network hydrogels coordinated by trivalent metal ions (Al^{3+} and Fe^{3+}) have been constructed with polysaccharide (carboxymethyl cellulose and sodium alginate) as the 2nd network; the obtained materials display a hydration-enabled higher strain (up to 1228%) and tensile strength (up to 3.24 MPa) upon equilibration in water which limits their application to aqueous environment, but show compatibility with direct ink writing 3D printing with subsequent UV irradiation treatment.[30–32]

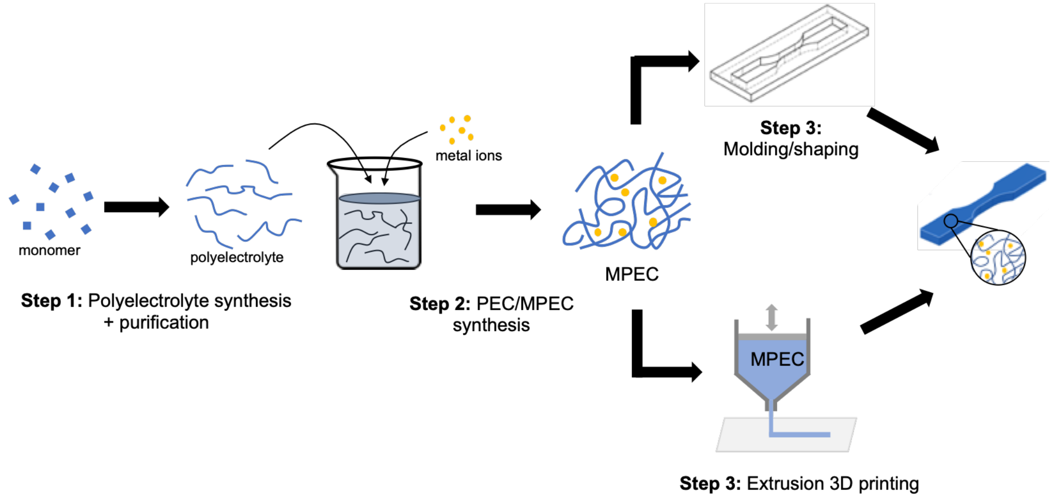

Figure 2.2: General steps involved in MPEC synthesis and fabrication into functional parts or mechanical testing specimens.

To the best of our knowledge, most MPECs generally are constructed in multi-step processes that not only are unsuitable for VP processes, but can also introduce inhomogeneities and diffusion limitations during production of these MPEC materials.[33] Such multistep processes also require a large material processing parameter space (e.g. time for equilibration step, metal ion solution concentration, and solvent evaporating during testing) likely to give rise to large sample-to-sample mechanical variability and poor mechanical stability. The necessity to equilibrating and storing in water adds challenges for MPEC to be fabricated into objects or parts that are useful and inert in ambient environment.[34]

To avoid these issues, we introduce a fast and simple *one-pot* approach to achieve *in situ* synthesis and fabrication of MPEC structures suitable for VP, where the 3DP MPECs demonstrate mechanical compliance, recoverability, as well as self-healing. We vary three aspects of the photoresin compositions: metal cation species, metal ion crosslinker concentration, and/or glycerol content, to investigate the effect of photoresin compositions on the tunability of the mechanical properties for our 3DP MPECs. The failure strain, ultimate tensile strength, strain rate dependency, cyclability, reproducibility, and self-healing of the 3DP MPECs are also examined. Most 3D printable photopolymer systems are designed for thermoset-based materials that are highly and irreversibly crosslinked. These materials are not suitable for studying the impact of polymer chain molecular weight on the mechanical properties. Because of its supramolecular nature, this MPEC system also provides us a unique gateway to understand the molecular weight of polymer chains on the mechanical properties in 3DP materials and offer valuable insights on optimization of photoresin design for additive manufacturing.

2.2 Fabrication and Chemical Characterization of MPEC

To investigate the effect of the photoresin formulation on the mechanical properties of 3D architected MPEC samples, particularly the stress and strain at failure, we developed twelve sets of resins where we systematically vary the metal cation species (e.g. Al^{3+} and Fe^{3+}), the relative metal ion crosslinker concentration, and the glycerol content (e.g. 5, 10 and 20 v/v%). We conducted D638 Standard V tensile testing on the 3DP MPEC specimens in ambient conditions to determine the UTS, strain to failure, and toughness. To further understand the impact of resin formulation on the molecular weight of 3DP MPECs, thus the overall mechanical properties of the printed samples, we performed rheological measurements of the dissolved MPECs samples to study the relative molecular weight of the polyanions.

2.2.1 Photoresin Development

Developing a 3D printable resin for *in situ* photopolymerization requires an appropriate balance between the chain building monomers for constructing the polymer network and photoactive components for enabling an efficient printing process with considerations of the resin viscosity and shelf-life.[5, 35] We formulate a resin that consists of co-monomers acrylic acid (AA) and sodium acrylate (SA) as chain

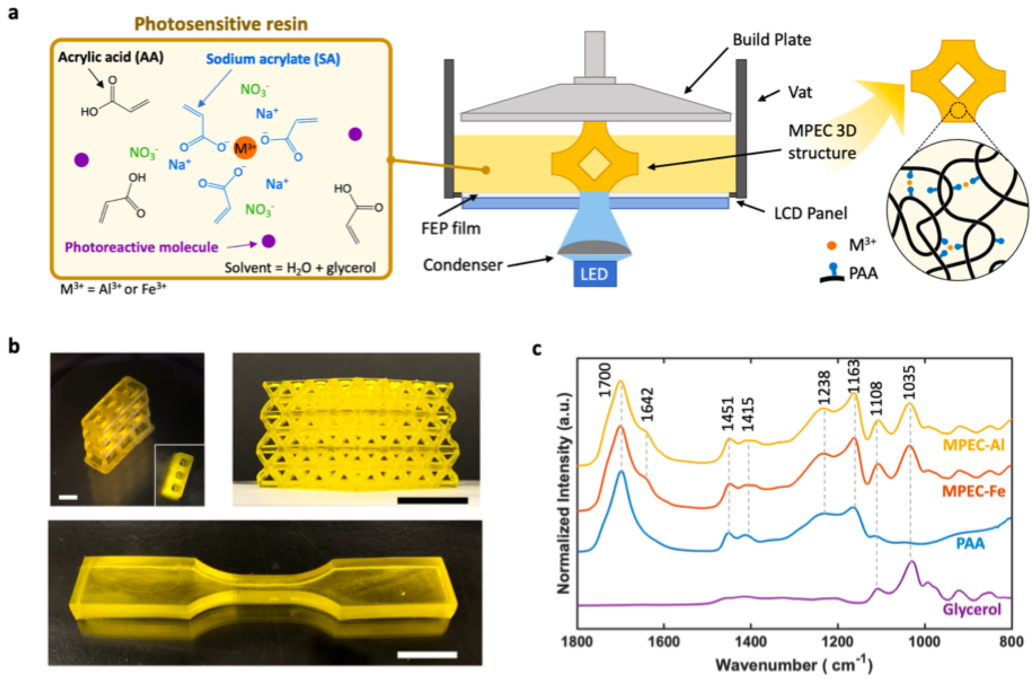

Figure 2.3: Schematics of MPEC fabrication and chemical characterization. a) Chemical composition of photoresin and schematics of liquid crystal display (LCD) stereolithography (SLA). b) Optical images of architected samples. Scan bars are 1mm (top left) and 5mm (rest). c) ATR (Attenuated Total Reflectance) FTIR spectra of 3DP aluminum ion-containing MPEC (MPEC-Al), the ferric ion-containing MPEC (MPEC-Fe), polyacrylic acid (PAA), and glycerol.

builders, the trivalent metal ion species as crosslinkers, and photoreactive molecules such as ethyl phenyl (2,4,5-trimethylbenzoyl) phosphonate as the photoinitiator and tartrazine as the UV blocker; all are dissolved in glycerol and water (Figure 2.3). While keeping the metal ion to SA mole ratio to be 1:3 as well as constant molarities of monomers, photoinitiator, and UV blocker, we formulate twelve resin compositions with two AA to SA mole ratios (n:m = 100:1 or 200:1) with two different trivalent metal ion species (Al^{3+} or Fe^{3+}) in three different glycerol contents (5, 10, or 20 v/v%). The intent is to probe two relative crosslinking densities with the n:m = 100:1 set having a higher relatively crosslinking density while the n:m = 200:1 set having a lower relatively crosslinking density, denoted as high and low, respectively, in the following context. The reason for adding SA to AA is to increase the degree of ionization for metal ion binding without having to do titration; the highly concentrated photoresin is unsuitable for any pH measuring instruments. The specimen for an aluminum ion containing MPEC (noted as MPEC-Al) with

AA:SA = 200:1 and 20% volumetric glycerol content in the photoresin would be labeled as low-Al-20%. Upon 3D photopolymerization via LCD-mSLA, the MPEC synthesized *in situ* is composed of poly(acrylic acid-co-sodium acrylate) (P(AA-co-SA)) as the polyanions that are electrostatically crosslinked by the metal cations. The developed photoresins have been demonstrated to be capable of fabricated 3D architectures with various geometries, such as cubic lattice, octet lattice, and ASTM standard Type V dogbone sample, shown in Figure 2.3b.

2.2.2 Sample Preparation of Mechanical Testing

To remove the unreacted acrylic acid within 3DP MPEC samples, a post processing procedure was performed on the as-printed MPEC samples by being exposed under a 405um UV lamp (60W, Peopoly Inc.) at 5 cm distance for 30 minutes on each side. Since the MPEC samples are fabricated using aqueous photoresin, to ensure stability in ambient conditions the samples were dried at room temperature in a vacuum oven for 2 days and then equilibrated in open air for 6-25 days until the fluctuation of the sample mass within three consecutive days is less than 1%. The percentage of mass loss is calculated as

$$Mass\ Loss = \frac{Mass_i - Mass_{equ}}{Mass_i} \tag{2.1}$$

where $Mass_i$ is the initial mass of MPEC type V tensile samples after post-printing treatment and $Mass_{equ}$ is the ambient-equilibrated mass of the samples. All mass loss data of the MPEC samples used for tensile testing reported in Section 2.5 that have been measured and calculated using Equation 2.1 are presented in Table 2.1.

2.2.3 FTIR Characterization

Figure 2.3c shows the FTIR spectrum of the LCD-SLA-fabricated MPEC materials in comparison to the spectra of the PAA and glycerol. The peaks at 1600–1700 cm^{-1} and 1400–1500 cm^{-1} correspond to the asymmetric and symmetric stretches of the carbonyl functional groups, respectively. The supramolecular coordination of metal ions to P(AA-co-SA) has been confirmed by the emergence of a new peak with low intensity at 1642 cm^{-1} in MPEC-Al and MPEC-Fe spectra, which indicates the characteristic peak of stretching asymmetric vibration of the ionized carboxyl group.[36, 37] The FTIR spectrum of pure glycerol shows the five typical absorption bands from 800–1150 cm^{-1}, where the bands at 1110 and 1029 cm^{-1} correspond to the C-O stretch and the bands at 992, 922, and 851 cm^{-1} relate

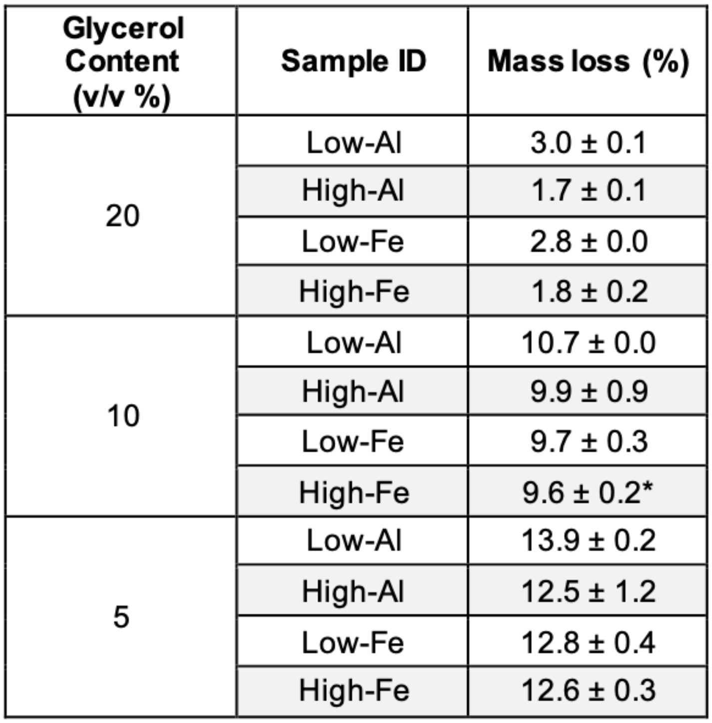

Glycerol Content (v/v %)	Sample ID	Mass loss (%)
20	Low-Al	3.0 ± 0.1
	High-Al	1.7 ± 0.1
	Low-Fe	2.8 ± 0.0
	High-Fe	1.8 ± 0.2
10	Low-Al	10.7 ± 0.0
	High-Al	9.9 ± 0.9
	Low-Fe	9.7 ± 0.3
	High-Fe	9.6 ± 0.2*
5	Low-Al	13.9 ± 0.2
	High-Al	12.5 ± 1.2
	Low-Fe	12.8 ± 0.4
	High-Fe	12.6 ± 0.3

Table 2.1: Mass Loss of MPEC Samples after Equilibrating in Ambient Condition. (The mass measurements of the set of samples marked with * are not available. The values reported here are calculated from a different batch of samples fabricated exactly the same way.)

to the vibration of the C-C backbone.[38] The same signatures of glycerol are also present in the glycerol containing MPEC-Al and MPEC-Fe samples.

2.2.4 UV-vis Characterization

The UV-vis absorption of the MPEC system has also been measured to complement the FTIR spectra. To ensure accurate comparisons between the absorbance of the ferric nitrate solution with the MPEC precursor solution containing ferric ions, the ferric ion concentration in the two solutions are the same. Hence, the new bands at 405nm and 465nm in the MPEC precursor solution containing ferric ions are solely from the complex formation of ferric ion with acrylic acid, not from the difference in the ferric ion concentration. Furthermore, the photoinitiator is not added to the MPEC precursor solution containing ferric ions for the UV-vis measurement, since TPO-L also has absorption near 405nm. Therefore, in the MPEC precursor solution containing ferric ions, the presence of a new absorbance band is indicative of complex formation that has occurred prior to photopolymerization (Figure 2.4). A similar absorbance band for aluminum complex in the MPEC precursor solution

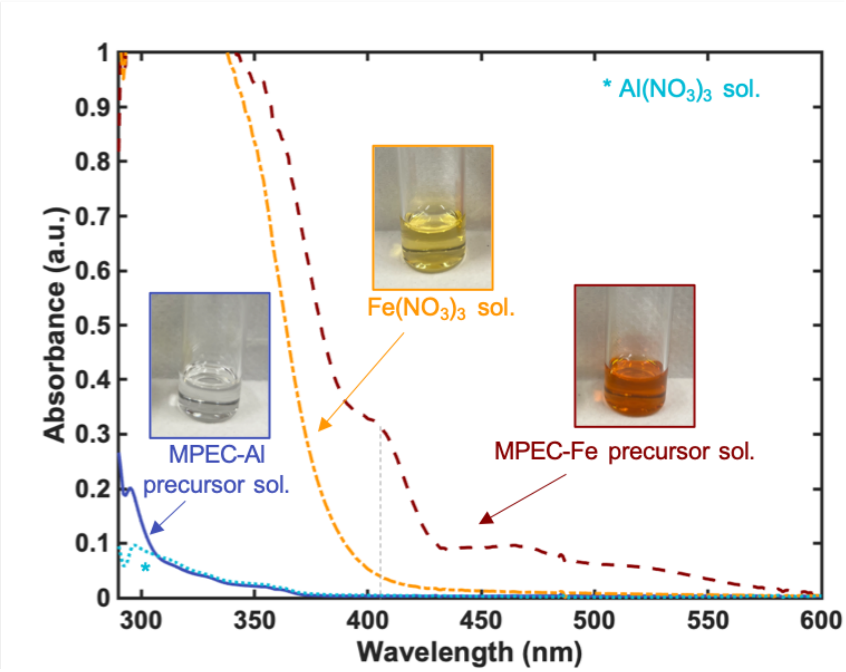

Figure 2.4: UV-vis spectra of MPEC precursor solutions with iron (III) ions and aluminum (III) ions, iron (III) nitrate, and aluminum (III) nitrate aqueous solutions. The MPEC precursor solutions are diluted 25-fold. The iron (III) nitrate and aluminum (III) nitrate aqueous solutions have the same metal ion concentration as the diluted MPEC precursor solutions. The vertical dotted line is at 405nm which is the wavelength of the light source in the 3D printer.

containing aluminum (III) ions appears at 300nm (Figure 2.4).

The UV-vis spectra of MPEC thin films have also been collected after curing MPEC precursor solutions between two glass slides with a 405nm UV lamp (Peopoly Inc). The same absorbance band at 405nm for the ferric ion complex is also present in the MPEC-Fe polymer thin films, showing that the complex can be sustained through the photopolymerization process. The MPEC-Al and polyanion control thin film samples show similar absorption profiles and minimum absorption near 405nm; the absorbance of the photoinitiator TPO-L likely provides the band at ~380nm (Figure 2.5). These absorbance bands suggest that the metal (III) ions can effectively serve as the crosslinkers in the polymer network.

2.2.5 Thermogravimetric Analysis

Thermogravimetric Analysis (TGA) is a thermal analysis method to precisely measure the mass of a sample over time by heating it to a high temperature, while gas (e.g. nitrogen or air) is flowing in the chamber. The goals for TGA measurement

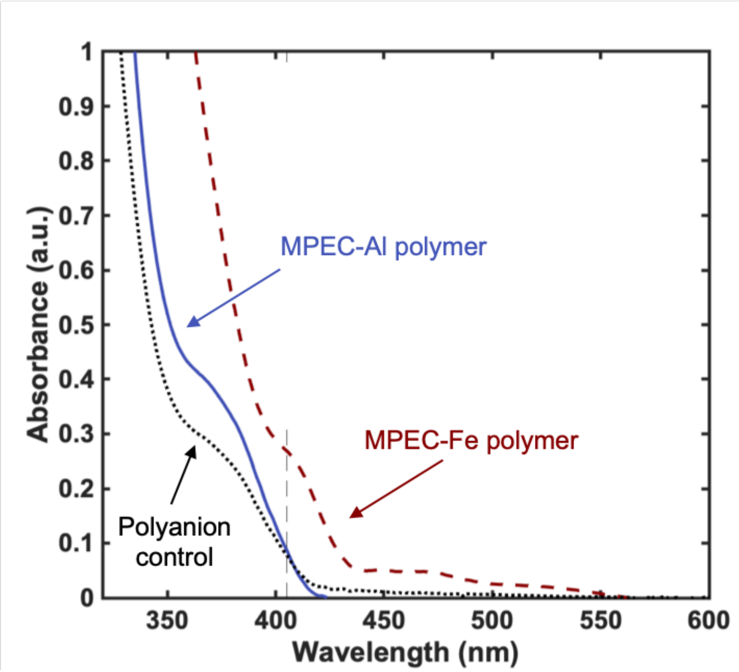

Figure 2.5: UV-vis absorption spectra of MPEC thin films compared to metal ion free control polymer. The vertical dotted line is at 405nm which is the wavelength of the light source in the 3D printer.

of ambient-equilibrated 3DP MPEC are to assess the sample stability at low temperature regime (room temperature to 100^{o}C) and to compare decomposition profiles between different resin compositions. TGA profiles of ambient equlibrated MPEC samples are conducted in air with a flow rate of 50 mL/cm^3 and a heating rate of 5^{o}C/min, shown in Figure 2.6. The mass loss from room temperature (20–25^{o}C) to 50^{o}C is less than 0.5% for all compositions and the mass loss from room temperature to 100^{o}C is less than 3% for all compositions. As introduced in the Introduction, MPEC materials do not hold water very well and show a dramatic stiffening effect upon loosing water. Because of this, MPEC must be stored in water to retain the functionalities, which limits its applications. Our 3DP MPEC shows good material stability in ambient room condition without being in water.

All TGA curves of MPEC with the same glycerol content have similar appearances and decomposition patterns (Figure 2.6). Two representative sets of derivatogram of the TGA curves (Figure 2.7) show three to four major decomposition signatures during the decomposition process. First to note, the absence of the peaks below 150^{o}C indicates no significant water loss of the samples. The first decomposition peak has an onset of 190-207^{o}C for both 5% glycerol samples of low and high

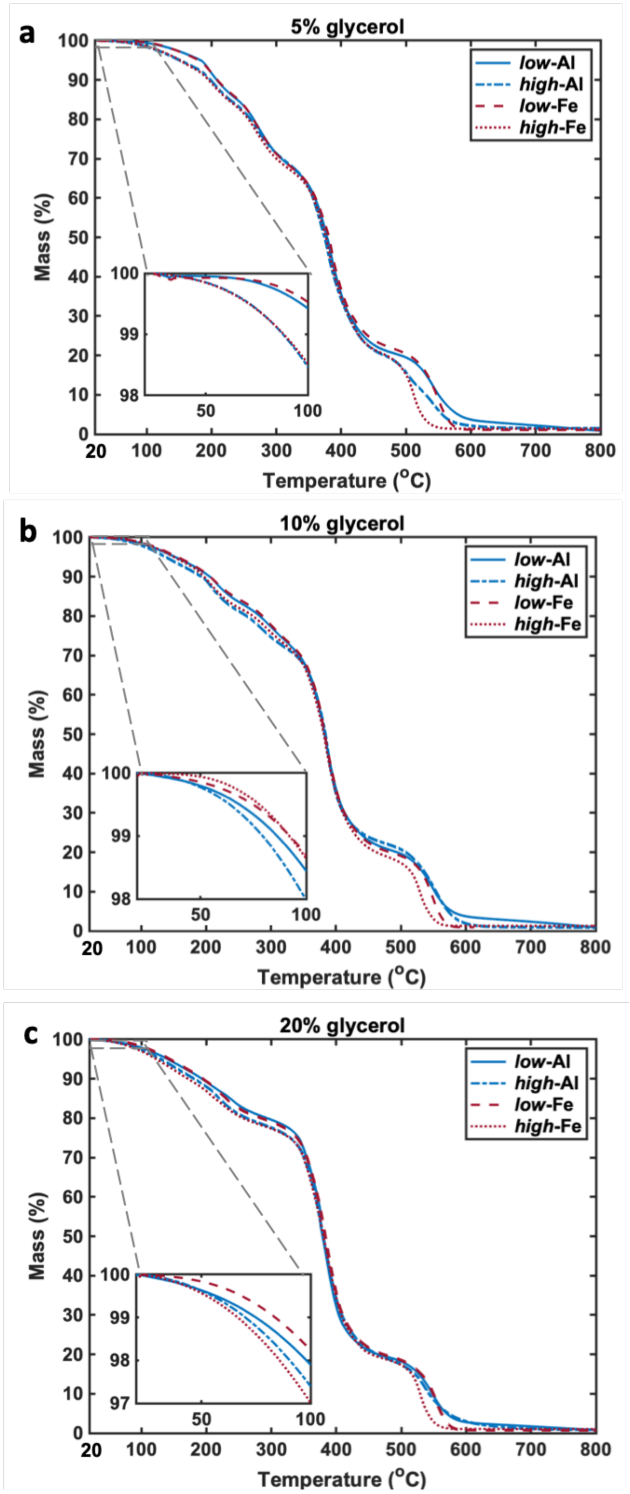

Figure 2.6: Thermogravimetric analysis of 3DP MPECs with a) 5, b) 10, and c) 20 v/v% glycerol in photoresin. Within each glycerol content, samples with two different metal ion species and metal ion concentrations have been analyzed.

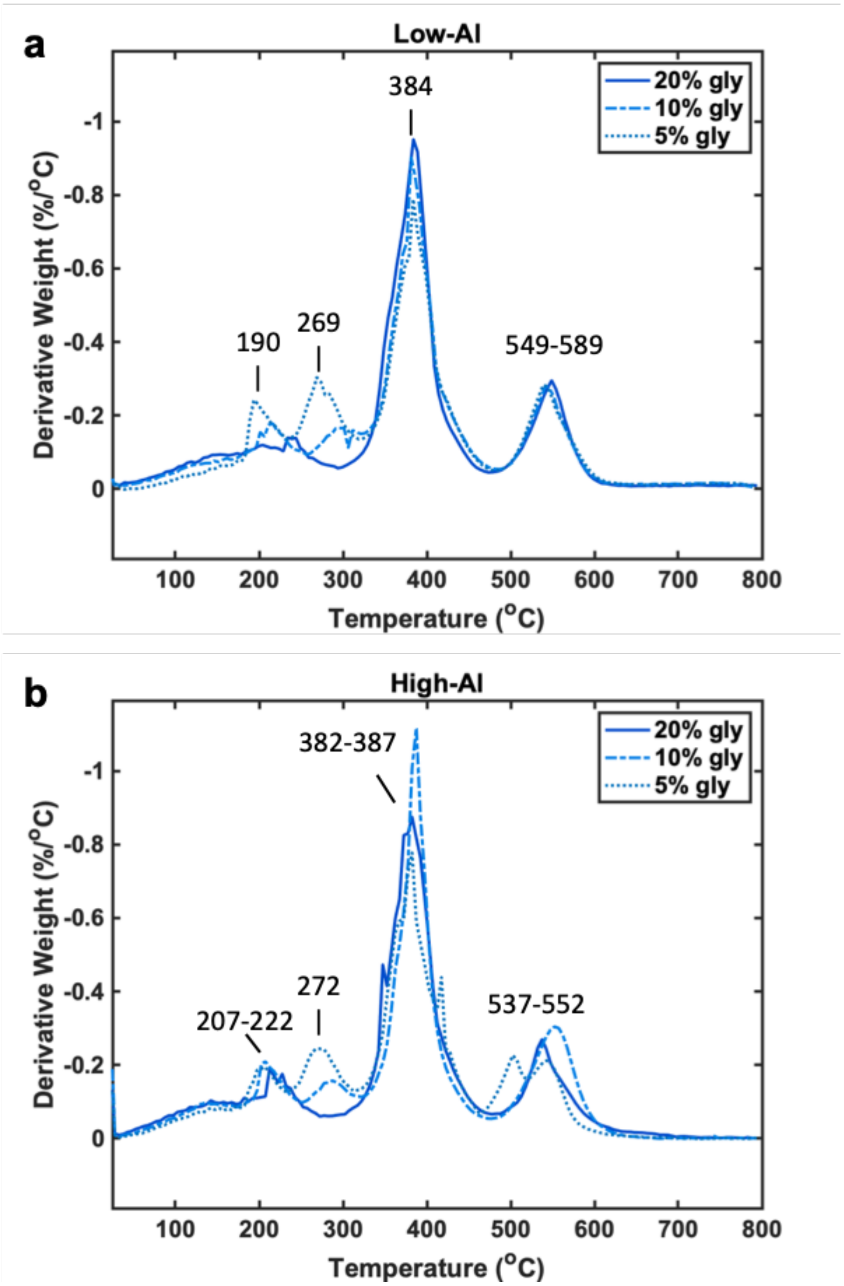

Figure 2.7: Derivatogram of TGA curves for 3DP MPECs with a) low ion content MPEC-Al and b) high ion content MPEC-Al.

relative metal contents; it is likely resulted from the loss of solvents (such as, water and glycerol) and the bound water to the polyelectrolyte.[39, 40] Next, we see some interesting deviations between the MPECs with different contents of glycerol; the 5% glycerol MPECs show a clear peak at 272^{o}C and 10% glycerol MPECs have a less pronounced peak at a slightly elevated temperature. These peaks have been reported as the decomposition of the polymer side groups [41], which suggest that the interactions between glycerol and polymer side groups can prevent the decomposition of polymer side groups. For 20% glycerol samples, the side group decomposition peak is absent below 380^oC, which is likely shifted to an even higher temperature and is overlapped with the large decomposition peak for polymer backbone at 384^oC. The final decomposition occurs between 537^oC and 589^oC that is likely attributed to combustion reactions.

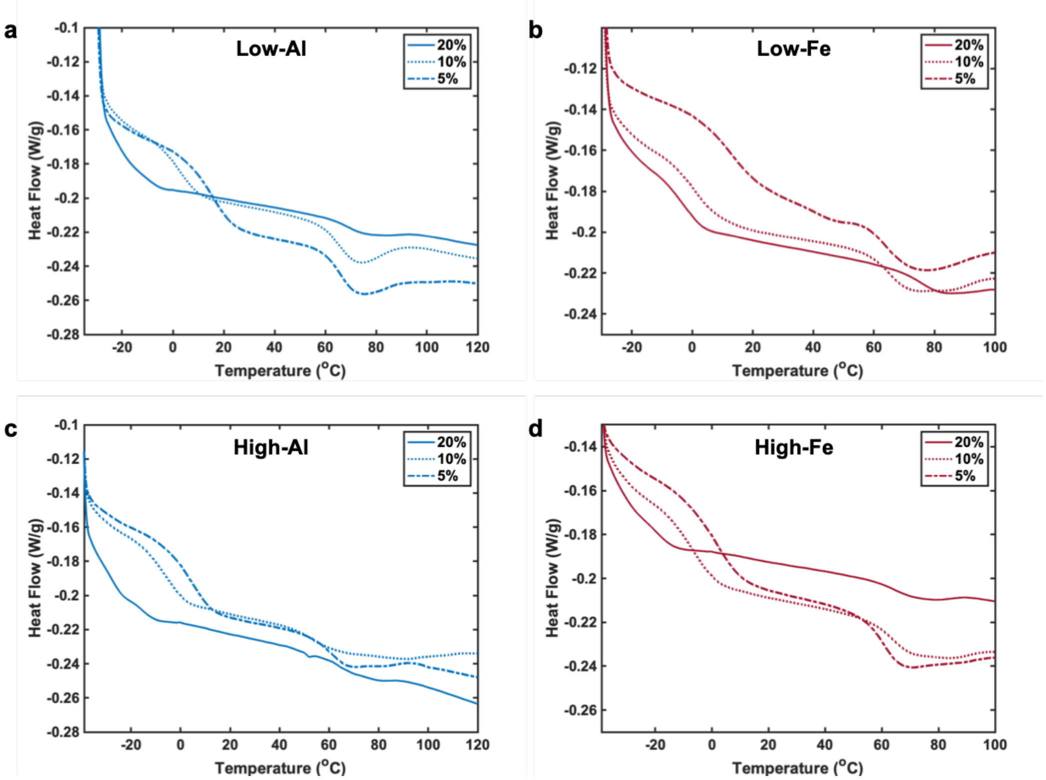

Figure 2.8: Differential scanning calorimetry measurements of 3DP MPECs with low content of a) Al and b) Fe and high content of c) Al and d) Fe from -35^oC to 120^oC. Legend provides information of the glycerol content in the MPECs.

2.2.6 Differential Scanning Calorimetry

Differential scanning calorimetry (DSC) is a thermoanalytical technique in which the difference in the amount of heat required to increase the temperature of a sample and the reference is measured as a function of temperature. DSC is commonly used for detecting and evaluating phase transformations (melting, evaporation, glass transition, etc.) that often require or give out heat. Figure 2.8 shows the DSC data for all the compositions of MPECs discussed in this chapter. There are two peaks for each curve that are present for all the compositions; first, the change in slope varying from -20^oC to 15^oC arises from the glass transition, and second, the peaks at the onset of 70^oC correspond to the endothermic process of water evaporation. These data reveal important features of these MPEC materials. The glass transition temperatures consistently shift to a low temperature with an increased content of glycerol, which is a known effect of the glycerol as additive or solvent to polymers. [42] Moreover, increasing glycerol content in MPEC shifts the evaporation temperature of water to a high temperature due to an increase in evaporation energy, and decreases the degree of water evaporation upon heating above 80^oC.[42] This result shows the important effect of glycerol on stabilizing the MPEC materials.

2.3 One-pot LCD-SLA Fabrication Approach

Vat polymerization (VP) process uses photopolymerization to fabricate 3D objects. With feedstock material being a solution or a liquid resin, it allows *in situ* polymer synthesis of functional materials and provides a vast parameter space to design the material properties of the printed objects, such as crosslinking density, hydrophilicity/hydrophobicity, and functionality of polymer side groups. In this simple one-pot fabrication of MPEC, we aim to tune the range of failure strain and UTS by varying the metal ion types and the relative crosslinking density via dynamic metal-polymer coordination bonds by changing the amount of the composition in the photoresin. The goal of incorporating SA as the comonomer is to increase the degree of ionization of the monomers in water. The formation of the supramolecular network within the MPEC samples is confirmed by the metal-coordination bonds between ferric ions and carboxylic groups of the copolymers using Attenuated Total Reflectance (ATR)-FTIR and UV-vis spectroscopy (Figures 2.3, 2.4, and 2.5). .

2.4 Tensile Testing of 3DP MPECs

The ASTM D638 Standard V tensile testing has been conducted using Universal Testing Machine (INSTRON 5569, 500 N load cell) with a standard laser extensometer system on several compositions of MPEC-Al and MPEC-Fe to determine the recoverability, ultimate tensile stress (UTS), σ_u, and failure strain, ϵ_f. The chemical structure of the MPEC polymer is shown in Figures 2.9 a and b, where the trivalent metal ions serve as the crosslinkers and bind to the ionized carboxylic side groups of the sodium acrylate fraction within the linear PAA polymers. The polymer network shows good recoverability upon applying uniaxial tension on the sample. Figure 2.9 d and e show the representative engineering stress-strain curves of MPEC specimens with the low relative cross-linking density and different glycerol contents

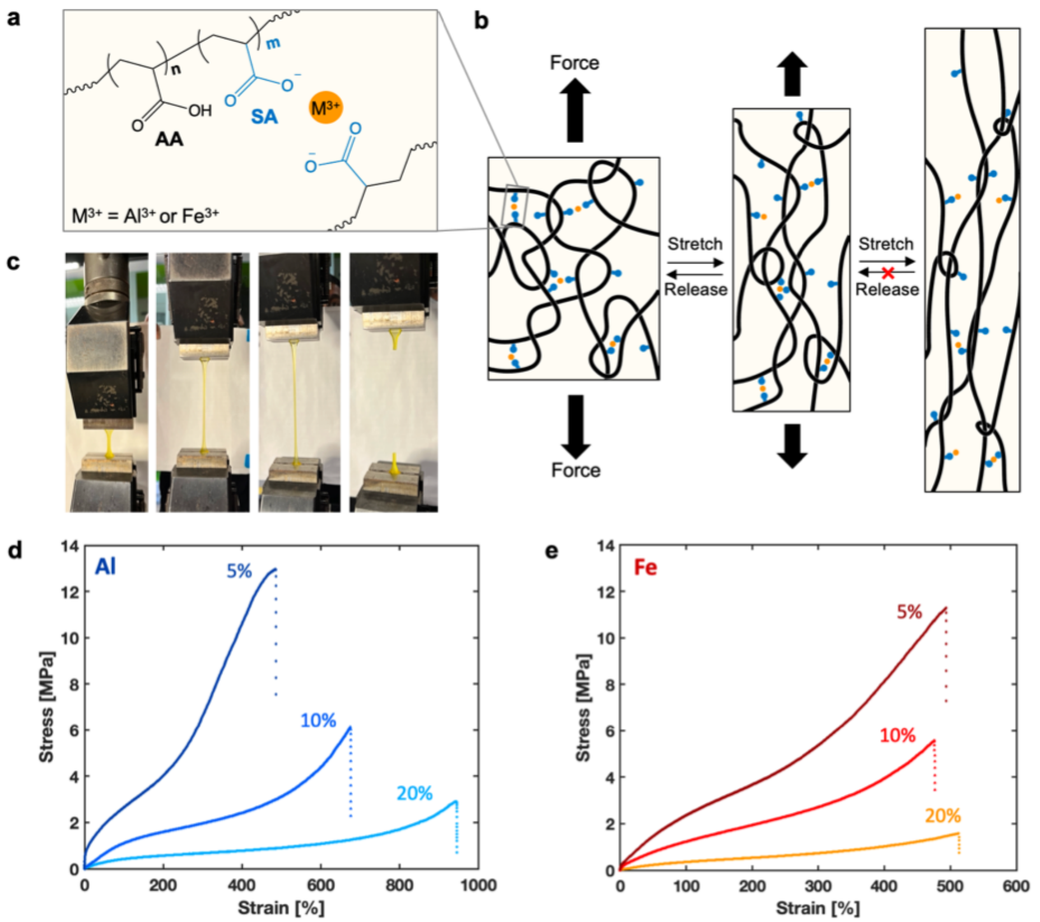

Figure 2.9: Schematics of MPEC under Tension and Stress-Strain Profiles of MPECs. a) Chemical structure of random acrylic acid (AA) and sodium acrylate (SA) copolymer. MPEC samples with two monomer mole ratios of AA to SA were fabricated: 200:1 and 100:1 (n:m = 200:1 or 100:1). Two types of metal ions are used to fabricate the MPEC samples, Al3+ and Fe3+. b) Optical images of MPEC-Al tensile sample before, under, and after stretching. c) Schematic of the supramolecular network and proposed mechanism of chain raveling and sliding under tension. Representative stress and strain curves for d) MPEC-Al and e) MPEC-Fe with 5 %, 10%, and 20% volumetric percentage (v/v) of glycerol contents in photoresins are shown.

(5, 10 and 20 v/v%), which display as typical s-shape curves of elastomeric materials. σ_u of low-Al samples decreases from 13 MPa to 3.5 MPa with increasing volumetric content of glycerol in the photoresin from 5% to 20%, whereas ϵ_f increases from 440% to 960% with the same increase in glycerol content. A similar trend on the effect of glycerol content is present in the low-Fe samples, where σ_u decreases from 12MPa to 1.7 MPa with increasing glycerol content. Unexpectedly, the failure strains of low-Fe with different glycerol contents are all around 500%. The possible causes of this unexpected observation will be explained in the later section.

2.4.1 Tensile Testing to Failure

To demonstrate the 3DP MPECs have consistent mechanical behaviors, we performed uniaxial tensile measurements to 3–4 specimens for each of the twelve different photoresin compositions in standard laboratory conditions. All the average values and standard deviations of ultimate tensile stress and failure strain are presented in Figure 2.10, plotted among the individual data points of each set. With the low relative metal ion crosslinking with a molar ratio of $AA : SA : Fe^{3+}$ of 600:3:1, the 3DP MPEC-Al (low-Al) samples exhibit a larger range of σ_u and ϵ_f than MPEC-Fe (low-Fe), shown in Figure 2.10a. The effect of glycerol-enabled high strain is clearly observed in low-Al as ϵ_f ranging from 448 ± 40%, 644 ± 28% to 942 ± 122% with increasing glycerol contents of 5, 10, and 20v/v% in the MPEC resin; the corresponding σ_u values are 12.4 ± 0.7, 6.3 ± 0.2 and 2.2 ± 0.5 MPa. With 5% glycerol content, the averaged σ_u of low-Al is 2.4MPa higher than $\sigma_u = 10.0 \pm 1.2$ MPa for low-Fe. Similarly, the averaged σ_u of low-Al with 10 and 20 v/v% glycerol contents are greater than that of the low-Fe by 1.4 MPa and 0.8 MPa, respectively.

When we increase the amount of metal ions to a molar ratio of $AA : SA : Fe^{3+}$ to be 300:3:1, the glycerol-enabled strain enhancement is not observed and the failure strains surprisingly are within a relatively narrow range. At high relative crosslinking density, the averaged ϵ_f of MPEC-Fe set (high-Fe) are 338 ± 12%, 406 ± 10%, and 362 ± 35% whereas the mean ϵ_f of MPEC-Al (high-Al) are 466 ± 20%, 481 ± 48%, and 342 ± 23% with a decreasing glycerol content of 20, 10, 5 v/v% (Figure 2.10b). Unexpectedly, an enhancement in UTS with higher metal ion content has not been observed. σ_u of high-Al spreads from 0.9 MPa to 12.5 MPa and σ_u of high-Fe are from 1.0 MPa to 7.0 MPa with decreasing glycerol content. The viscosity measurements in the section below have been conducted to address some of these discrepancies.

2.4.2 Young's Modulus

To gain better understanding of our 3DP MPEC materials, another important mechanical property needed to be evaluated is Young's modulus, also known as the modulus of elasticity or tensile modulus, which is determined by the initial slope of a stress-strain curve. The initial tensile response tends to vary from material to material. In Figure 2.15, MPEC has an initial linear region (O-A) before the curves slightly flatten out into the flow strain region (A-B). The elastic modulus can be directly related to the density of polymer crosslinks in a gel.[43] Typically polymer elastic modulus is evaluated using the slope of a stress-strain curve between 5% to 10% strain.[44] Figures 2.11a and b show the obtained elastic moduli for MPECs with low and high metal contents, which decrease with increasing glycerol concentrations. This result suggests that the glycerol content has more dominating effect on the polymer crosslinks than the metal ion concentration in the photoresin.

2.4.3 Tensile Toughness

To demonstrate the load bearing capacity of 3DP MPECs, tensile toughness, or deformation energy (U_T), which describes the energy absorbed by per unit volume of the material before rupturing (Figure 2.12), U_T is determined by integrating the area under the stress-strain curve, shown as

$$U_T = \int_0^{\epsilon^*} \sigma d\epsilon \tag{2.2}$$

where σ is the measured stress and ϵ^* is taken at the strain with the maximum stress. At low relative crosslinking density, the tensile toughness of low-Al with 5 v/v% glycerol content (low-Al-5%) is 25.1 ± 3.4 MJ$\cdot cm^{-3}$, while U_T = 15.4 ± 0.6 MJ$\cdot cm^{-3}$ for low-Al-10% and U_T = 7.8 ± 1.6 MJ$\cdot cm^{-3}$ for low-Al-20%, prospectively (Figure 3c). In comparison, the U_T values of the low-Fe set are consistently 4–5 MJ$\cdot cm^{-3}$ less than that of the low-Al set. With high relative crosslinking density, we observed lower toughness values in the set. The U_T values of high-Al with 5%, 10%, and 20% glycerol are calculated to be 23.0 ± 0.9, 7.5 ± 0.7, and 1.7 ± 0.1 MJ$\cdot cm^{-3}$, which have sustained 8.1%, 51%, and 77% decreases compared to the low-Al set. The U_T values of high-Fe also exhibit a similar trend where the obtained values are U_T = 13.1± 1.1 MJ$\cdot cm^{-3}$ for 5 v/v%, 6.7 ± 0.2 MJ$\cdot cm^{-3}$ for 10 v/v%, and 2.2 ± 0.2 MJ$\cdot cm^{-3}$ for 20 v/v% glycerol, which are 33–38% less than the toughness of the low-Fe set.

2.4.4 Cyclic Loading Test

Cyclic loading test has been conducted at a low strain range (<300%) to demonstrate the recoverability of the 3DP MPEC. As shown in Figure 2.13, with no resting time between consecutive cycles, the loading curve does not overlay with the loading curve from the previous cycle as cycling to a higher strain, which suggests bond breakage within the polymer network.[45, 46] Due to the dynamic nature of the metal–polymer coordination bond, we observed that with a 25-minute relaxation time between each consecutive cycle, the loading curves can superimpose nicely with the previous loading curve. As expected, the hysteresis indicates the viscoelastic essence of these 3DP MPEC materials, which is also indicative of energy dissipation as cycling to a higher strain.

2.5 Rheological Analysis of Dissolved 3DP MPECs

Besides high mechanical compliance and toughness, the 3DP MPECs also demonstrate excellent degradability due to the supramolecular nature, where the metal-polymer coordination can be removed in acidic or basic conditions (Figure 2.14a). Our 3DP MPECs show great degradability in basic solution at room temperature to form a homogeneous solution with linear PAA chains.

2.5.1 Rheology Measurement

The dynamic viscosity of dissolved MPECs were measured using a rheometer (ARES, TA instrument) to investigate the relative molecular weights (MWs) of linear PAA polymer within MPEC. Since the sample compositions within the set with the same glycerol content are fairly similar, as evidenced by the thermal gravimetric analysis data (Figure S4), this allows an equitable comparison of the MWs of PAA with a fixed solution concentration. As shown by thermal gravimetric analysis measurements in Figure S4, the composition of each set of MPECs with the same glycerol content are fairly similar as evidenced with the similarity in the mass loss profiles as a function to temperature. If the ratio of the MPEC mass to the volume of 1M NaOH solution is controlled (to be 50mg/1.2mL), we are able to make comparisons on the relative MWs within each set of MPECs with the same glycerol content. Figures 2.14c-e show the viscosity of the dissolved MPEC solutions decreases with increasing the shearing flow rate; this flow behavior is known as shear-thinning, which is associated with non-Newtonian viscous liquids for a solution with a linear chain structure.[47] At low shear rate, the shear flow is impeded by physical entanglement, where the viscosity value of the system remains constant and is characterized as the initial viscosity or zero shear viscosity, η_o, which is listed for various sample compositions in Table S2. For all glycerol contents, the η_o values of both low-ion sets are higher than the η_o values of both high-ion sets. Similar trend is present when comparing the Al sets and Fe sets where the η_o values of the Al sets are greater than those of the Fe sets.

2.5.2 Relative Molecular Weights of Polyanions in 3D printed MPEC to Mechanical Properties

The polyanion PAA with our MPEC system contains the ionizable carboxylate side groups which are able to dissociate from the metal ions in a polar solvent. The 3DP MPEC contains multiple components which requires extensive efforts to purify the polyanion for molecular weight measurement. It is commonly known that viscosity of polymer solutions is closely related to the polymer MW as longer chains are likely to resist flow due to entanglement. Taking advantage of this unique feature of MPEC, we performed rheological measurements of the dissolved 3DP MPEC to compare the relative MWs of PAA. The initial viscosity, η_o, values exhibit trends across all three glycerol contents in the subsequent descending order: low-Al > high-Al > low-Fe > high-Fe. Based on the Mark-Houwink (MH) relation, the dynamic or kinematic viscosity of the solution (η) and the molecular weight of the polymer chain (M) relate as the following

$$\eta \backsim KM^{\alpha} \tag{2.3}$$

where K and α are constants for a specific polymer-solvent pair. We recognize that the classic MH relation between viscosity and molecular weight is not fitted to describe MPEC solutions which contain components that affect viscosity, such as glycerol, UV blocker, and the excess base/salt, as for pure polymer solutions. The effects of the resin compositions on the MW of PAA within the 3DP MPEC is consistent for all three glycerol contents: the MW of low-ion sets are greater than that of high-ion sets regardless of the ion type; with the same metal ion concentration, the MW of MPEC-Al is higher than the MW of MPEC-Fe.

In VP, the photoinitiators break down to radicals upon UV irradiation. The radicals trigger the free radical polymerization process that includes the initiation, propagation, and termination steps to convert the monomers in solution to 3DP materials. We surmise that the MW variation associated with the metal ion types is due to the light absorption of the ferric complex near 405nm in solution that can affect free radical generation in the initiation step (Figure 2.4). Higher ion concentration would lead to high ionic strength, which is shown to increase primary cyclization rates and promote early terminations in free radical polymerization process.[48] This justifies the MW differences for the low-ion and high-ion sets.

The MWs of PAA provide more insights on the mechanical performance of 3DP MPEC. Upon applying tension, the ability of MPEC containing higher MW PAA chains to unravel would allow the samples to reach a higher failure strain. Loosely crosslinked polymer networks would have higher numbers of repeat units between crosslinks, thus the glycerol-enabled high strain behavior would be more pronounced. This can be validated by the uniaxial tensile results of low ion content sets; given the same metal ion and 10%–20% glycerol content, the MPEC-Al samples consistently reach 180%–320% higher failure strains than MPEC-Fe (Figure 2.10a). Such behavior is absent in the samples with lower glycerol content (5 v/v%) likely due to the smaller free volume and higher friction between polymer chains. The high ion content sets do not display a clear evidence of strain enhancement by glycerol, suggesting that the crosslinking density as well as polyanion molecular weight are critical factors on the mechanical performance.

2.6 Summary of Effect of Resin Formulation on Mechanical Properties

By simply introducing stochiometric variation in photoresin formation, the resulted 3DP materials not only demonstrated high compliance, toughness, and good tunability, but also exhibit a desirable “S-curve” stress-strain behavior which is commonly seen in organic biopolymers. At temperature higher than its glass transition temperature, such a polymer system can undergo different deformation stages through molecular reconfiguration that include uncoiling and strengthening before reaching catastrophic failure. The tensile testing reveals that the 3DP MPEC mimics this behavior where it displays high compliance at a low flow stress (point A in Figure 2.15) up to a high flow strain with limited stiffening effect (A-B in Figure 2.15), followed by a high strain-stiffening region (B-C in Figure 2.15) that lead to a high ultimate tensile strength at rupture.

2.6.1 Effect of Metal Ion Type

Metal ion-polymer coordination has been demonstrated as a way to enhance the mechanical strength of polymeric systems.[31] The binding affinity of the metal ions and polymer is specific to the chemical environment of the metal ion-polymer pair.[24] Higher binding affinity leads to stronger metal ion-to-polymer coordination bonds that contribute to the material strength.[32] The effect of metal ion type on mechanical properties manifests in UTS, failure strain, and tensile toughness of MPEC. Despite the glycerol content, the viscosity measurements reveal that the MWs of PAA within MPEC-Al are higher than those of the MPEC-Fe set due to the iron (III) absorption at the 3D printer light source wavelength, 405nm (Figure 2.4). Comparing to the low-MPEC-Fe set, the longer polymer chains within the low-MPEC-Al sample set give rise to larger flow strain region (A-B in Figure 2.15), which is likely attributed to its superior failure strain. The strain-stiffening portion (B-C in Figure 2.15) of the stress-strain tensile profile for the low-MPEC-Al set is also more pronounced before reaching a high ultimate tensile strength further suggesting the enhanced polymer entanglement. With enhancement in both failure strain and UTS, the resulted tensile toughness of the low-MPEC-Al set is also consistently greater than that of the low-MPEC-Fe set. The high-MPEC samples do not exhibit a clear trend in terms of failure strain and UTS, but the UT values of high-MPEC-Al are generally greater than those of the high-MPEC-Fe.

2.6.2 Effect of Metal Ion Content

Higher ion concentration leads to higher ionic strength in solutions. Higher ionic strength gives rise to an increase in the degree of primary cyclization and promotes early termination in free radical polymerization process, thus results in shorter polymer chains.[48] Regardless the glycerol content, the viscosity measurements reveal that linear PAA chains of MPECs made with photoresins containing low-ion concentrations are longer, which can be seen by comparing between the solid data point versus the hollow ones in Figure 2.14. Because of this, the low-MPECs continuously reaches to higher failure strain with increasing glycerol content, where the absence of glycerol-enabled strain enhancement for high-MPEC is likely due to the low degree of physical entanglement with shorter polymer chains. This leads to the tensile toughness of the low-MPEC set exceeding the high-MPEC set (Figure 2.12a and b). While the averaged U_T of low-Al-5% is only 0.5 MJ·cm^{-3} likely due to high friction between chains, the averaged U_T of low-Al-10% and low-Al-20% are approximately 77-78% higher than the U_T of the corresponding high-Al sets. For MPEC-Fe, the U_T of low-MPEC-Fe surpasses the U_T of high-MPEC-Fe by 33-38%.

2.6.3 Effect of Glycerol Content

Glycerol being a low vapor pressure solvent can prevent further water loss of sample in ambient conditions, as well as serve as a plasticizer that can increase the free volume between polymer chains and enable higher strain by reducing friction.[8] As shown in Figure 2.10a, the failure strain of both MPEC-Al and MPEC-Fe has been enhanced with higher glycerol contents. In the low metal ion content samples, the increase in failure strain for MPEC-Al is more significant than that for MPEC-Al, which is likely enabled by the higher MW PAA chains in the MPEC-Al samples. Although the glycerol-enabled high strain comes at the cost of the material's tensile strength, a commonly seen phenomenon in loosely crosslinked polymers with such additive [49], it alleviates the reduction in toughness with increasing glycerol content. This effect is the most pronounced in the low-MPEC-Al set; from 5% glycerol content to 20%, the averaged UTS decreases by 82%, whereas the averaged U_T only decreases by 70%.

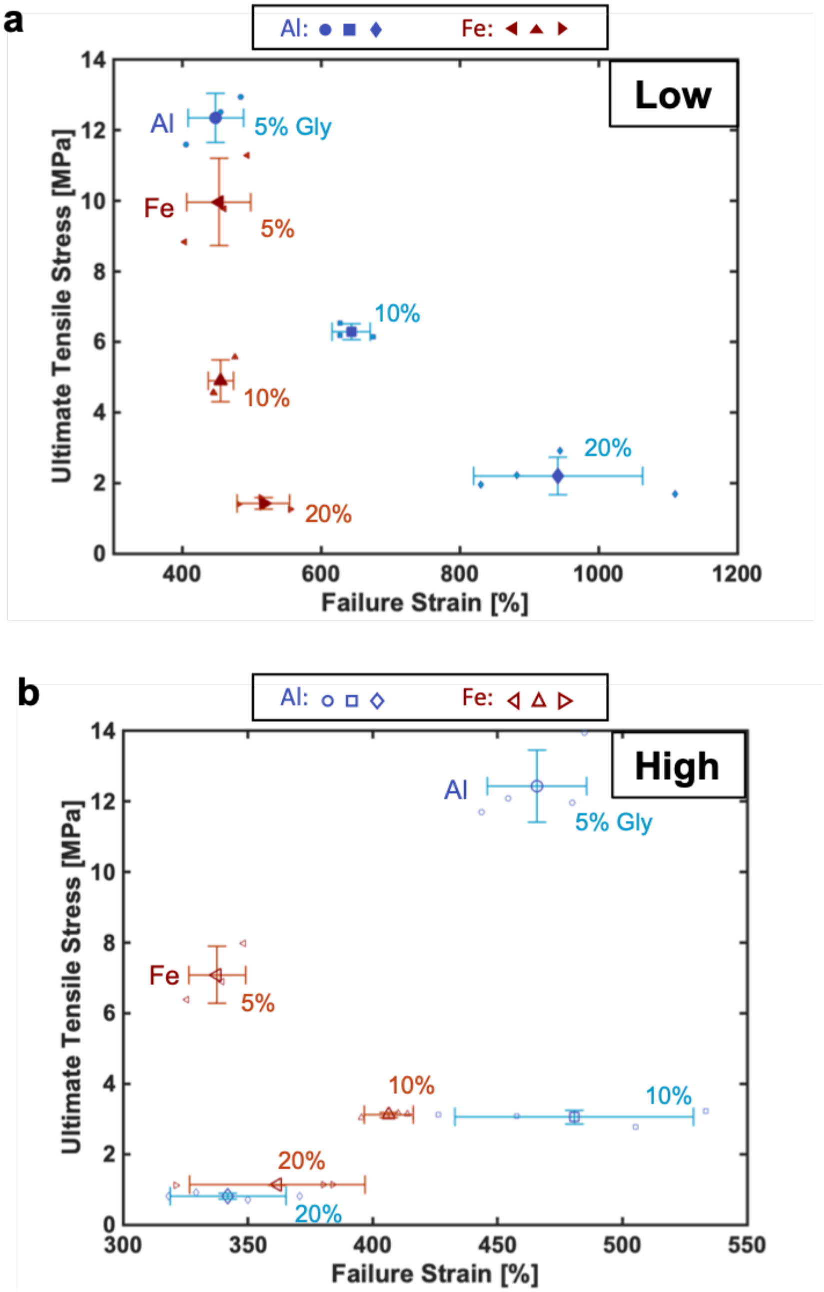

Figure 2.10: Ultimate tensile strength and failure strain of a) low (n:m = 200:1) and b) high (n:m = 100:1) relative crosslinking density of MPEC-Al and MPEC-Fe tensile specimens with 5%, 10%, and 20% v/v glycerol contents in the photoresins. Data points and error bars correspond the mean and standard deviations of each set of 3–4 specimens. All individual data points in each set are also shown using small markers.

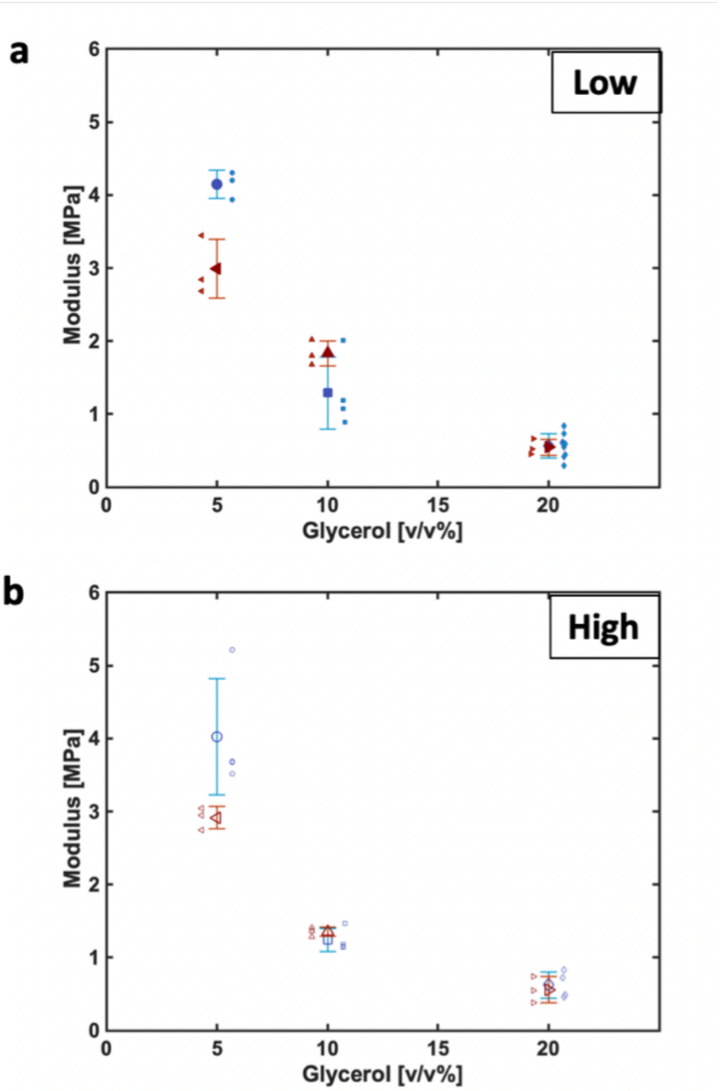

Figure 2.11: Elastic Modulus of 3DP MPECs determined at 5%–10% strain for a) low and b) high metal ion concentrations. All individual calculated modulus values and the standard deviations of each set are also shown using small markers.

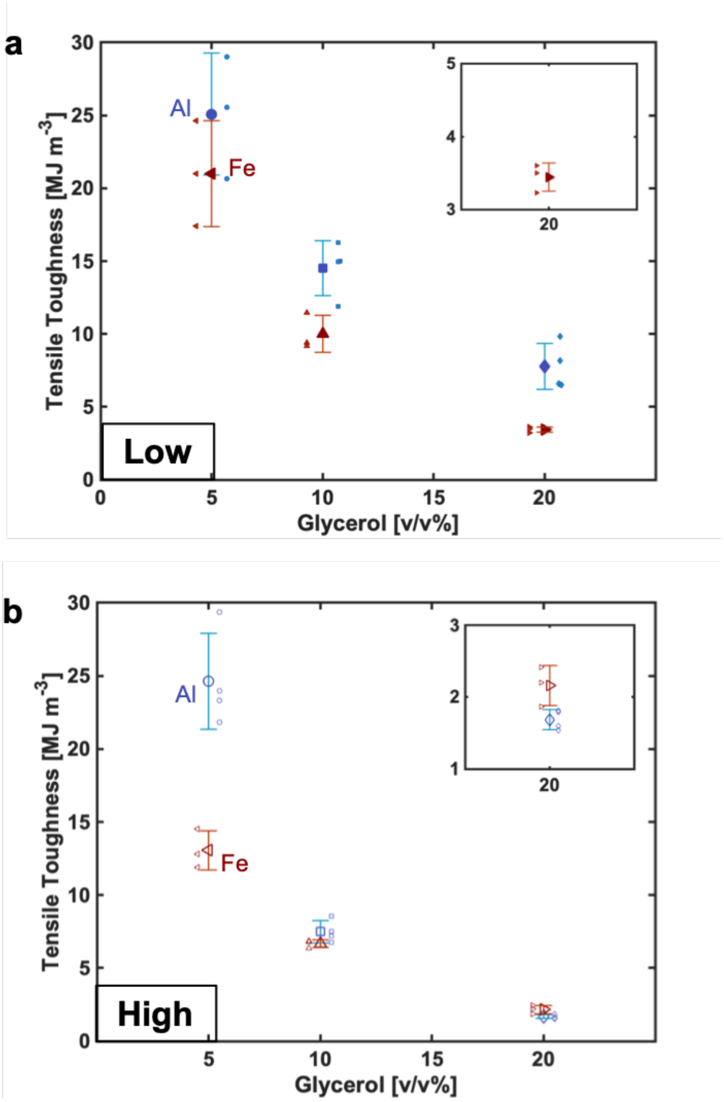

Figure 2.12: Tensile toughness with respect to volumetric content of glycerol in photoresin for a) low (n:m = 200:1) and b) high (n:m = 100:1) relative crosslinking densities in MPEC-Al and MPEC-Fe. Data points and error bars corresponded the mean and standard deviations of each set of 3–4 specimens. All individual data points and the standard deviations in each set are also shown using small markers.

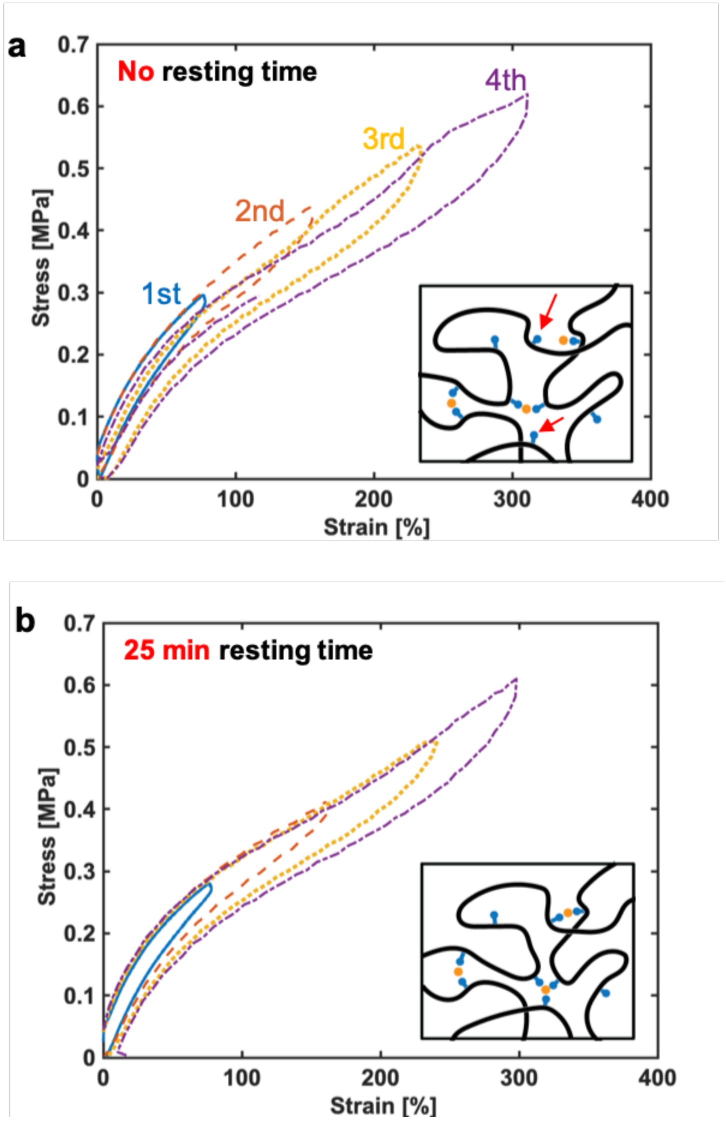

Figure 2.13: Cyclic loading tests to 300% elongation of a low ion content specimen a) without and b) with 25-minute resting time between consecutive cycles. The inserts are schematic of the molecular networks and the red arrows indicate the local bond breakage under tension.

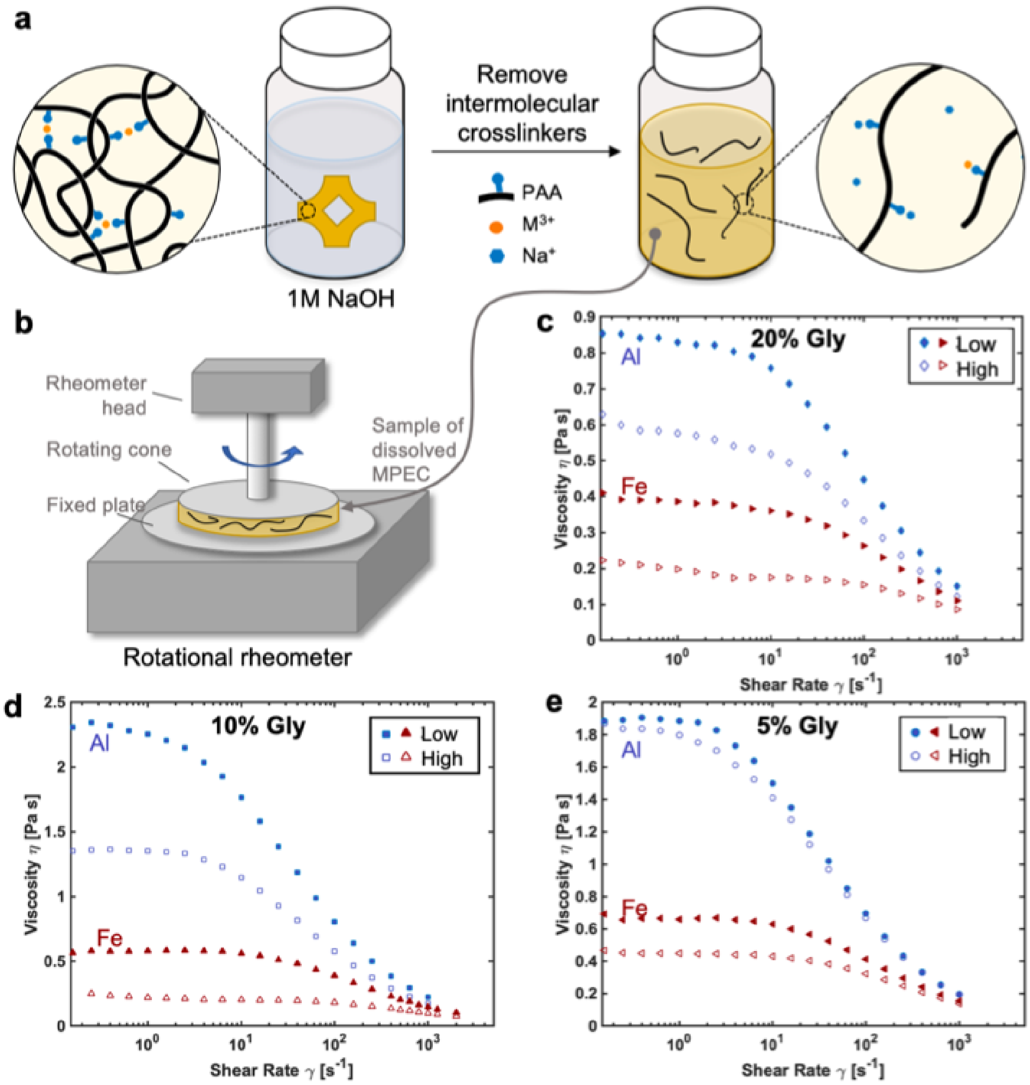

Figure 2.14: Schematics of a) the sample preparation for the rheological samples and b) the rotational rheometer used for the viscosity measurements. Rheological measurements of dynamic viscosity as a function of shear rate for MPEC-Al and MPEC-Fe samples with c) 20%, d) 10%, and e) 5% glycerol contents dissolved in 1M NaOH at room temperature.

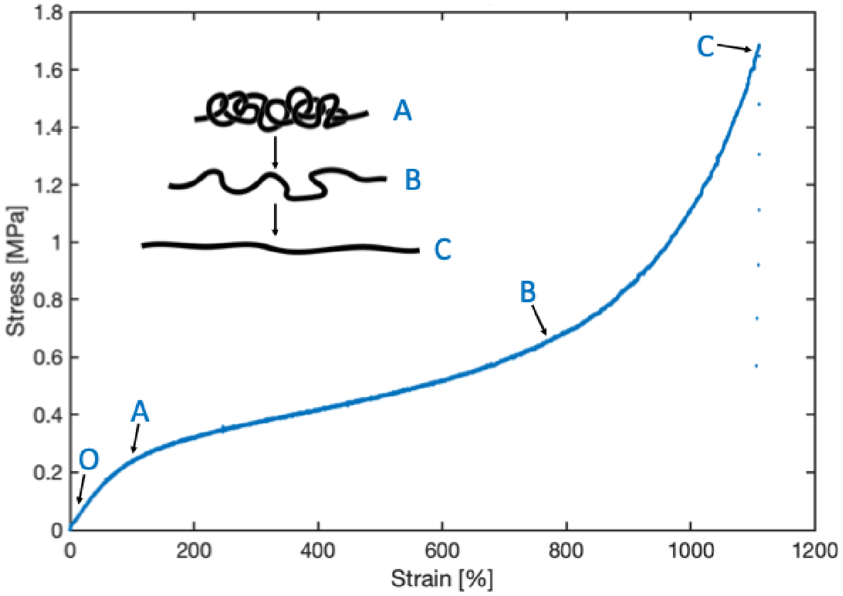

Figure 2.15: S-shape tensile curve and schematics of polymer configuration upon tension. The stress-strain curved is from a MPEC-Al-20% sample.

Chapter 3

ADDITIVE MANUFACTURING OF THERMAL RESPONSIVE DOUBLE NETWORK HYDROGELS

Chapter Abstract

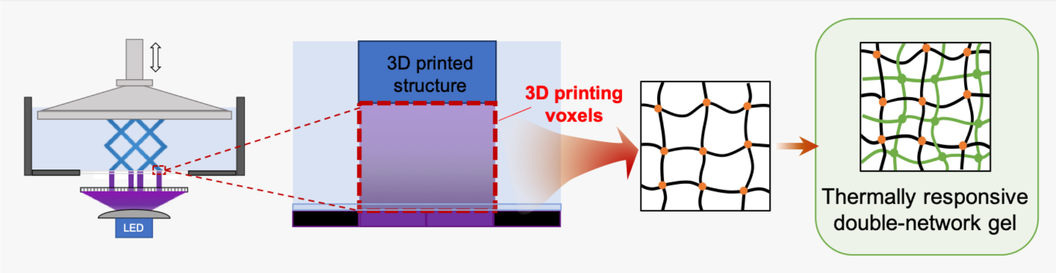

Figure 3.1: Schematic Overview of Chapter 3.

Thermoresponsive polymers such as poly(N-isopropylacrylamide) (PNIPAM) are important smart materials due to their biocompatibility and near-biological lower critical solution temperature (LCST) at 32°C. This critical property enables many potential applications in drug delivery and capture, tissue engineering, soft robotics actuation, and efficient water release following purification or atmospheric water harvesting.[50–52] To compensate for the mechanical fragility of these gels, this work explores sequential interpenetrating networks (IPNs) fabricated using an architected first network 3D printed by micro-stereolithographic techniques from polyacrylic acid (PAA), polyacrylamide (PAM), and poly(acrylic acid-co-acrylamide) (P(AA-co-AM)). It is found that AA contents in the first networks of these gels caused polymer-polymer phase separation that could be compensated by copolymerization with AM. However, at low density and light crosslinking, the first network does not interfere with the polymer-water phase separation of the PNIPAM second network. Using a lightly crosslinked second network and these insights with P(AM-co-AA)/PNIPAM IPNs, stable architected IPNs consistently displayed strong phase transition behavior at an LCST between 31°C and 33°C with volumetric shrinkage due to water loss tunable between 30% and 70%.

Adapted from:

Amylynn C. Chen et al. “Additive manufacturing enabled thermally responsive double network hydrogels (*In preparation*).” 2022.

3.1 Introduction to Thermoresponsive Polymers

Thermo-responsive polymer is a class of stimuli-responsive or smart material system with temperature stimulus that triggers change in material property, such as shape-memory effect, sol-gel process and coil-globule transition.[54–56] A particular interest is on thermally responsive hydrogels. Due to the higher water content and the soft but rubbery mechanical property, hydrogels closely resemble living tissues and have been investigated intensely in the biomedical research. The ability to provide three-dimensional network made with biocompatible materials to allow cells and tissue to interact and grow onto one another is very promising for discovering new materials for therapeutic drug release, medical implants, and tissue engineering.[50, 57, 58]

Based on their response to change in temperature, these polymers can be categorized in two types; first, polymers that become insoluble and undergo phase change above a critical temperature, namely the lower critical solution temperature (LCST), and second, polymers and other components of mixtures that become miscible in all proportions above a critical temperature called the upper critical solution temperature (UCST). These phenomena are due to the miscibility gab driven primarily by enthalpy of mixing in the case of UCSTs and by a negative (unfavorable) entropy of mixing for LCSTs.[59, 60]

Often, these transitions are studied in the context of solutions of linear polymers with low polymer content on the order of 1wt% and observed empirically by their cloud-point, the temperature at which the solutions become opaque due to this phase separation.[59, 61] However, these phase transitions occur in polymer gels as well. In thermogels, a thermoresponsive gelation is driven by the formation of micelles of thermoresponsive blocks, crosslinked by non-thermoresponsive blocks in the copolymer.[62] Even in covalently crosslinked hydrogels, thermoresponse can be observed in homopolymer gels, copolymer gels, and interpenetrating networks that contain significant compositions of a thermoresponsive material.[63] The entropy-driven polymer collapse and rejection of solvent results in a deswelling and opacity in such crosslinked gels. These phenomena can be probed by differential scanning calorimetry (DSC), thermalgravimetric analysis (TGA), mass and volumetric change measurements, small-angle neutron scattering, transmittance vs temperature, and nuclear magnetic resonance (NMR) spectroscopy.[64]

3.1.1 Poly(N-isopropylacrylamide)

Many common polymers display both UCST and LCST behaviors such as poly(ethylene oxide), poly(hydroxyethyl methacrylate), polyacrylic acid under specific ionic strength and pH conditions, some zwitterionic polymers, poly(3-acrylamidopropyl trimethylammonium chloride), and even some semiconducting polymer-small molecule systems.[59, 61, 65] Among all, poly(N-isopropylacrylamide) (PNIPAM) has been one of the most widely studied and quintessential thermoresponsive polymer systems that undergoes a phase change at an LCST of 32°C. Below the LCST, hydrogen bonding is formed between the amide groups on the polymer and water molecules that keeps the polymer miscible with water. As temperatures rise above the LCST, the polymer chain undergoes conformational changes from an expanded chain to a globular structure while exposing the hydrophobic isopropyl groups, hence transitions from the hydrophilic to the more hydrophobic state. This transition, known as coil-globule transition, can be observed when the polymer solution is heated through its LCST. (Figure 3.2). Its near-biological temperature LCST makes PNIPAM a desirable material along with its other characteristics, such as biocompatibility, easy synthesis, and easy modification through copolymerization. [66, 67]

However, being mechanically weak and fragile limits the applications of PNIPAM and presents challenges to be accurately characterized using standard mechanical testing devices.[68] Various parameters can affect the mechanical properties of PNIPAM, such as initial monomer concentration, crosslinker ratio, measurement temperature, and the degree of swelling at the time of measurement. As a result, it is often made into micelles rather than solid gels and even its thin-films cannot structurally support architecture, cyclic swelling/deswelling, or the growth of more than a few cell-layers.[57, 69, 70]

Despite the mechanical weaknesses, the LCST behavior of PNIPAM can be readily controlled though copolymerization. A previous study has demonstrated by copolymerizing with a more hydrophobic monomer, such as 2-hydroxyethyl methacrylate (HEMA); by increasing the polymer’s affinity for water, the LCST shifts to a lower temperature; when NIPAM copolymerizes with more hydrophilic monomers such as N,N-dimethylacrylamide (DMAA) or acrylamide, the LCST increases as stronger hydrogen bonds can be formed between copolymer and water.[72] It has also been

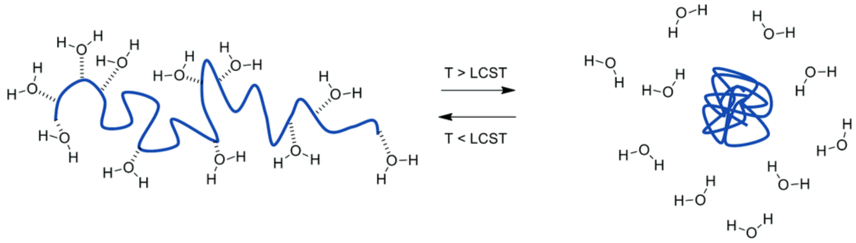

Figure 3.2: Schematic of polymer conformational transition (coil-globule) near LCST.[71]

found that lowering the water content of a copolymer of NIPAM and methacrylic acid (MAA) shifts the LCST and glass transition temperature to higher temperatures, due to the loss of chain mobility and lower free-water content preventing the LCST phase transition from occurring.[64]

3.1.2 Interpenetrating Polymer Networks

Interpenetrating polymer networks (IPNs) are a class of polymer systems that contain two or more polymer networks are often entangled or at least partially interlaced, but not covalently bonded to each other on the molecular scale. Although not all IPNs exhibit thermal responsive behaviors, there have been studies that show the compatibility of PNIPAM with many non-thermoresponsive polymers, particularly with hydrophilic polymers, such as poly(vinyl alcohol), polyacrylic acid (PAA), PAM, and PMAA, to form IPN hydrogels.[63, 73, 74] Similarly to the copolymerization approach, it has been found that formation of interpenetrating networks with PNIPAM can also affect the LCST due to the hydrophilicity or hydrophobicity of the copolymers to obtain the range of LCST, 20–50^{o}C. Analogous to the NIPAM-containing copolymers, with the incorporation of high hydrophilic polymer content, the enhanced hydrogen interaction within the network pushes the coil-globule transition to a higher temperature.

Besides improving the thermo-responsibility, the second network in PNIPAM-containing IPNs can also provide a toughening effect, add functionalities through the introduction of a dynamic network, and offer sacrificial networks.[31, 58, 75–77]. There have been works focusing on introducing linear polymers into IPNs to improve the mechanical property of PNIPAM. For example, Guo et al. found in compliant systems on the order of tens of kPa strength that interpenetrating hydrophilic poly(N,N-dimethylacrylamide) PDMA into a PNIPAM 1st network or host network results in greater toughness and lower swelling ratio compared to the semi-IPN fabricated from PNIPAM inside a PDMA host.[78] A phase-separation enhanced toughening is observed that reduces crack propagation in the PNIPAM/PDMA system. There is also a decreased swelling ratio in PDMA/PNIPAM IPN relative to PNIPAM/PDMA because linear PDMA has a greater affinity for water above LCST, but also has a greater tendency to diffuse out of the polymer since the PDMA network is not crosslinked. Related work with linear PAA chains swollen in a PNIPAM host network found to the contrary that LCST, volumetric shrinkage, injectability, and lack of phase separation did not depend on concentration or molecular weight of PAA chains.[79] In our study, we focus on the fabrication of IPNs with two crosslinked networks.

3.2 Tuning Volumetric Change of Thermoresponsive IPNs for Optimized Water Release

Atmosphere water harvesting (AWH) emerges as a promising approach to address water scarcity of arid regions, such as remote islands or desert areas. The AWH process condenses water vapor to liquid water; it requires an efficient absorbent to absorb moisture and then release it in the form of vapor or liquid. Deliquescent salts, such as calcium chloride and lithium chloride, exhibit high water uptake of 5–6 time of its own weight, but particle agglomeration and solvation of the salts can result in reduced permeability of water vapor and poor cyclability during hydration and dehydration processes.[80–82] Porous sorbents, such as metal-organic frameworks, silica gels, zeolite, and activated alumina, are great insoluble moisture sorbents due to their high affinity to water, high sorption/desorption rate, sorption at low humidity, excellent thermal stability and cycle performance; however, an alleviated temperature is often required for the removal of the absorbed water making AWH costly and energy-intensive.[83–85]

Because of the large volumetric shrinkage and the ability to reject water above LCST, the PNIPAM-containing polymers are ideal candidates to be combined with efficient moisture sorbents to achieve controlled water release. As mentioned above, the desorption process can be energy intensive due to the high affinity of water to the binding sites that often involves evaporation of the absorbed water followed by subsequent cooling steps to achieve liquid water collection via condensation. These thermoresponsive IPNs are capable of liquid-polymer phase separation at LCST, which can potentially reduce the temperature and energy required to release liquid water after collection from the atmosphere.[69]

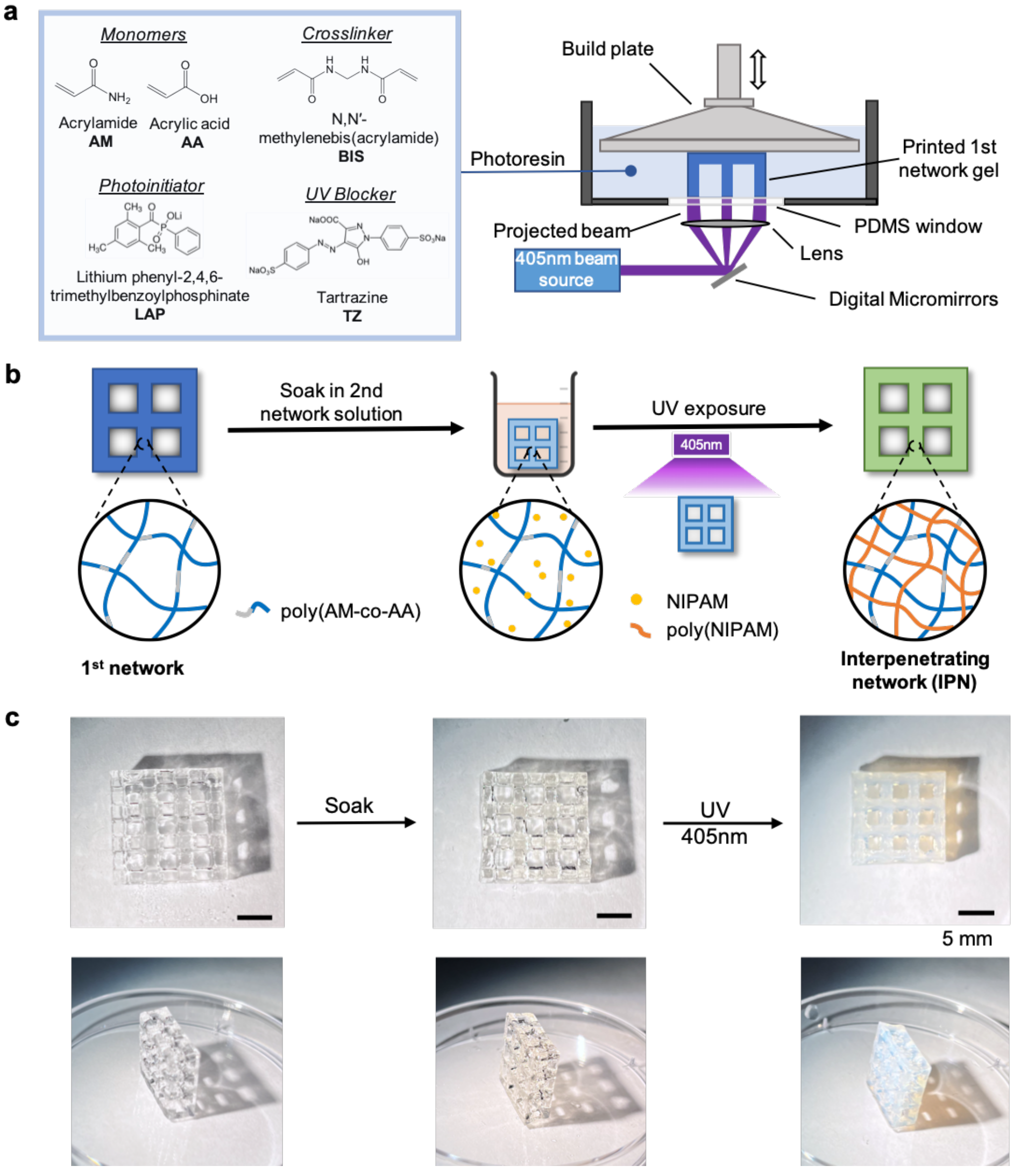

Figure 3.3: Fabrication steps of double network gels for controlled water release: a) chemical composition of photoresin and schematics of digital light processing (DLP) stereolithography (SLA) for 1st network gel fabrication, b) schematics of steps for 2nd network fabrication and c) optical images of gels for each step during 2nd network fabrication. All scale bars are 5mm.

3.3 Fabrication of Thermoresponsive Interpenetrating Networks

The thermally-responsive IPNs were fabricated by a sequential method. A first network was 3D architected using Ember (Autodesk, Inc) 3D printer, a commercially available projection micro-stereolithography (PμSL) to create the host gel or 1st network of the IPN in a layer-by-layer fashion. The composition of a photoresin for P(AA-co-AM) is shown as an example in Figure 3.3a, which includes acrylic acid (AA) and acrylamide (AM) as the comonomers and chain builders, N,N'-metheylenebis(acrylamide) (BIS) as crosslinker, lithium phenyl-2,4,6-trimethylbenzoyl phosphinate (LAP) as photoinitiator, and tartrazine (TZ) as UV blocker; all are dissolved in water to make 1, 1.5, 2.5 and 3.5 M solutions. In addition to P(AM-co-AA), the first network have also been explored in the context of PAA and PAM of different concentrations. The as-printed first network gel is then soaked in water to remove unreacted resin components.

As shown in the schematic in Figure 3.3b, upon purification the first network gel is then swelled in a second network solution and sequentially the swollen gel is cured by a UV lamp (405nm, Peoply Inc.) to obtain the completed IPN. Three separate second network solution concentrations have been explored which are 0.9, 1.4, and 1.8M. Same as the first network, the formation of second network is also achieved by photopolymerization via a free radical mechanism. Detailed resin compositions are listed in Appendix C.1. Figure 3.3c displays optical images of the sample during each step of the IPN fabrication. The opaqueness of the post UV-cured sample suggests phase separation within the polymer networks as previously introduced in Section 3.1.[61] In the following sections, the composition of 1st and 2nd networks would be optimized for improved compatibility of the networks and better control in water release.

3.4 Characterization and Optimization of Thermally Responsive IPNs

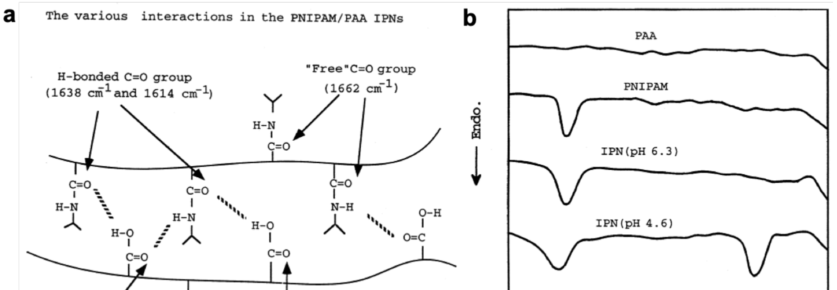

Figure 3.4: Interactions of PNIPAM and PAA within IPNs. a) Schematic diagram illustrating the interaction of the amide I group and the carboxylic acid. b) DSC thermograms of two reference polymers and (PMIPAM/PAA) IPNs. Figure reprinted with permission from the copyright holder, Elsevier.[86]

Various interactions are available in PNIPAM/PAA IPNs as shown in Figure 3.4a, where PNIPAM is forming a monomeric or dimeric form of hydrogen bonding with the carboxilic acid groups of PAA.[86] The transition heat from the hydrophobic collapse of PNIPAM is endothermic and often studied using differential scanning calorimetry (DSC) (Figure 3.4b). The following sections show the results on the chemical conformation of the IPN composition by FTIR, the optimization of polymer-liquid separation of IPNs using DSC, and volumetric shrinkage measurements of the IPNs when heated above LCST.

3.4.1 FTIR Characterization

Analysis by FTIR spectroscopy confirms the incorporation of the NIPAM into the IPN. The carboxyl C=O stretch at approximately $1700cm^{-1}$ and the broad bands between 1240–1150 cm^{-1} are all signatures of PAA and present in both the PAA control and the IPN, contributed from the first network. Two new additional bands in the IPN spectrum are assigned as the signatures of the isopropylacrylamide side of PNIPAM with the N-C=O stretch at $1622cm^{-1}$ and the C=N stretch at approximately $1550cm^{-1}$, which are indicative of PNIPAM incorporation into the second network of the IPN.[87, 88]

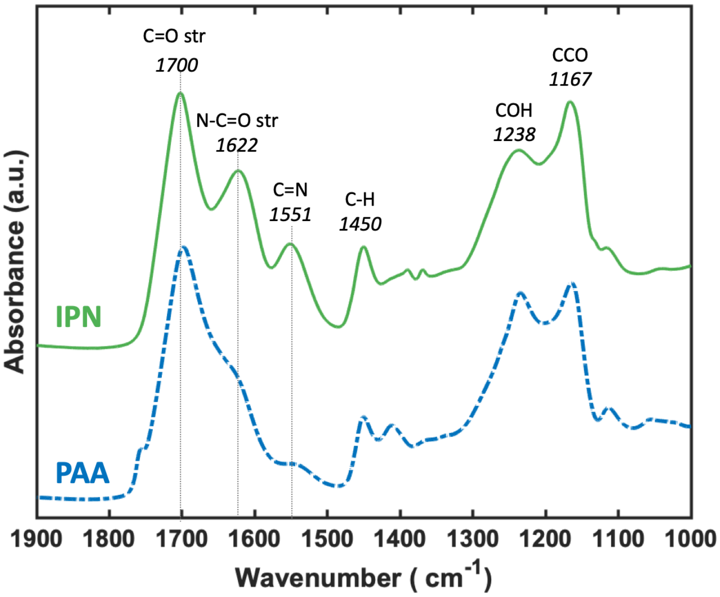

Figure 3.5: FTIR spectra of PAA and IPN with PAA as 1st network.

To assess the compatibility of the two polymer networks, differential scanning calorimetry (DSC) is used to detect the LCST of the fabricated IPNs. DSC measures difference in heat required to increase the temperature of a sample and the reference as a function of temperature. PNIPAM undergoes polymer to liquid separation at its LCST that can be observed as an endothermic peak in the DSC thermogram (Figure 3.4b). For reference, no endothermic peak was observed in the PAA reference; the endotherm appeared at 32°C in the reference PNIPAM and the IPNs are resulted from the enthalpy gain of coil-globule transition of PNIPAM by rejecting water (Figure 3.4b).[86] The coil–globule transition describes the collapse of a macromolecule from an expanded coil state to a collapsed globule state. In this work, several IPN material systems have been explored including PAA/PNIPAM, P(AM-co-AA)/PNIPAM, P(AM-co-SA)/PNIPAM and PAM/PNIPAM IPNs. Combining the DSC analysis and assessment on the opacity of the obtained IPNs, we can evaluate the compatibility of the two networks for a given composition.

3.4.2 Differential Scanning Calorimetry

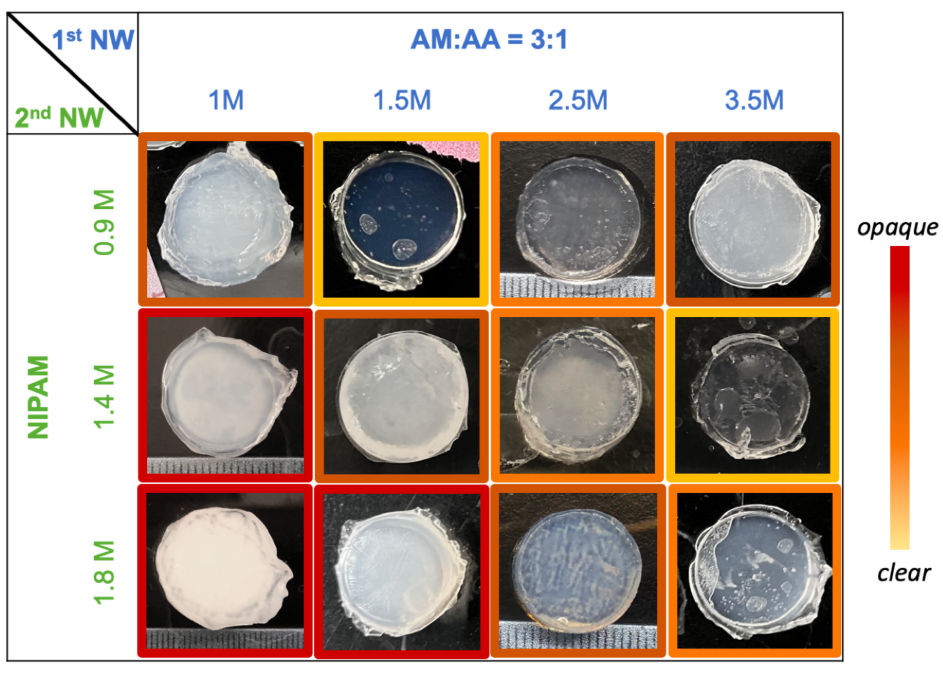

Table 3.1: Sample formulations and optical images of P(AM-co-AA)/PNIPAM IPNs for DSC.

For our initial exploration of the PAA/PNIPAM system, we found that the obtained IPNs are highly opaque and have inconsistent LCST behaviors ranging from 30 ^{o}C to 49 ^{o}C. With a low 1st network monomer molarity (1.5M), the LCSTs are seen near 32 ^{o}C (Table D.1a and Figure D.1)a. The opacity is likely due to a decrease in water solubility and an increase in hydrophobicity of the IPNs. With a relatively high 1st network monomer molarity (3.5M), the LCSTs are shifted to

48–49 ^oC (Figure D.1)c). With a moderate 1st network monomer molarity (2.5M), unexpected exothermic peaks at ~30^oC are observed, possibly due to rearrangement of water molecules and the polymer networks to reach an energetically-favorable configuration. Further investigation is needed to confirm this hypothesis.

To improve the LCST transition behavior, we hypothesize to replace the PAA network with a more hydrophilic network. Acrylamide (AM) is selected to replace acrylic acid (AA) because the hydrophilicity of the amide of NIPAM is higher than the ester functional group.[89] While keeping the molarity of the 2nd network monomer constant at 0.9M, Figure 3.6 shows emergence of LCST with copolymerization of AM and AA in the 1st network. For a temperature range of 25–60^oC, no thermoresponsiveness is seen when the first copolymer network consists of 75 mol% AA. Increasing AM content in the first network increases the compatibility between the first and second networks, reducing polymer-polymer phase separation and resulting in the emergence of a polymer-liquid phase transition and LCST at approximately 33°C. The IPN with a mole ratio of AM:AA = 3:1 shows the most promising LCST transition, which reveals that increasing the hydrophilicity of the first network promotes the coil-globule transition of PNIPAM.

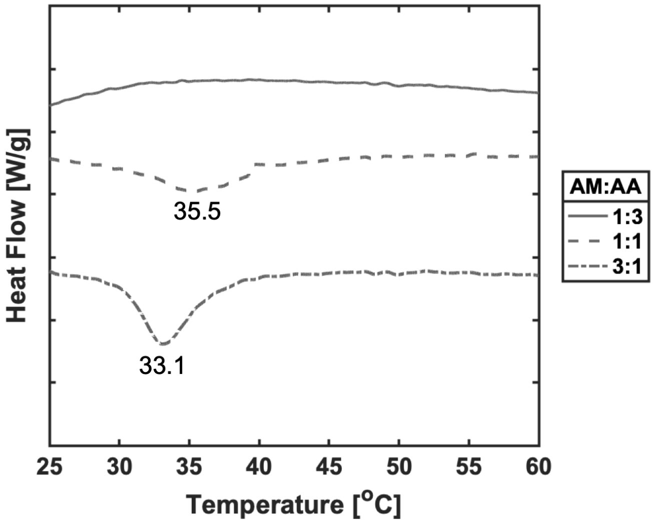

Figure 3.6: DSC measurements of P(AM-co-AA)/PNIPAM IPNs with varying AM:AA ratios. The molarity of 2nd network monomer (NIPAM) is fixed at 0.9M while the AM:AA ratios vary from 1:3, 1:1 to 3:1.

With AM:AA ratio at 3:1, several 1st and 2nd network monomer concentrations have been explored for further optimization of P(AM-co-AA)/PNIPAM IPNs. In Table 3.1, images of the IPNs made with 3DP first-network pucks are shown with the respective monomer concentrations for both networks. The opacity of the samples suggests some degree of phase separation between the two networks. With 1.5M first network molarity, increasing NIPAM loading leads to an increase in turbidity and the samples transition from highly transparent to a nearly opaque state. It is observed that increasing NIPAM loadings lead to an increase in turbidity. When the total monomer concentration of 1st network is 1.5M and 2.5M, the samples become opaque as the monomer concentration of the 2nd network solution increases (Table 3.1).

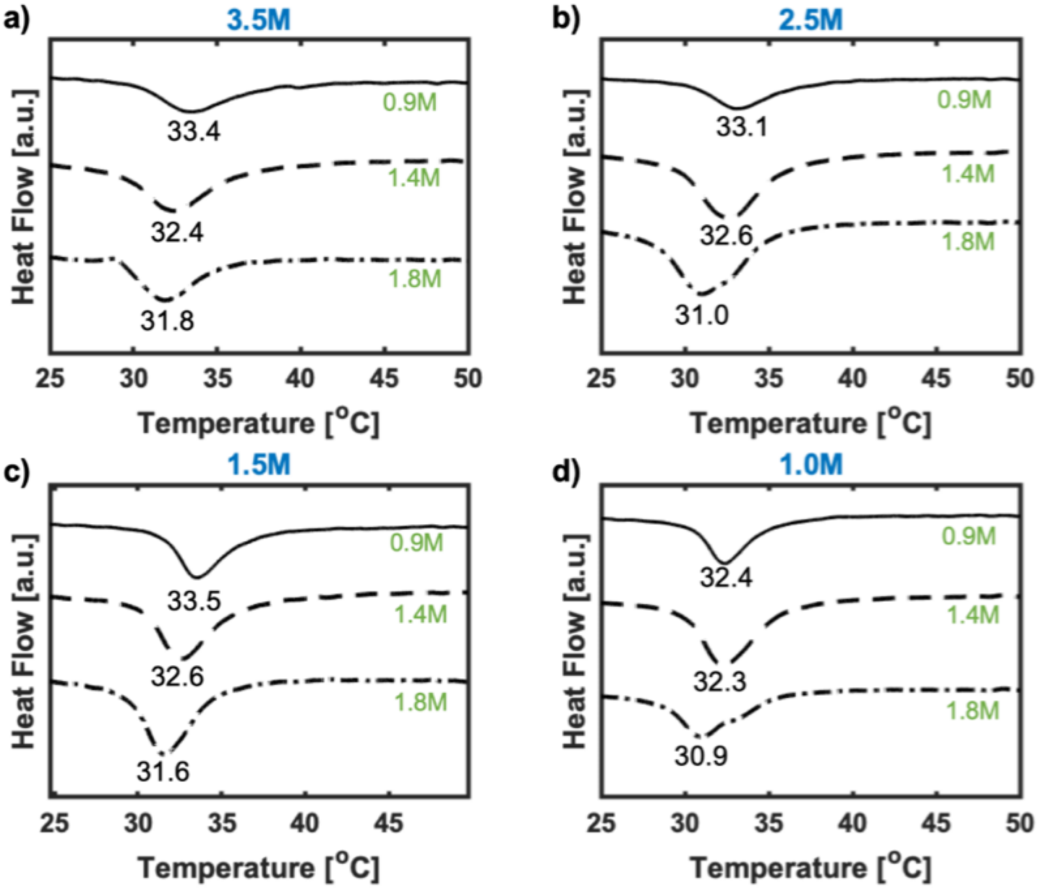

Figure 3.7: DSC measurements of thermoresponsive P(AM-co-AA)/PNIPAM IPNs with 1st network comonomer molarity of a) 3.5M, b) 2.5M, c) 1.5M and d)1M. The mole ratio of AM:AA = 3:1. The concentration of 2nd network monomer (NIPAM) varies from 0.9M, 1.4M to 1.8M for all four sets.

Figure 3.7 shows the effects of first and second network monomer concentrations on the DSC profiles of the completed IPNs. Increasing the first network concentration results in a broadening of the LCST endothermic peak. As the interaction between the first and second networks increases with increasing first network concentration, the thermodynamics of polymer-liquid phase separation are expected to change at different length-scales, resulting in the broadening of the LCST consistent with literature.[64] In gels of pure thermoresponsive material, the entire gel structure can energetically undergo the polymer-liquid phase separation at a single well-defined temperature. In an IPN, the thermoresponsive second network can undergo phase separation of a lower temperature at small polymer length scales where the polymer chains are not hindered by the host network. But at larger length scales that require more significant polymer reorganization and accommodation of the host network, a greater entropic driving force and higher temperature is necessary to drive the phase transition. The result is broadening of the LCST.

Unlike the PAA/PNIPAM IPNs, it is found that changing the first network concentration has little effect on the DSC profiles beyond broadening the LCST, which indicates greater compatibility between the first and second networks in the P(AM-co-AA)/PNIPAM IPNs. A great compatibility comes from a high cross-linking ratio of IPNs, which indicates a high degree of interpenetration in IPNs, particularly good connectivity of the networks.[90] Furthermore, because the materials can still experience a thermoresponse and phase transition at a higher first network concentration, this system is more amenable to architecting because the 3D printed first network is stronger and more resilient to the sequential IPN fabrication process.

Varying the 2nd network concentration shifts the LCSTs to lower temperatures. This may be a result of two combined effects. Firstly, increasing the concentration of the second network leads to a higher PNIPAM content in the IPN, reducing the size of the collapsed polymer structure following polymer-liquid phase separation. Secondly, increasing the PNIPAM concentration in the 2nd network also increases the hydrophilicity of the IPN at temperatures below its LCST, allowing it to swell with more water, which has been reported to decrease the LCST due to increased polymer mobility.[64]

3.4.3 Characterization of 1st Network Gel Crosslinking Density

The crosslinking density, n, of the 1st network hydrogels can be characterized using the Flory-Rehner equation,

$$-[ln(1-v_p)+v_p+\chi_o v_p^2] = V_o D_p n(v_p^{\frac{1}{3}} - \frac{v_p}{2}) \tag{3.1}$$

where v_p is the volume fraction of polymer in the swollen mass, V_o is the molar volume of the solvent (18 cm^3/mol for water), D_o is the density of polymer (1.41 g/cm^3 for PAA and 1.30 g/cm^3 for PAM), and χ_o is the Flory solvent-polymer interaction term that is specific to the polymer-solvent pair (0.41 for PAA-water and 0.495 for PAM-water).[91–93] Specific volume v_p is obtained as

$$v_p = \frac{1}{1+Q} \tag{3.2}$$

and

$$Q = \frac{m_s \cdot D_p}{m_p \cdot D_o} \tag{3.3}$$

where m_s is the mass of solvent in the swollen polymer, m_s is the weight of the polymer and D_o is the density of solvent ($1g/cm^3$ for water). Upon measuring parameters of the welled and hydrated states of the PAA and PAM 1st network gel, the degree of swelling is calculated by dividing the weight of the swelled hydrogel by the weight of the dried gel. The degree of swelling for 1st network gels as a function of crosslinking density are plotted in Figure 3.1. With the same monomer molarity, the PAM samples are more crosslinked, likely due the higher molar reactivity of AA that lead to longer chains between two crosslinking points. As expected, the crosslinking density increases with increasing monomer concentration and leads to a decrease in the degree of swelling.

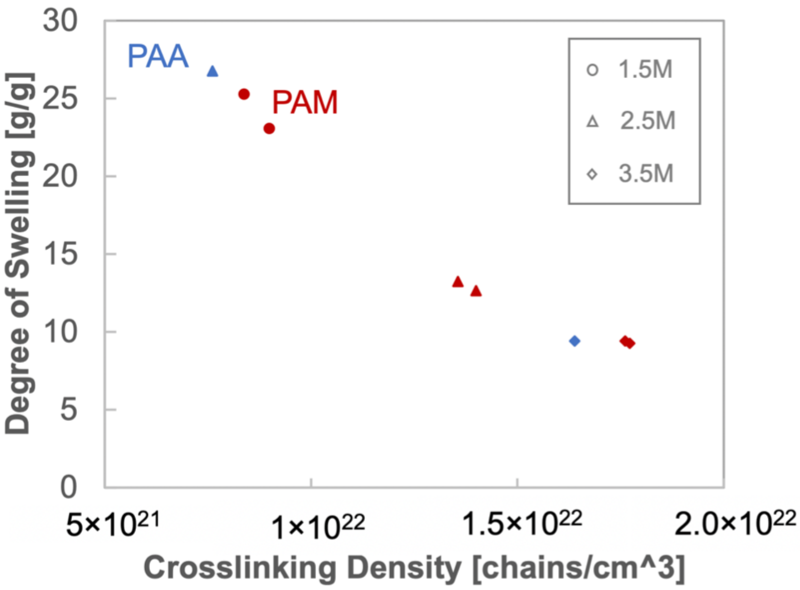

Figure 3.8: Degree of swelling for 1st network gels as a function of crosslinking density obtained using Flory-Rehner equation. The volumes and masses of samples with different monomer molarities (1.5M, 2.5M, and 3.5M) have been measured at both the fully hydrated and dehydrated states.

3.4.4 Volumetric Change Measurements

Volumetric shrinkage of IPNs upon heating above their LCSTs have been measured to characterize their water release performance. The schematic diagram in Figure 3.9a illustrates the expected water release behavior where the PNIPAM network undergoes conformational collapse above LCST and repels water out of the polymer networks. Figure 3.9b and c are representative photos that show tht two types of thermoresponsive behaviors have been observed. First, when the water release rate overcomes the rate of water evaporation, a small pool of water is collected at the base of the IPNs; in this case, the volumetric shrinkage is relatively large and the process occurs within seconds. Second, the IPN rapidly turns from transparent to opaque and the volumetric shrinkage is small. No liquid water is observed to be released from the IPN and volumetric shrinkage is mainly attributed to evaporation. Both of these behaviors are reversible; when placing the sample back to room temperature water, the sample returns to its original state. Moreover, both cases provide qualitative evidence that PNIPAM has been incorporated into that material to form an IPN.

1st NW 2nd NW		AM:AA = 3:1			
		1M	1.5M	2.5M	3.5M
NIPAM	0.9 M	60% ± 5%	71% ± 4%	25% ± 2%	31% ± 2%
	1.4 M	68% ± 5%	61% ± 4%	43% ± 1%	29% ± 2%
	1.8 M	46% ± 2%	70% ± 2%	29% ± 3%	27% ± 3%

Table 3.2: Volumetric Change of IPNs at 50^{o}C. A total of 12 compositions have been accessed with different 1st and 2nd network (co)monomer concentrations. The volumetric shrinkage of 4–5 samples for each composition have been measured.

The volumetric shrinkage of IPNs is reported in Table 3.2. It has been observed that the samples with volumetric change less than 50% do not release significant amount water when heated in air, suggesting that the volumetric change is mainly driven by evaporation. For more accurate and repeatable measurements, the values in Table 3.2 are obtained after placing the sample in a 50^{o}C water bath. It is interesting to note that increasing the molarity of the 2nd network does not have a drastic effect

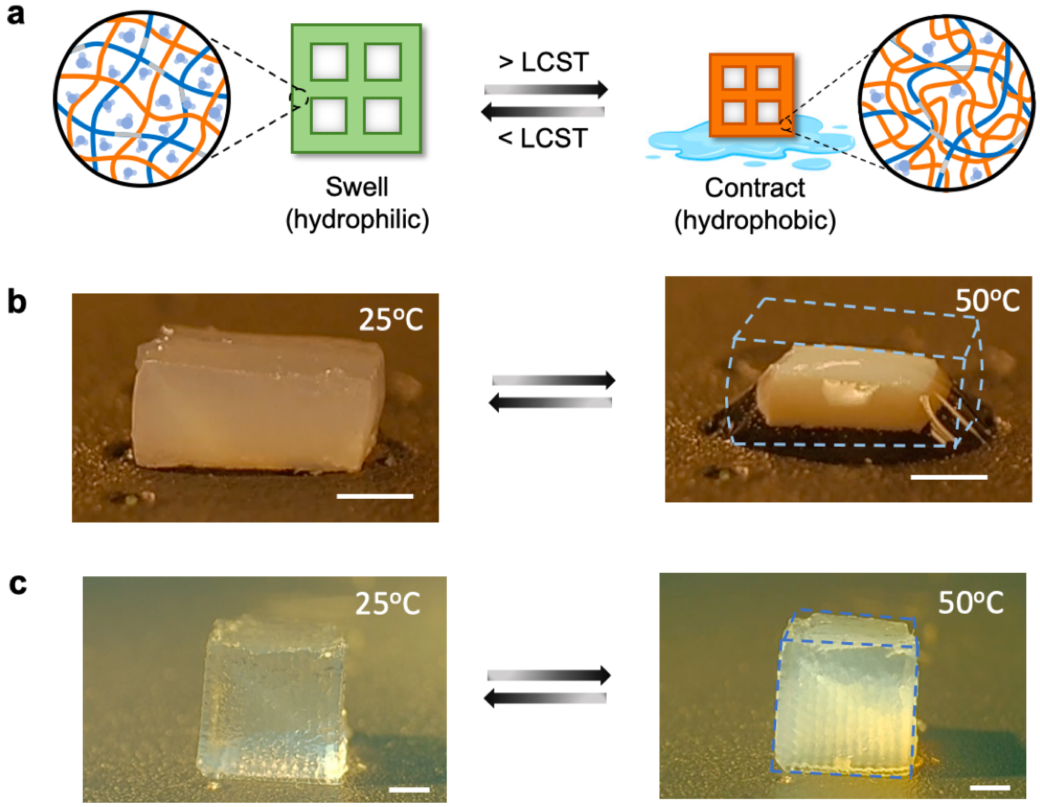

Figure 3.9: Thermoresponsive P(AM-co-AA)/PNIPAM IPNs undergoing LCST phase transition shown using a) schematic diagram, b) images of IPNs with relatively large volumetric shrinkage, and c) images of IPNs with relatively small volumetric shrinkage before and after heating above LCST. Scale bars are 1 mm.

on the volumetric shrinkage. However, the change in volume varies significantly with different 1st network monomer molarities, suggesting the swellability of the 1st network gels affecting the volumetric change of IPNs. For example, the IPNs with a 1st network molarity of 1.5M has the largest volumetric change of 60–70%. This observation is consistent with the DSC data; only very minor shift and intensity change of the LCST peak have been observed when increasing the 2nd network molarity.

3.5 Dynamic Mechanical Analysis

Dynamic Mechanical Analysis (DMA) of IPNs have been conducted on a TA Instrument Q850 Dynamic Mechanical Analyzer using a standard submersion compression clamp filled with deionized water (diH2O). After a strain sweep to determine a strain value within the material's linear viscoelastic regime, frequency sweeps from 0.1Hz to 5Hz have been conducted. Three IPN systems (PAA/PNIPAM, PAM/PNIPAM and P(AM-co-AA)/PNIPAM) have each been tested at 30°C, 35°C, and 40°C to evaluate the storage modulus and loss modulus below and above the LCST of PNIPAM. All samples were preloaded with 0.3N of force and equilibrated at the preset temperature for 15 minutes before testing. Single-network and double-network hydrogels were fabricated in cylinders with dimensions of ~10mm diameter by ~5mm height and stored in deionized water (diH_2O) for at least 48 hours before testing.

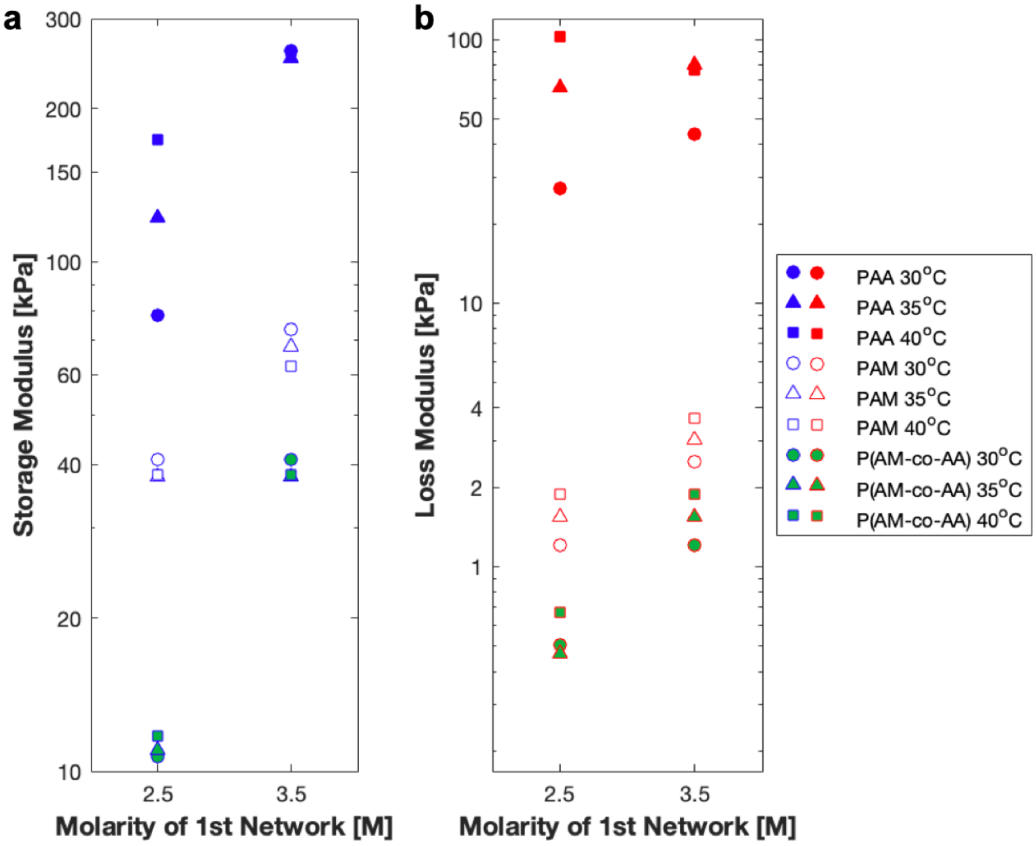

Figure 3.10: Storage and loss moduli of thermoresponsive IPNs at 1Hz. Three types of IPNs have been investigated, PAA/PNIPAM, PAM/PNIPAM, and P(AM-co-AA)/PNIPAM with AM:AA=3:1. IPNs were fabricated with 2.5M and 3.5M 1st network monomer concentrations while the 2nd network monomer concentration is controlled at 1.4M. Each sample is tested at 30°C, 35°C, and 40°C. Legend displays the 1st network material and the temperature in which the DMA test is conducted.

The obtained storage and loss moduli of IPNs with 2nd network NIPAM molarity fixed at 1.4M are shown in Figure 3.10. The storage moduli of all IPNs, regardless of the composition, are at least an order of magnitude higher than their loss moduli, meaning the IPNs behave more elastically, which is consistent with the behavior of high water content hydrogels. With 2.5M monomer concentration for the host network, PAA/PNIPAM IPN has the highest storage and loss moduli and the moduli of P(AM-co-AA)/PNIPAM are a magnitude lower than PAA/PNIPAM. The same trend is present for the 3.5M 1st network concentration. The moduli increased when the 1st network monomer molarity went from 2.5M to 3.5M due to a higher crosslinking density. Finally, the increase in temperature has also shown effects on the moduli. P(AM-co-AA)/PNIPAM and PAM/PNIPAM IPNs behave similarly when the temperature increases from 30^{o}C to 45^{o}C, except the storage modulus of PAM/PNIPAM is significantly higher. Within this temperature range, the loss modulus of these two IPNs have increased roughly by 50% and the storage modulus show a slight decrease. As determined by DSC, the LCSTs of the 2.5M P(AM-co-AA)/PNIPAM and the PAA/PNIPAM are around 32^{o}C. At a temperature above 32^{o}C, IPNs undergo volumetric shrinkage making the chains between crosslinking points looser and reducing the number of hydrogen bonding within the network in comparison to their fully swelled state; hence the storage modulus goes down and the loss modulus goes up. However, the PAA/PNIPAM IPNs behave differently; at 2.5M 1st network molarity, the storage and loss moduli have both increased. The 2.5M PAA/PNIPAM IPNs is a broad LCST peak between 35–50^{o}C (Figure D.1, which could have resulted in the continuous change in the storage modulus (79 kPa to 173 kPa) and loss modulus (27 kPa to 103 kPa) as the temperature goes from 30 to 45^{o}C. At 1st network molarity of 3.5M, the moduli are relatively unchanged with increasing temperature. This is likely due to the LCST of this composition is 48^{o}C and the temperature range tested here is not high enough to induce a mechanical response.

3.6 Summary on VP-enabled Thermoresponsive IPNs

In summary, we report a new way to fabricate thermoresponsive IPNs with assistance from a VP-based 3D printing system. By introducing a more hydrophilic monomer (AM) in the 1st polymer network at a molar ratio of AM to AA = 3:1, the obtained P(AM-co-AA)/PNIPAM IPNs exhibit consistent LCSTs near 32 ^{o}C which are not impacted by changing the 2nd network monomer concentration. By varying the total comonomer concentrations, stable architected IPNs have consistently displayed strong phase transition behavior and a tunable water release behavior with volumetric shrinkage between 30% and 70% upon heating above LCST. The temperature-dependent dynamic mechanical properties of the IPNs require further investigation which can potentially enable applications as thermoresponsive biomaterials.

Chapter 4

ADDITIVE MANUFACTURING OF DEGRADABLE ACRYLIC POLYMERS

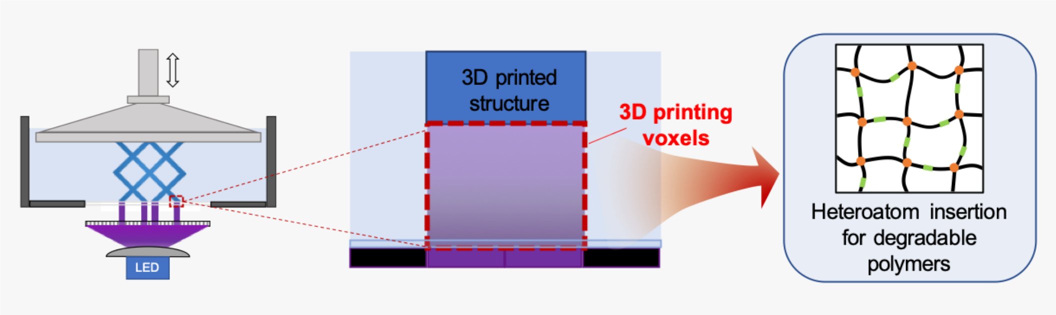

Figure 4.1: Schematic Overview of Chapter 4.

4.1 Motivation for Designing Degradable Materials Suitable for VP

One of the major environmental challenges of the 21st century is the buildup of plastic waste, which impacts the soil fertility, marine biology, and ultimately the global ecosystem.[94, 95] Only 14% of the global plastic usage for packaging is collected for recycling; particularly the recycling percentage in the U.S. is as low as 2%.[96] The vast majority of consumer plastic products are petroleum-based thermoplastics, such as polyethylene, polystyrene, and poly(vinyl chloride), all of which consist of nondegradable aliphatic hydrocarbon backbones making these materials environmentally unsustainable in the long-term. The global challenge has prompted the research and development of new sustainable polymeric materials in both academic and industrial sectors. One of the most widely used degradable, polylactide (PLA), is made with raw materials derived from the fermentation of plant matter, which is used as packaging materials, containers, service ware, waste-composting bags, and mulch films worldwide.[97]

With the rapid growth of AM technologies, the global revenues from AM products, services, and material sales have grown exponentially in the past decade, which have exceeded 10 billion USD annually in 2018 and is forecasted to be 23 billion USD by 2029.[5, 98, 99] A significant portion of these revenues are polymeric materials arising from growing AM fields in consumer products (e.g., automotive parts and shoes) and specialty products (e.g. medical/surgical parts and digital density).

3D printed products arranged from surgical guides to retainers and guards have revolutionized the field of dentistry. Align Technology, one of the largest 3D printing production facilities in the U.S. dedicated to printing, produces over half a million unique 3D printed parts with high precision per day using VP-based 3D printing technologies such as stereolithography (SLA) and projection μ-stereolithography (PμSL).[100]

In comparison to traditional manufacturing processes, AM processes afford significant improvements in production cost, energy consumption, re-usability of raw materials, and manufacturing lead times, which prompt more efforts to optimize this technology to have higher efficiencies and lower environmental impacts.[99] One of these efforts is the development of new sustainable materials for AM. While 3D printing has already shown various potential applications in medicine, dentistry, and consumer goods production, the studies that focus on the design, fabrication, and properties of (bio)degradable polymeric materials, and products become extremely important and relevant. As discussed in Chapter I, most AM techniques have limitation on the type of materials that can be fabrication, whereas VP offers a large design space for new material exploration via Photopolymerization. (Figure 1.3)

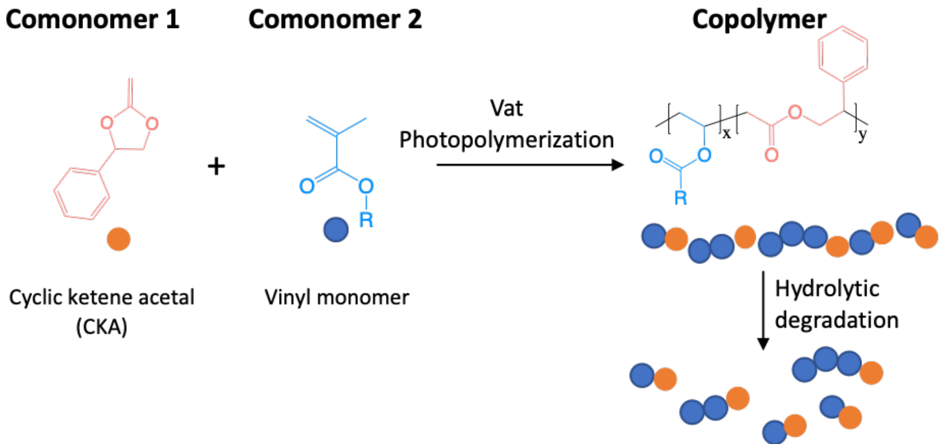

Figure 4.2: Schematic of Degradable Polymer for VP.

In this chapter, a new way to improve the degradability of commercially available photoresins for VP is investigated by introducing cyclic ketene acetals (CKAs) via olefin metathesis polymerization (OMP) into vinyl- or acrylate-based phototresins (Figure 4.2). Although there are many photoresins for AM that have already been optimized in terms of printability, processability, and mechanical functionalities, the obtained polymers consist of aliphatic hydrocarbon backbones that are not degradable. OMP allows incorporation of heteroatoms (oxygen or nitrogen atoms) to the polymer backbone which can undergo degradation upon being exposed to various stimuli (e.g. pH, thermal, or enzymatic).[101] The investigation in this chapter is focused on using CKA as an additive for commercially available photoresins to enhance the degradability of polymers obtained by VP, thus to alleviate the environmental impact of AM polymers in the long term.

4.2 Introduce Radical Ring Opening Polymerization to VP Processes

Chain growth polymerization (CGP), which describes a process of polymer formation through successive addition of monomers to an active site, is the most fundamental mechanism that drives the VP processes. Free radical polymerization (FRP) and cationic polymerization are two most common types of CGP utilized in VP, where different photoinitiators are required to enable the two different processes.[102] Cationic photoinitiators are used to initiate the photopolymerization of epoxy resins, whereas free radical photoinitiators are commonly used in the photopolymerization of acrylate or vinyl based resins.

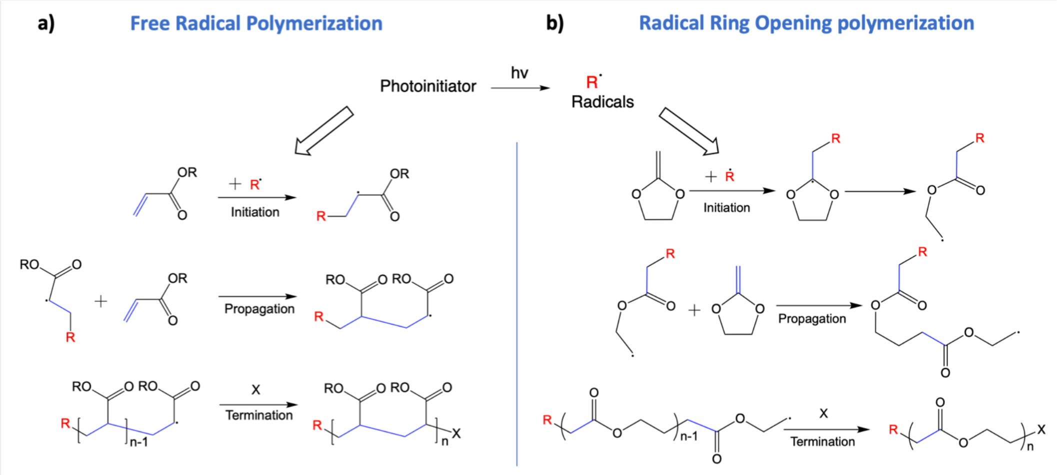

Figure 4.3: Comparison of Free Radical Polymerization and Radical Ring Opening Polymerization.

Figure 4.3a describes a standard free radical polymerization process that includes the initiation, propagation, and termination steps. Upon UV irradiation, the photoinitiators, which are small molecules that are sensitive to light, undergo photochemical cleavage to generate reactive species (free radicals) that can initiate the photopolymerization process. Once the free radical reacts with a monomer, a new radical is generated and serves as the active site for subsequent monomer addition to form a polymer chain; this step is known as chain propagation. Finally, the reactive intermediates generated in the propagation step would reach the end of their chain growth via recombination or disproportionation. In a recombination step, radicals from two reactive chain intermediates combine and form a covalent bond to create a stable polymer. In a disproportionation step, one radical transfers a hydrogen atom to the other to form two stable molecules and bring the chain growth to a halt. Similarly, the cationic polymerization process also contains four steps generally. The main difference between the two polymerization processes is that in the free-radical polymerization process the cations act as the reactive center throughout the entire polymerization process without charge transferring to another molecule.

Radical ring opening polymerization (rROP) is a specific type of radical polymerization that involves cyclic monomers with vinyl or exomethylene groups being polymerized though a ring opening mechanism.[103, 104] Various types of cyclic monomers are compatable with rROP, such as cyclic ketene acetal (CKA), thionolactones, and macrocyclic monomers. rROP allows the incorporation of labile functional groups (e.g., ester, thioester, disulfide, etc.) into the backbone of vinyl polymers to obtain (bio)degradable materials. As shown in Figure 4.3, rROP also contains four steps during the polymerization process which are analogous to the free radical polymerization process.

As discussed in a 2017 review by Tardy et al., shrinkage stress can be created during polymerization reaction when liquid resin becomes solid which can be build up continuously until the maximum percentage conversion has been reached. This can lead to volume contraction or material shrinkage due to replacement of Van der Waals distances between unreacted monomers with a shorter covalent bond along the polymer backbone.[104] AM processes suffer from this problem causing delamination during printing, warping, or/and cracking of the 3DP parts. Cyclic monomers are known to be able to compensate the shrinkage by the ring-opening mechanism where longer linear polymer segments are created and incorporated into the main chain. Thus, the higher the molecular weight of the cyclic monomer, the less shrinkage would occur during polymerization.

4.3 Copolymerization

Different monomers have different tendencies to undergo copolymerization. The amount of monomer being incorporated into a copolymer is determined by the relative concentration and the reactivities. The reactivity of the monomer, which is defined as a relative value derived from the measurements of the rate of the monomer addition to a specific reactive site, is ultimately determined by the chemical environment of the reactive functional group. As an result, the composition of the comonomer feed often deviates from the composition of the copolymer being produced. The discussion in this section is adapted from Chapter 6 from Odian's Principles of Polymerization.[105]

$$\begin{aligned}
M_1^{\bullet} + M_1 &\xrightarrow{k_{11}} M_1^{\bullet} \\
M_1^{\bullet} + M_2 &\xrightarrow{k_{12}} M_2^{\bullet} \\
M_2^{\bullet} + M_1 &\xrightarrow{k_{21}} M_1^{\bullet} \\
M_2^{\bullet} + M_2 &\xrightarrow{k_{22}} M_2^{\bullet}
\end{aligned}$$

Figure 4.4: Two types of chain propagation: self-propagation and cross-propagation. M_1 and M_2 represent two different types of monomers where k_{ij} is the rate constant of each propagation type. i represents the type of monomer that the reactive species is ending with, whereas j represents the type of monomer being added.

To determine the copolymer composition, we can refer to $first\text{-}order\ Markov$, known as the $terminal\ model$, which assumes that the chemical reactivity of the propagating chain only depends on the monomer unit at the growing end and does not depend on the chain composition before the active unit. Copolymerization of two different monomers (M_1 and M_2) can lead to two types of propagation species: the same monomer being added to a reactive site of itself or to a reactive site ended in the other type of monomer. As shown in Figure 4.4, monomers M_1 and M_2 can each add either to a propagating chain ending in M_1 or to one ending in M_2. Monomer M_1 can add to a reactive site made of M_1 to generate a new reactive site of M_1; this is known as self-propagation. M_1 can also add to a reactive site made of M_2 to create a new reactive site of M_2; this is known as cross-propagation. Similarly, if M_2 is being added to an reactive site of M_1, a new M_1 active site is generated; and if M_1 is being added to an reactive site of M_2, a new M_2 active site is generated. The rate constant, k_{11}, gives the rate of a propagating chain ending in M_1 adding to monomer M_1, and k_{12} is for a propagating chain ending in M_1 adding to monomer M_2, and so on. Molar reactivity ratio, r is defined as

$$r_1 = k_{11}/k_{12} \tag{4.1}$$

$$r_2 = k_{22}/k_{21} \tag{4.2}$$

where r is a dimensionless value. Derived from the rates of disappearance of the two monomers or their rates of incorporating into the copolymer, the mole fraction of M_1 and M_2 in the copolymer (F_1 and F_2, prospectively) can be determined as

$$\frac{F_1}{F_2} = \frac{f_1(r_1 f_1 + f_2)}{f_2(r_2 f_2 + f_1)} \tag{4.3}$$

where f_1 and f_2 are the mole fractions of monomers M_1 and M_2 in the feed and F_1 and F_2 are the mole fractions of monomers M_1 and M_2 being incorporated in the copolymer. Alternately, the mole fraction of one monomer in the obtained copolymer can be derived to be

$$F_1 = \frac{r_1 f_1^2 + f_1 f_2}{r_1 f_1^2 + 2 f_1 f_2 + r_2 f_2^2} \tag{4.4}$$

and F_2 can be obtained by substituting Equation 4.4 into Equation 4.3 .

4.3.1 Ideal Copolymerization.

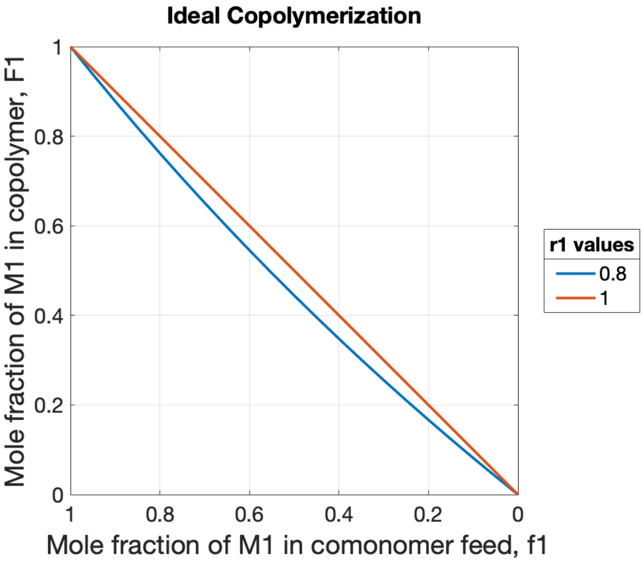

Figure 4.5: Ideal copolymerization.

Ideal copolymerization is characterized when the product of the two molar reactivity ratios equal one: $r_1 \cdot r_2 = 1$. A copolymerization is called *ideal*, when the probabilities of the two propagating species $M_1\cdot$ and $M_2\cdot$ adding one or the other of the two monomers are identical. As shown in Figure 4.5 (red line), the mole fraction of one monomer in the feed is the same as the mole fraction of the monomer in the resulted copolymer in such copolymerization. When r is close to 1 (e.g. $r_1 = r_2 = 0.8$), the mole fraction of the monomer in the feed still closely reflects the mole fraction in the copolymer (blue line in Figure 4.5).

4.3.2 Alternating Copolymerization

Alternating copolymerization is defined with $r_1 \cdot r_2 = 0$, where neither r_1 nor r_2 is greater than 1. There are two types of alternating behaviors:

1) $Extreme\ alternating\ behavior : r_1 \cdot r_2 = 0$

$M_1\ M_2\ M_1\ M_2\ M_1\ M_2\ M_1\ M_2\ M_1\ M_2\ M_1\ M_2\ ...$

2) $Moderate\ alternating\ behavior : 0 < r_1 \cdot r_2 << 1$

$M_1\ M_2\ M_1\ M_2\ M_2\ M_1\ M_2\ M_1\ M_1\ M_2\ M_1\ M_2\ ...$

Extreme alternating polymerization occurs when $r_1 = r_2 = 0$, that is, $M_1\cdot$ only adds M_2 and $M_2\cdot$ exclusively adds M_1. In this case, the mole fraction of monomer in the copolymer can be reduced to $F_1 = F_2 = 0.5$. Moderate alternating behaviors happen when either 1) the r_1 and r_2 values are very small and the product of r_1 and r_2 is close to zero or 2) one r value is small and the other r is zero. As shown in Figure 4.6, when both r_1 and r_2 are small values or one of r values is zero, the mole

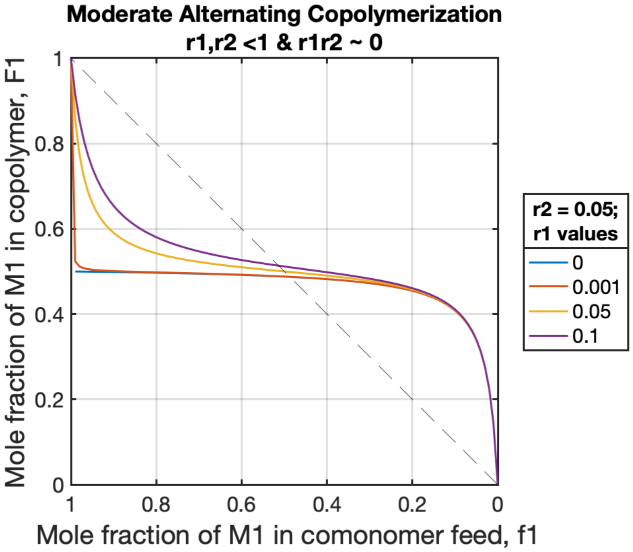

Figure 4.6: Alternating copolymerization.

fraction of each monomer in the copolymer stays close to 0.5 over a large range of mole fraction of the monomer in the feed. In this case, the monomer composition in the feed does not have a dramatic effect on the monomer mole fraction in the copolymer.

4.3.3 Copolymerization of CKA and Vinyl Monomer

Copolymerization of CKAs and vinyl and acrylic monomers has been widely studied to create functional and degradable polyesters in the recent years. The majority of the studies involved complicated synthesis, such as nitroxide-mediated rROP, thermally activated radical polymerization, and reversible addition fragmentation chain-transfer polymerization, which require elevated reaction temperatures, inert reaction environments (e.g. nitrogen), or/and prolonged reaction times (e.g. 8–24 hours), where the obtained polyesters can undergo hydrolytic (e.g. acidic, alkaline, or nearly neutral conditions) or enzymatic degradation (e.g., lipase or proteinase K).[101, 103, 104, 106, 107] Pesenti and Nicolas [103] and Tardy et al. [104] published comprehensive reviews on the history of rROP and the recent advancements on degradable polymers from rROP.

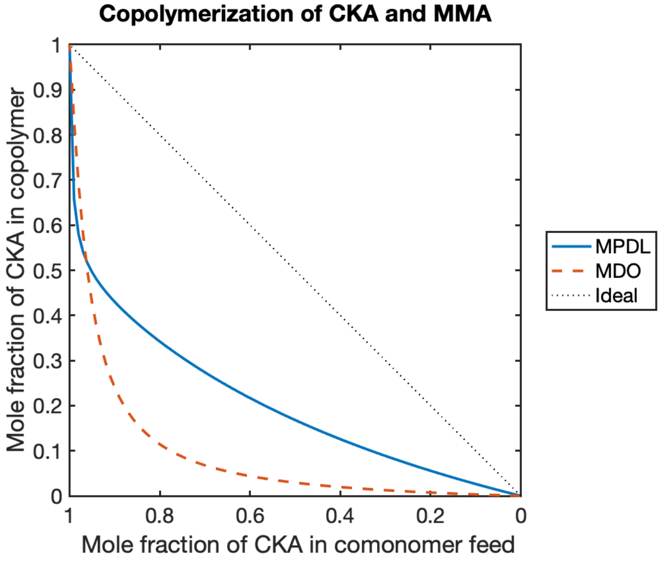

Figure 4.7: Copolymerization of CKA and MMA. The molar reactivity ratios of MPDL and MDO with respect to MMA have been obtained from previous literature.[108, 109]

The molar reactivity ratios of a copolymer pair can be experimentally determined from copolymer compositional analyses by non-linear least squares fitting.[110] Two CKAs have been frequently studied to copolymerize with acrylates, which are 2-

methylene-1,3-dioxepane (MDO) and 2-methylene-4-phenyl-1,3-dioxolane (MPDL) ; their chemical structures are shown in Figure 4.10. MPDL has been determined to be more reactive towards poly(methyl methacrylate) (PMMA) radicals (r_{MPDL} = 0.01 and r_{MMA} = 4.0) while comparing to the reactivity of MDO with the same methacrylate monomer (r_{MPDL} = 0.057 and r_{MMA} = 34).[108, 109] Using the r values of MDO and MPDL when copolymerized with MMA, Figure 4.7 shows the plots of mole fraction of CKAs in the copolymer as a function of CKAs in the comonomer feed obtained by Equation 4.4. Although the amount of MPDL incorporated into the copolymer is much lower than that in the comonomer feed, MPDL is much more reactive than MDO when copolymerizing with MMA due to the ability of the phenyl group to stabilize the propagating radials (Figure 4.8).

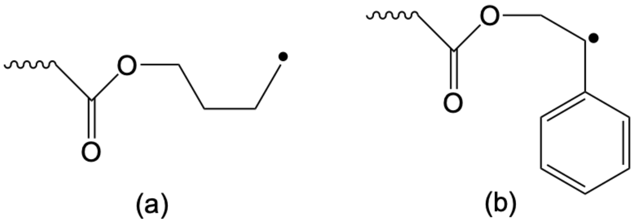

Figure 4.8: Structures of propagating radicals from (a) MDO and (b) MPDL polymerization.

Although the compositions of most commercially available photoresins are proprietary, Autodesk made the composition of their photoresin (PR 48), which has been considered as a widely used acrylate formulation in both industry and academia, has become open sourced in 2015.[21, 111] Figure 4.9 shows all the components in the PR48 photoresin and their weight percentages. It contains two types of acrylate-based oligomers (Sartomer SR 494 LM and Ebercryl 8210) in PR48 which are tetra- and bi-functionalized acrylates for crosslinking the polymer. Ebercryl 8210 has shown to improve the compliance of the obtained materials.[22] Besides the photoinitiator (TPO), whose function is to enable photopolymerization, the UV blocker (Mayzo OB+) is also present to reduce the penetrating dosage of the light giving rise to fine details and embossing in 3DP structures. Another component that takes up a large weight percentage in the resin is the reactive diluent (Genomer 1122), a mono-functionalized urethane acrylate, which can reduce the viscosity of the resin for processing.[112, 113] Besides enhancing degradability with ester insertion to polymer backbones, small organic molecules like CKAs can also reduce the viscosity of photoresin, in ways similar to reactive diluent. To best preserve the mechanical property of the photopolymer, the viscosity of the resin should not be

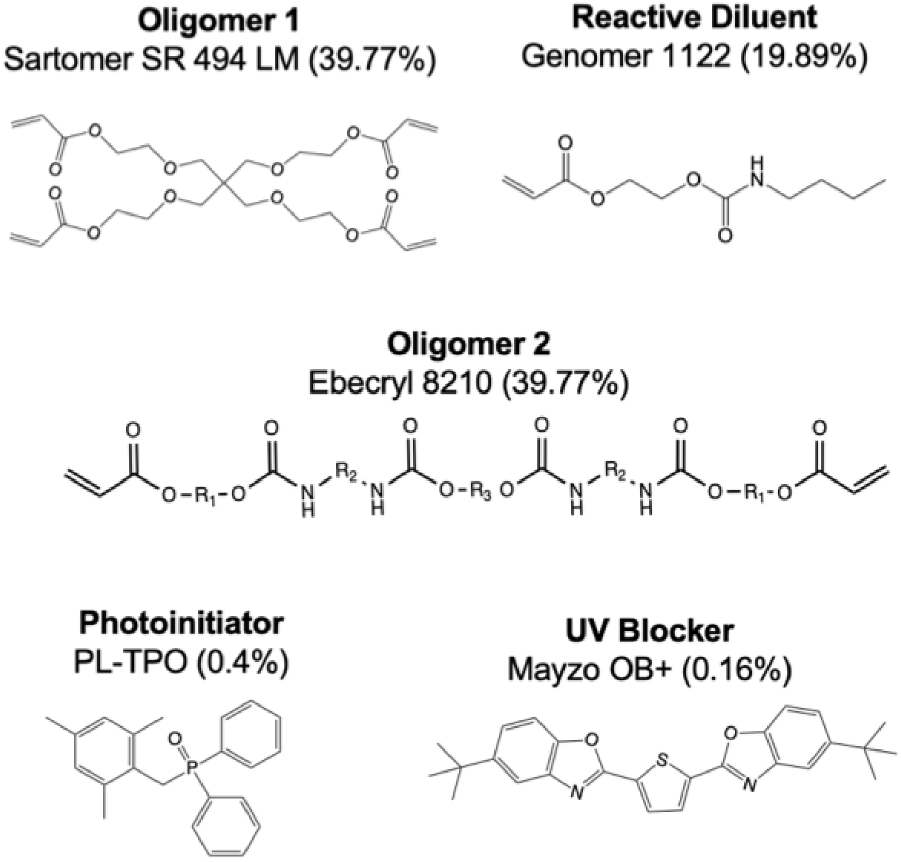

Figure 4.9: Chemical composition of Autodesk's photopolymer resin PR48 including trade name and weight percentage of each component.[21] Ebercyl 8210 is a commercially available UV-curable coating material and the exact chemical structure is proprietary, thus the chemical structures of segment R_1 and R_2 are unknown to the public.

changed drastically; therefore, only a small portion of the reactive diluent can be replaced by CKA to promote degradability.

In the following sections, we first conducted model studies on copolymerization of CKAs and vinyl or acrylic monomers to investigate the incorporation of CKA into carbon-carbon polymer backbone via photopolymerization. The synthesis was conducted in regular laboratory environment (not in inert gases) to ensure compatibility with VP processes. Once we confirmed that the CKAs can be sufficiently introduced into the main chain, we moved onto the bulk study on copolymerization of CKA and multi-functionalized acrylates and the resulted bulk material was treated under alkaline condition for degradation study.

4.4 Material Fabrication and Characterization

To incorporate CKAs into acrylate or vinyl containing system in experimental conditions that are analogous to the VP process, a model study has been conducted to synthesize linear polymers. Two CKAs have been selected, MDO and MPDL, to each to pair with methacrylate (MA) and vinyl acetate (VAc). MA is selected here instead of MMA due to the fact that most commercially available resins are acrylate based and the reactivity of MA is higher than that of MMA (orange line in Figure 4.13). On the other hand, VAc is selected due to its low reactivity in comparison to MA or MMA to promote the incorporation of CKA in copolymer. The chemical structures of comonomers are shown in Figure 4.10. Photoinitiator (TPO-L) is

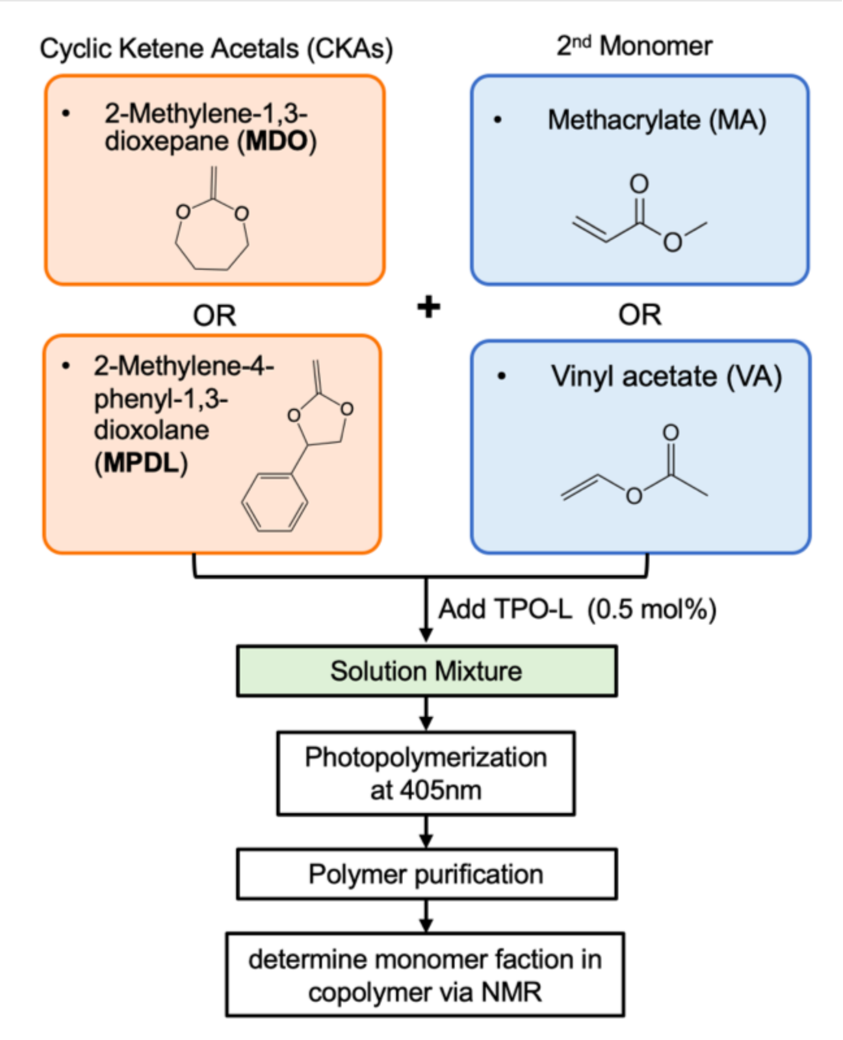

Figure 4.10: Chemical Structure of Comonomer Feed and Fabrication Steps for Model Study.

added at 0.5 mol% of the total comonomer content (1 mmol) to the monomer mixture in dimethylformamide (DMF) as solvent. After mixing of the components in a small optically transparent glass vial, the precursor solution mixture is purged under nitrogen for 5 minutes then is reacted under 405nm UV lamp (60W, Peopoly Inc.) for 60 seconds. The resulted polymer is then transferred to a dialysis membrane in 100mL methanol for 24 hours while methanol is being changed 3–4 times. Upon removing the solvent, the purified polymer is then dissolved in deuterated acetonitrile (CD_3CN) for ^1H NMR spectroscopy.

4.4.1 Model Study of Copolymerization of CKAs and MA

Following the fabrication steps described above, model studies of copolymerization of CKAs (MPDL and MDO) and MA have been conducted. Mole fractions of MPDL and MDO in their copolymers with MA have been calculated by ^1H NMR spectroscopy. As shown in Figure 4.12, the chemical shifts are assigned based on previously published values of similar polymer composition.[114, 115] The peaks that are unique signatures for each comonomer would be integrated to calculate the mole fraction of CKA in the copolymer. For P(MDO-co-MA), the methyl signal for MA (labeled with a) and the protons next to the ester oxygen from MDO (labeled with d) have the most downfield shifts at 3.5 ppm and 4.1 ppm, respectively (Figure 4.12a). After assigning the two d protons to be 1 and the three a protons integrated to be 163.91, the mole ratio of MDO in copolymer is calculated to be 1:109, which is significantly lower then the mole ratio of MDO to MA feed, n(MDO : MA) = 1:3.5. MPDL is known to be able to undergo ring-opening as well as vinyl-addition during polymerization, which gives rise to the peak near 5.1 ppm for the f proton in Figure 4.11.[116] To calculate the mole fraction of MPDL in copolymer via ring-opening

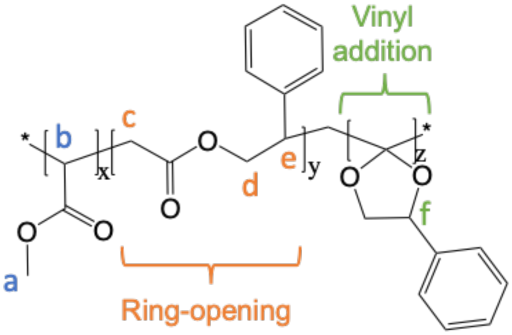

Figure 4.11: Polymer structure of p(MPDL-co-MA) with vinyl addition.

mechanism, the phenyl signal from vinyl addition needs to be subtracted. Together with the integrated values of $-CH_3$ from MA and the corrected phenyl signal, the

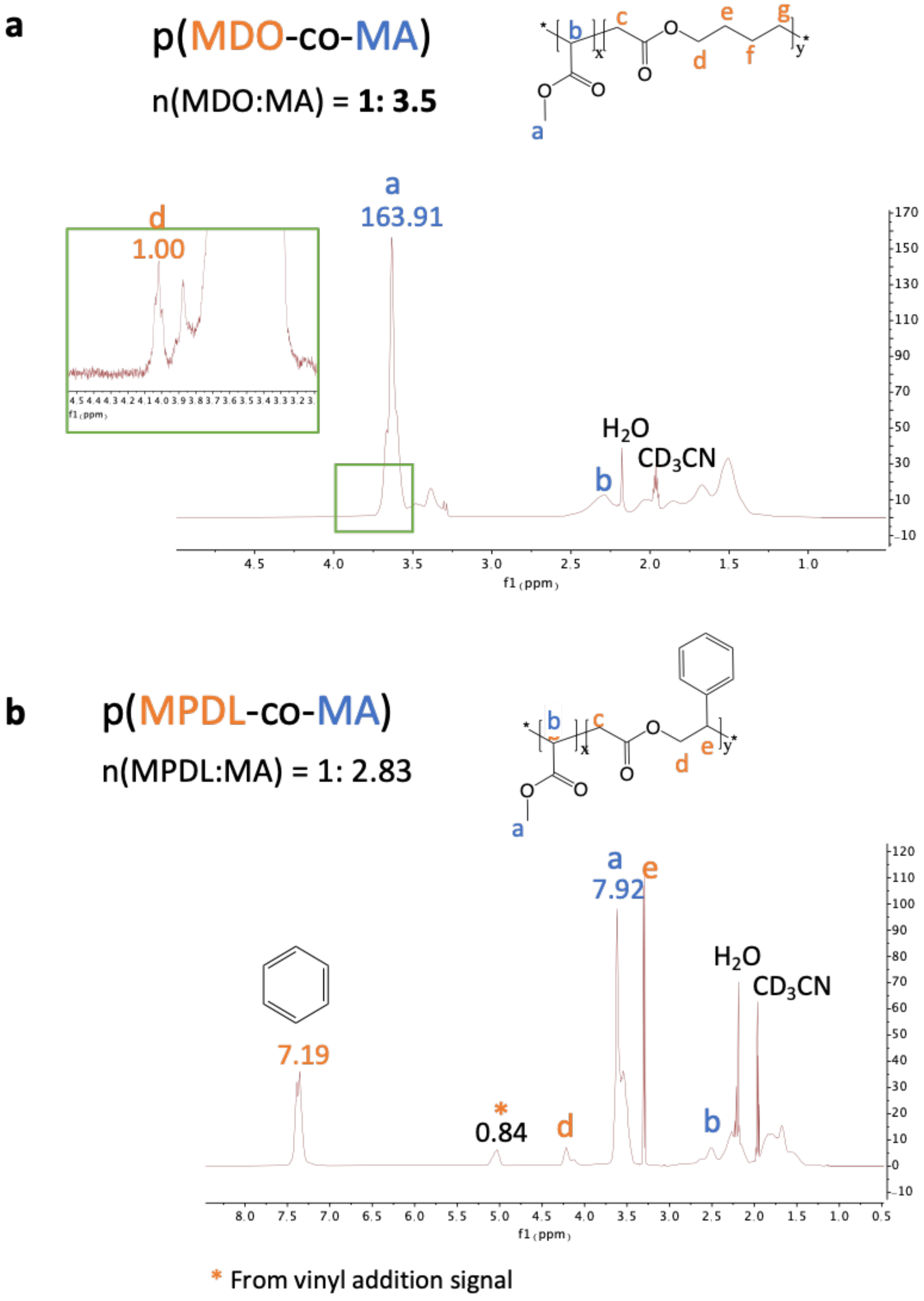

Figure 4.12: NMR of CKA-acrylate Copolymers via photopolymerization: a) MDO and MA copolymer and b) MPDL and MA copolymer. Chemical shifts have been assigned based on previous reported values.[114, 115]

mole ratio of MPDL via rROP is calculated to be 1:4.4, which is close to the mole ratio of the MPDL and MA in the feed, n(MPDL : MA) = 1:2.8. MPDL shows significantly better incorporation than MDO in copolymerization with MA. TPO-L has proven to be an effective photoinitiator for photopolymerization of CKA and acrylate.

4.4.2 Model Study of Copolymerization of CKAs and VAc

To improve the MDO incorporation in copolymer, vinyl acetate (VAc) is selected as the 2nd monomer because the VAc is less reactive than MA.(Figure 4.13). Hence, VAc is expected to have less competition with MDO during copolymerization and the mole fraction of MDO would be enhanced. A control polymer, p(VAc), has also been synthesized for easy chemical shift assignment of p(MDO-VAc) in the ^1H NMR (Figure 4.14a). In Figure 4.14b, the two most downfield shifts correspond to the -CH-O ester proton from VAc at 4.7 ppm and the two -CH_2-O protons from MDO at 4.1 ppm.[115] With the integrated value of these two shifts, the mole ratio of MDO to VAc in the copolymer is 1:3.3, which is close to the mole fraction of MDO and VAc feed, n(MDO:VAc) = 1:4. This result indicates that the incorporation of MDO improves drastically when MDO copolymerizes with the less reactive vinyl acetate as the 2nd comonomer. TPO-L is also shown to be effective to initiate a MDO and VAc photopolymer system.

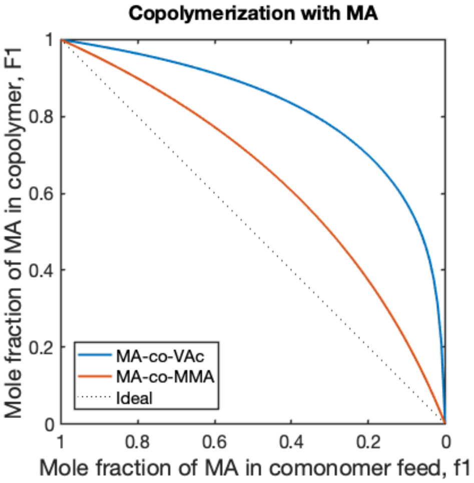

Figure 4.13: Copolymerization of MA with MMA or VAc.

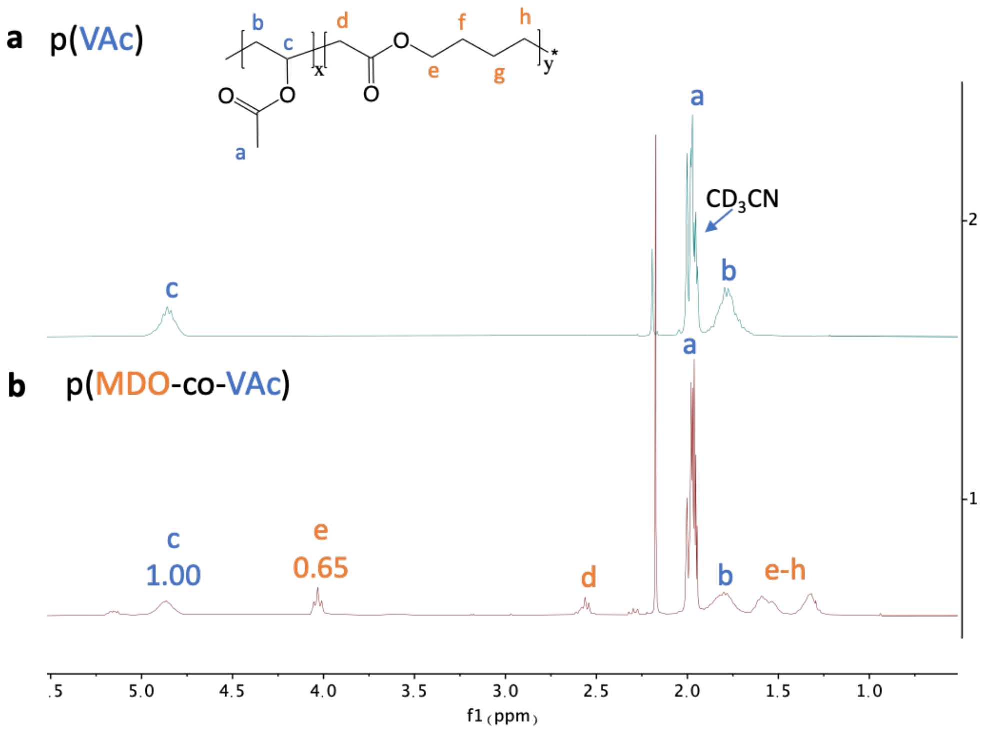

Figure 4.14: NMR of CKA-vinyl acetate Copolymers via photopolymerization: a) vinyl acetate polymer control and b) MDO and vinyl acetate copolymer.

4.4.3 Bulk Study of CKA incorporation

Based on the results obtained from the model studies of the rROP of CKA with acrylate and vinyl acetate initiated by TPO-L, we constructed the material system for the bulk study that includes methyl methacrylate (MMA) as the chain builder and poly(ethylene glycol) diacrylate (PEGDA, M_n 575) as the crosslinker to combine with one of the two CKAs (MDO AND MPDL) used in the model studies. Di- or multi-functionalized acrylates are commonly used in photoresins for VP due to their high reactivity and rapid reaction time. MMA is selected here due to its lower reactivity in comparison to MA, in hope to increase the mole fraction of CKA in bulk polymer (Figure 4.13).

The compositions of three representative samples are listed in Table 4.1 and the total amount of all components for each sample is kept at 1 mmol. All of these samples have been prepared in small quantities to emulate the curing volume for each layer in VP processes. Since PEGDA is fairly viscous, MMA and CKA also serve as reactive diluents, similar to the function of Genomer 1122 in the PR48 photoresin to reduce resin viscosity and improve processability (Figure 4.9). Upon mixing

Sample ID	CKA (mol%)	MMA (mol%)	PEGDA (mol%)
#1 (control)	-	37.5	62.5
#2	20 (MDO)	30	50
#3	20 (MPDL)	30	50

Table 4.1: Composition of Samples for Bulk Study.

the components, the mixture is purged in nitrogen for 5 minutes and followed by 45-second UV exposure by a 405nm wavelength lamp at 5cm distance; the obtained polymer is a clear and stiff solid. Although the UV source power and the geometry between sample resin and the UV source are not identical to those of a 3D printer, the curing time for the mixture can provide a rough estimate of the exposure time per layer for MDPL, and MDO have also shown good compatibility with 1,4-butanediol diacrylate to form clear solid polymers. Chemical structures of the crosslinkers using in this section are shown in Figure 4.15.

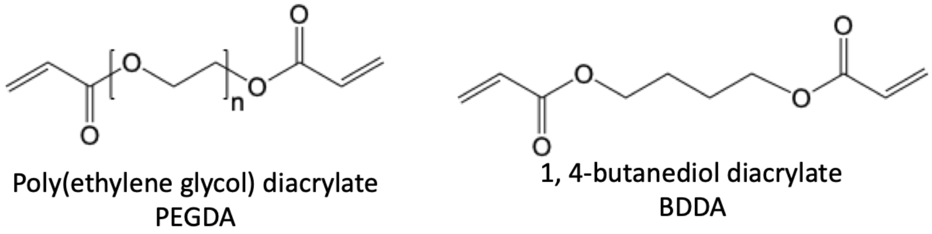

Figure 4.15: Chemical structure of crosslinkers for bulk study.

Unlike the linear copolymers, characterization of the CKA incorporation of these crosslinked photopolymer are more challenging. Comparing to MDO-enabled polymer, the bulk polymer with MPDL incorporation is more straightforward to identify because of the unique addition of the phenyl group. Since the aromatic functional group is more sensitive to Raman spectroscopy than IR spectroscopy, we have performed Raman spectroscopy on three samples that have been prepared under the same conditions previously described: a) control sample (2% PEGDA and 96% MA), b) Crosslinked MPDL polymer (20% MPDL, 3% PEGDA and 74% MA), and c) MPDL linear polymer (20% MPDL and 80% MA). TPO-L content is all kept at 0.5 mol% of the total mole of acrylates and CKAs. The resulted Raman spectra are shown in Figure 4.16. The overall chemical signature of the three samples is similar; however, the emergence of a band near 1000 cm^{-1} wavenumber for crosslinked MPDL polymer and MPDL linear polymer is consistent with strong ring-breathing vibration in mono-substituted aromatic compounds.[117] This indicates a successful insertion of MPDL into the crosslinked polymer network.

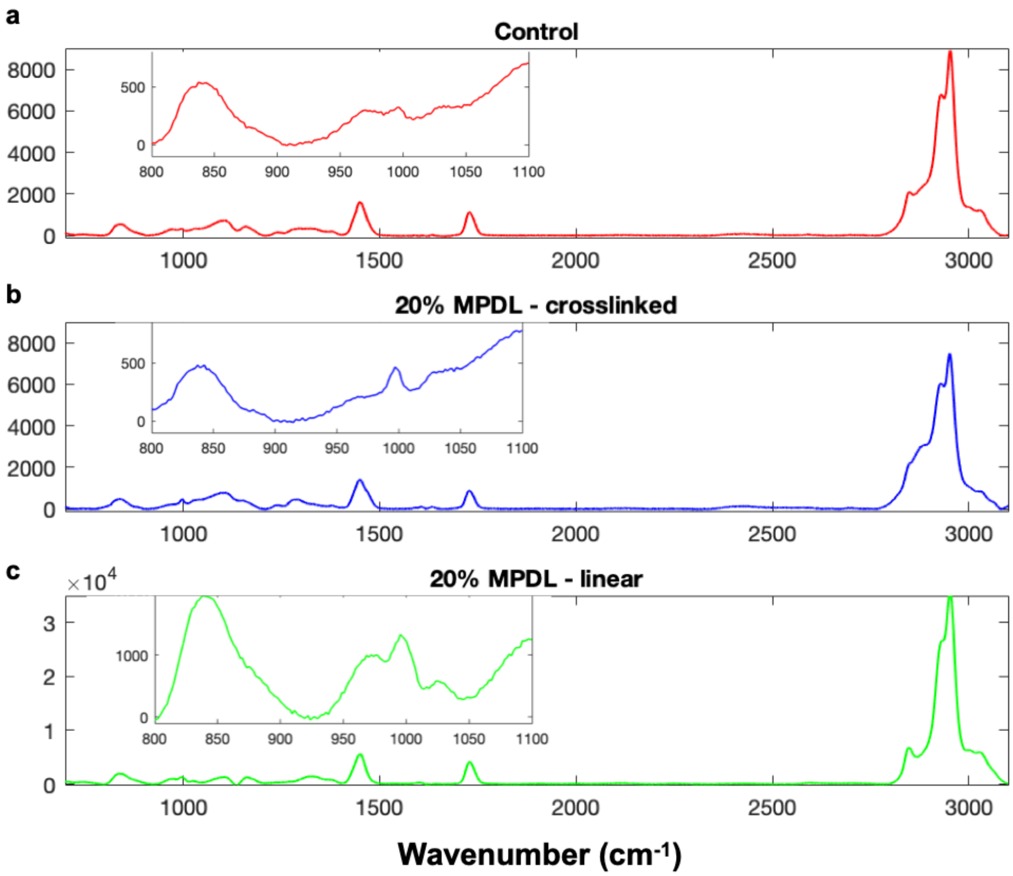

Figure 4.16: Raman spectroscopy of CKA-enabled photopolymer: a) control sample without CKA, b) crosslinked bulk polymer fabricated with 20 mol% of MPDL, and c) linear polymer fabricated with 20 mol% of MPDL.

4.5 Degradation Study

Once the obtained the solid polymers and confirmed the entry of CKA into the polymer network, we performed hydrolytic degradation studies in alkaline condition. The mass loss percentage has been calculated as the difference between the original sample mass and the lyophilized sample mass divided by the original sample mass. The degradation process involves the submerging of samples in 1N NaOH solution, washing and lyophilizing the sample before measuring the sample mass to complete the degradation cycle; the same cycle is repeated a number of times until the sample reach complete degradation (Figure 4.17). The degradation data of

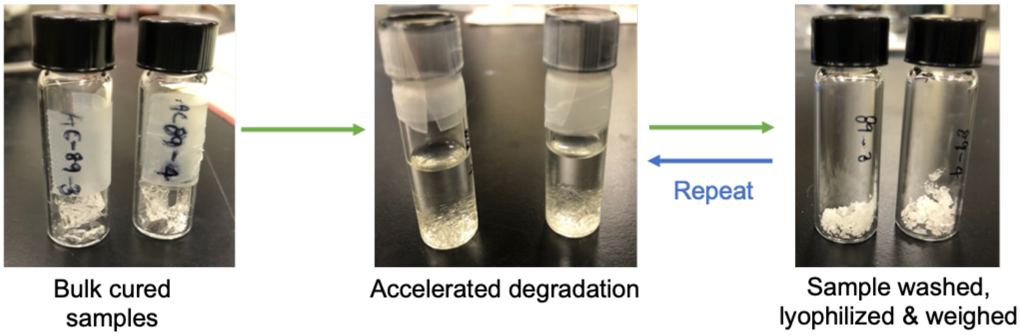

Figure 4.17: Degradation study of CKA-enabled photopolymer. Left image contains samples #2 and #3 listed in Table 4.17, each in a glass vial. Middle image shows the clear solid polymer samples submerged in 1N NaOH solution. Right image provides the sample appearance after they have been washed, lyophilized, and ready for weighing.

the three samples listed in Table 4.1 are shown in Figure 4.18 where photopolymer fabricated with MPDL displays the most rapid degradability, losing 84.4% of its original mass after under 7 hours of hydrolysis condition. The sample fabrication with MDO performed similarly well with a mass loss percentage of 79.3%. It is worth noting that the control sample has also experienced significant mass loss of 63.6% which is possibly due to the high content of PEGDA. As shown in Figure 4.15, the ester bonds of the acrylate functional groups are likely to break during the hydrolysis process, which gives the control sample the good degradation property.

4.6 Summary on Copolymerization with CKA for Degradable Polymer

In this work, we have demonstrated the compatibility of rROP of CKAs with compounds that are commonly used in photoresins for VP, such as multi-functionalized acrylate (crosslinker), TPO-L (photoinititator), and MA/MMA (chain builder). Out of the two CKA compounds have been used in this study, MPDL shows particularly high incorporation: 63.6% of mole fraction in the feed entered the acrylate based polymer backbone. With 20 mol% in the formulation, MPDL has also demonstrated its ability to improve the degradability of acrylate–based photopolymer by increasing the mass loss by approximately 21% during hydrolytic degradation. Due to its low viscosity and good reactivity with acrylates, CKAs have shown great potential in using a reactive diluent to improve the degradability of commercially available acrylate-based photopolymers for VP.

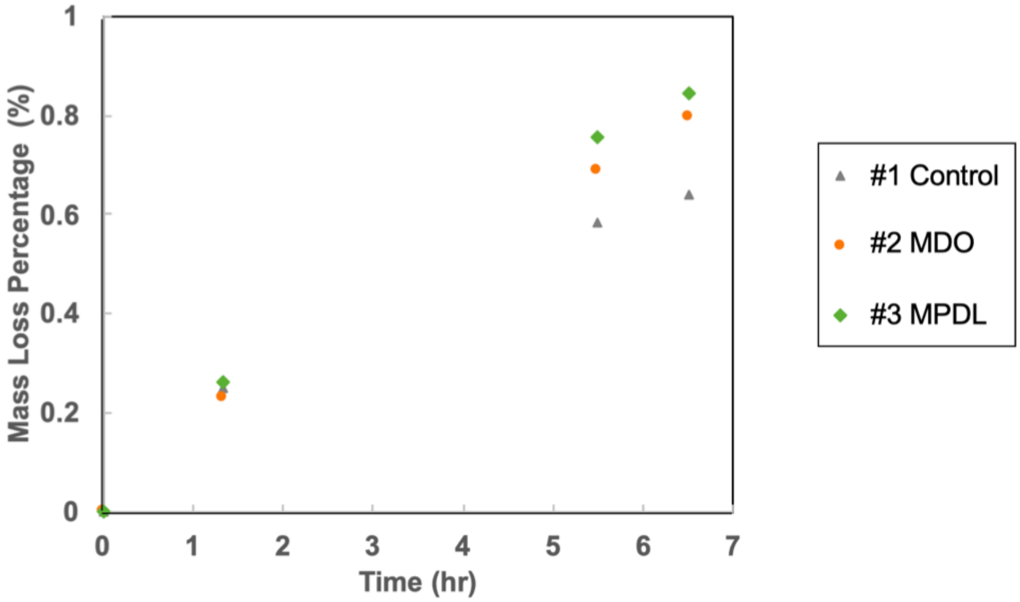

Figure 4.18: Plot of mass loss vs. time during hydrolytic degradation. Time represents the duration in which the samples are submerged in 1N NaOH solution. Compositions of the precursor mixture for the three samples are shown in Table 4.1.

For accurate control of the experimental process for characterization, all the samples have been fabricated after a short period of nitrogen purge and the solution mixture has been kept in an nitrogen environment during photopolymerization. However, the presence of oxygen is not expected to affect the polymerization dramatically as demonstrated in a previous work where minimal effect of oxygen has been observed on rROP of MA and cyclic allylic sulfide.[118] Although 3D printers can be easily modified to print under inert environment, it would be beneficial to reassess the reactions in a regular ambient environment (with the presence of oxygen) for future studies.

Chapter 5

OUTLOOK

5.1 Potentials of Dynamically Cross-linked Materials for AM

The reversible dynamic nature of electrostatic interactions between the metal ions and polyelectrolye (PAA) allows MPECs to change configuration and reform bonds that were once broken. The strength of the coordination bonding is determined by the affinity of the metal ion to the polymer binding site, which can be tuned based on the selection of the metal ion type and the chemical environment of the binding site. The bond breakage allows energy dissipation of the polymer network. Grindy et al. reported a model study with two types of metal-ligand crosslinks, relatively slow versus fast (Figure 5.1). By varying the relative concentration of the two types of metal-ligand interactions, the mechanical hierarchy of energy-dissipating modes under dynamic mechanical loading can be controlled. This approach offers an opportunity to engineer the viscoelastic properties of the materials by controlling the types of metal ion crosslinks without modifying the polymer itself.[119] For example, with 75% Ni^{+2} to 25% Zn^{+2}, the two local maxima in shear loss modulus (G") have been detected which are indicative of two distinct relaxation mode distributions; the modulus as a function of frequency is then fitted to the relaxation spectra to give rise to the two distinct peaks, shown at the bottom left plot of Figure 5.1. This work inspires to further the 3DP MPEC study by optimizing the material composition for efficient energy dissipation.

From the 3DP MPEC study reported in Chapter 2, we learned that initial metal ion content and metal ion species in the photoresin can affect the molecular weight of the PAA. To control the polymer network and only study the effect of metal-polyeletrolyte interaction for energy dissipation, it would be ideal to start with a low concentration of the metal ion to form the starting network. For instance, the low-Al system could offer a sufficient starting network and different metal ion species can be subsequently swelled into the network. Since the photoresin is optimized for VP processes, in addition to studying the energy dissipation of the dynamic interaction on the molecular level, the energy dissipation on the 3D architecture-level can also be investigated.

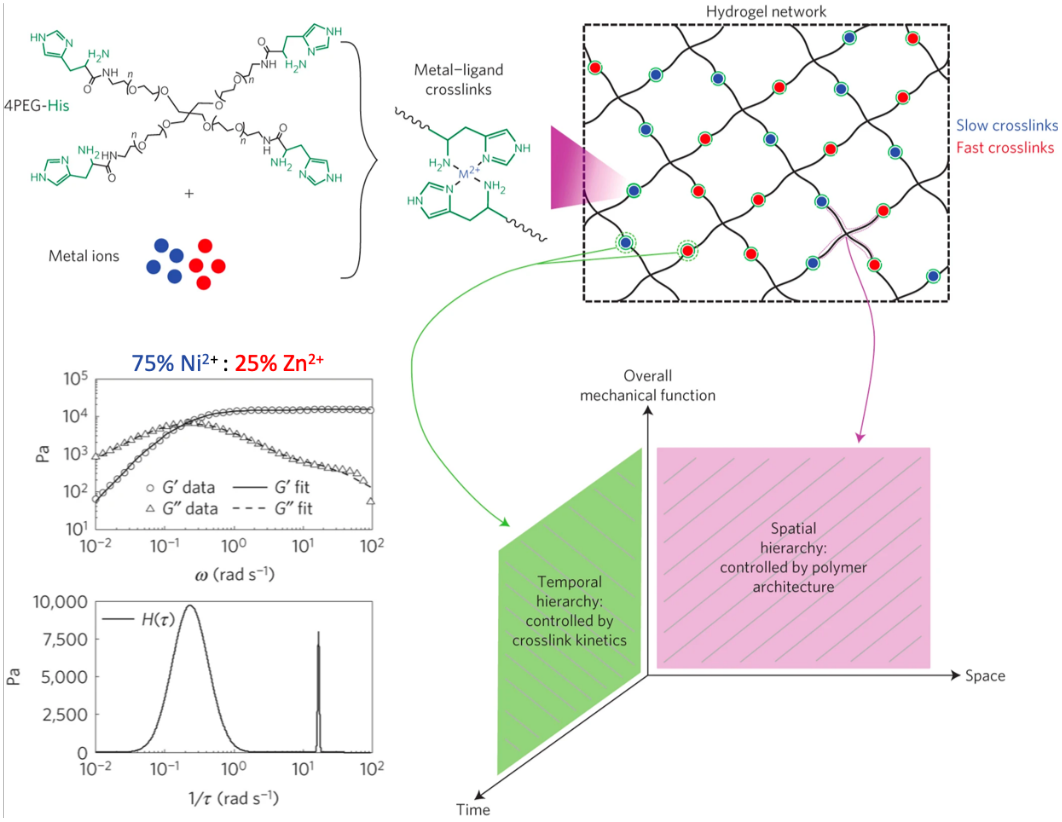

Figure 5.1: Model materials systems with orthogonally tunable mechanical temporal hierarchy.[119] Figure reprinted with permission from the copyright holder, Nature Publishing Group.

5.2 Capability of AM-enabled Thermoresponsive IPNs Beyond Water Release

5.2.1 VP-enable Thermoresponsive IPNs for Cartilage Tissue Engineering

As discussed in Chapter 3, the formation of IPNs is a great way to overcome the mechanical weakness of PNIPAM while preserving its thermoresponsiveness. Because of its biocompatibility and the near biological–temperature LCST, PNIPAM-containing INPs have great potentials in biomedical applications, where PNIPAM and its IPNs have been considered for cell-sheet growth, injectable 3D cell scaffolds, and controlled drug release/absorption.[50, 57, 58] However, to overcome the cytotoxicity and poor biodegradability of neat PNIPAM, copolymerization of NIPAM have been explored to enable an extrusion-based 3D printing technique for tissue engineering.[57, 120]

One specific field in which 3D architected PNIPAM-containing IPNs can be applied is in cartilage tissue engineering. For such applications, it is desirable to print tough, macroporous hydrogels that promote sell differentiation and proliferation into chondrocytes and are adhesive, non-degrading, and stable against dissolution in water. [51, 121] Cartilages are hydrogels with approximately 80 wt% water with the remaining mass comprised of extracellular matrix and chondrocytes to provide the structure, with compressive strength and elastic modulus of 14-59 MPa and 0.31 MPa, respectively.[121, 122] The mean storage and loss modulus of human cartilage is ranging from 31.9 MPa to 43.3 MPa and from 5.3 MPa to 8.5 MPa, respectively, over the frequency range of 1 Hz to 88 Hz.[123]

Based on what we have learned about the fabrication of the thermoresponsive IPNs, we can further optimize the architected IPNs to reach the desired mechanical property. By accessing tough, 3D–printable and thermoresponsive IPNs, personalized cartilage implants can be realized using this VP-enabled process. The material can be soft during the implant procedure at room temperature to alleviate the impact at the implant site, and then it thermoresponsively stabilizes into its final state once entering the body.

Most studies of PNIPAM-containing IPNs only focus on analyzing the thermodynamic or volumetric change properties, with some investigations on the environmental effects, such as pH and ionic strength.[59, 61, 63, 64, 74] Mechanical analysis of the temperature dependency for a simultaneously homogeneous and tough system has not been thoroughly explored via dynamic mechanical analysis (DMA).[78, 79] An investigation on the effect of temperature on dynamic mechanical behavior has since been studied by other lab members of the group.

5.2.2 Fabrication of Porous IPNs and Dynamic Mechanical Analysis

For biomedical applications, volumetric shrinkage can be a disadvantage, especially when it responds to a change in temperature. Based on our material exploration reported in Chapter 3, several formulations give rise to IPNs with relatively small volumetric changes (20% - 30%) but consistent LCSTs, such as, the PAM/PNIPAM and P(AM-co-AM)/PNIPAM IPNs with 2.5M and 3.5M first network monomer concentrations. With this observation, we fabricated cylindrical samples for DMA study with periodic pores design within the structures. By varying the pore sizes and periodicity, we fabricated the three sets of porous IPNs shown in Figure 5.2. The first network gels experience a significant volumetric retraction after the 2nd network formation, which suggests structural reinforcement. The DMA analysis of these samples is still under investigation.

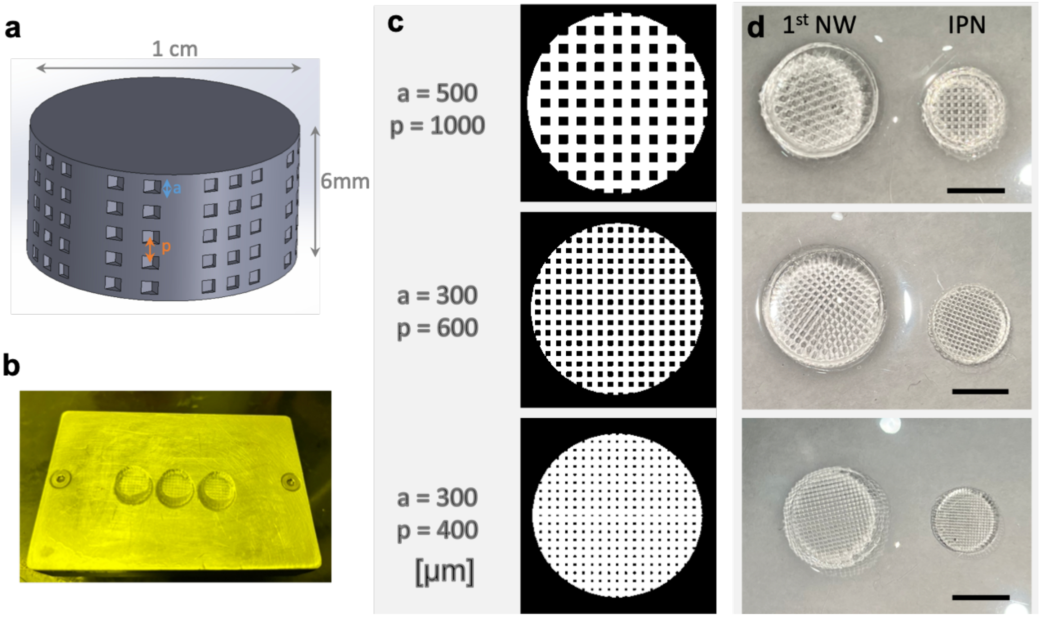

Figure 5.2: Fabrication of IPNs with designed pores. a) Representative CAD file for porous gels with *a* being the edge length of the cubic pores and *p* being the periodicity of the pores. b) Image of as-printed 1st network gel. c) Three sets of parameters used for different *a* and *p* values and the representative 2D pattern for PμSL. d) Optical images of the obtained 1st network gel and their corresponding IPNs.

5.3 Designing Degradable Materials for AM with Gas and Moisture Inhibition Capability

Besides enabling 3D printing technologies, photopolymer resins also demonstrate many other advantageous qualities, such as good solution processability, scalability for large scale processing and light-enabled simple curing process. Liquid photoresins also allow the addition of other functional components with compatible solubility. CKAs have shown promising results as an additive to increase the degradability of the acrylate-based photoresin. In addition to introducing CKAs, other functional chemical groups can also be incorporated to give the photopolymer advanced functionalities. One particular direction of interest is to create low oxygen and moisure permeability materials that are also degradable for either 3D–printed parts, packaging materials, or coating for surfaces. [124]

BIBLIOGRAPHY

[1] Pankaj Kumar et al. “3D Printing technology for biomedical practice: A review.” In: *Journal of Materials Engineering and Performance* 30.7 (2021), pp. 5342–5355.

[2] Peng Wu, Jun Wang, and Xiangyu Wang. “A critical review of the use of 3-D printing in the construction industry.” In: *Automation in Construction* 68 (2016), pp. 21–31.

[3] Iman Dankar et al. “3D printing technology: The new era for food customization and elaboration.” In: *Trends in Food Science & Technology* 75 (2018), pp. 231–242.

[4] Lawrence E. Murr. “A metallographic review of 3D printing/additive manufacturing of metal and alloy products and components.” In: *Metallography, Microstructure, and Analysis* 7.2 (2018), pp. 103–132.

[5] Samuel Clark Ligon et al. “Polymers for 3D printing and customized additive manufacturing.” In: *Chemical Reviews* 117.15 (2017), pp. 10212–10290.

[6] Anand Kumar and R.V.S. Prasad. “Basic principles of additive manufacturing: different additive manufacturing technologies.” In: *Additive Manufacturing*. Elsevier, 2021, pp. 17–35.

[7] Feng Zhang et al. “The recent development of vat photopolymerization: A review.” In: *Additive Manufacturing* 48 (2021), p. 102423.

[8] Ali Davoudinejad et al. “Additive manufacturing with vat polymerization method for precision polymer micro components production.” In: *Procedia CIRP* 75 (2018), pp. 98–102.

[9] William E. Frazier. “Metal additive manufacturing: A review.” In: *Journal of Materials Engineering and Performance* 23.6 (2014), pp. 1917–1928.

[10] Daryl W. Yee and Julia R. Greer. “Three-dimensional chemical reactors: in situ materials synthesis to advance vat photopolymerization.” In: *Polymer International* 70.7 (2021), pp. 964–976.

[11] Qi Ge et al. “Projection micro stereolithography based 3D printing and its applications.” In: *International Journal of Extreme Manufacturing* 2.2 (2020), p. 022004.

[12] Michael Layani, Xiaofeng Wang, and Shlomo Magdassi. “Novel materials for 3D printing by photopolymerization.” In: *Advanced Materials* 30.41 (2018), p. 1706344.

[13] C. Sun et al. “Projection micro-stereolithography using digital micro-mirror dynamic mask.” In: *Sensors and Actuators A: Physical* 121.1 (2005), pp. 113–120.

[14] Xiaoyu Zheng et al. “Ultralight, ultrastiff mechanical metamaterials.” In: *Science* 344.6190 (2014), pp. 1373–1377.

[15] John R. Tumbleston et al. “Continuous liquid interface production of 3D objects.” In: *Science* 347.6228 (2015), pp. 1349–1352.

[16] Haoyuan Quan et al. “Photo-curing 3D printing technique and its challenges.” In: *Bioactive Materials* 5.1 (2020), pp. 110–115.

[17] Mohamed GA Mohamed et al. “Rapid and inexpensive fabrication of multi-depth microfluidic device using high-resolution LCD stereolithographic 3D printing.” In: *Journal of Manufacturing and Materials Processing* 3.1 (2019), p. 26.

[18] Parvathi Nair S. et al. “3D printing mesoscale optical components with a low-cost resin printer integrated with a fiber-optic taper.” In: *ACS Photonics* (2022).

[19] Formlabs. *Materials Data Sheet of Photopolymer Resin for Form 1+ and Form 2*. `https://archive-media.formlabs.com/upload/XL-DataSheet.pdf`. 2019.

[20] Stratasys. *Materials Data Sheet for Flexible Tango*. `https://www.stratasys.com/en/materials/materials-catalog/polyjet-materials/tango`. 2018.

[21] adlughmin. *Materials Data Sheet of Photopolymer Resin for Form 1+ and Form 2*. `https://3dprint.com/50225/autodesk-ember-pr48-resin/`. 2015.

[22] Dinesh K. Patel et al. “Highly stretchable and UV curable elastomers for digital light processing based 3D printing.” In: *Advanced Materials* 29.15 (2017), p. 1606000.

[23] Amylynn C. Chen, Widianto P. Moestopo, Zane W. Taylor, Seola Lee, Daryl W. Yee, and Julia R. Greer. “Vat polymerization of compliant and tough metal-coordinated polymers with tunable mechanical properties (*In preparation*).” 2022.

[24] Tianyu Zhu et al. “Metallo-polyelectrolytes as a class of ionic macromolecules for functional materials.” In: *Nature Communications* 9.1 (2018), pp. 1–15.

[25] Liyang Shi et al. “Self-healing polymeric hydrogel formed by metal–ligand coordination assembly: design, fabrication, and biomedical applications.” In: *Macromolecular Rapid Communications* 40.7 (2019), p. 1800837.

[26] Eesha Khare, Niels Holten-Andersen, and Markus J. Buehler. “Transition-metal coordinate bonds for bioinspired macromolecules with tunable mechanical properties.” In: *Nature Reviews Materials* 6.5 (2021), pp. 421–436.

[27] Lisa M. Fuhrer et al. “Tuning the properties of hydrogels made from poly (acrylic acid) and calcium salts.” In: *Physical Chemistry Chemical Physics* 22.33 (2020), pp. 18631–18638.

[28] David J. Schupp et al. “Mineral plastic hydrogels from the cross-linking of polyacrylic acid and alkaline earth or transition metal ions.” In: *Chemical Communications* 55.34 (2019), pp. 4913–4916.

[29] Tadeusz Spychaj and Beata Schmidt. “Polymeric systems based on poly (acrylic acid) and trivalent metal cations.” In: *Macromolecular Symposia*. Vol. 152. 1. WILEY-VCH Verlag Weinheim. 2000, pp. 173–189.

[30] Longxiang Zhu, Jianhui Qiu, and Eiichi Sakai. “A high modulus hydrogel obtained from hydrogen bond reconstruction and its application in vibration damper.” In: *RSC Advances* 7.69 (2017), pp. 43755–43763.

[31] Xuefeng Li et al. “Dual ionically cross-linked double-network hydrogels with high strength, toughness, swelling resistance, and improved 3D printing processability.” In: *ACS Applied Materials & Interfaces* 10.37 (2018), pp. 31198–31207.

[32] Can Hui Yang et al. “Strengthening alginate/polyacrylamide hydrogels using various multivalent cations.” In: *ACS Applied Materials & Interfaces* 5.21 (2013), pp. 10418–10422.

[33] Dmitry V. Pergushov et al. “Advanced functional structures based on interpolyelectrolyte complexes.” In: *Polyelectrolyte Complexes in the Dispersed and Solid State I*. Springer, 2013, pp. 173–225.

[34] Huan Zhang et al. “Self-healing of bulk polyelectrolyte complex material as a function of pH and salt.” In: *ACS Applied Materials & Interfaces* 8.39 (2016), pp. 26258–26265.

[35] Jana Herzberger et al. “Polymer design for 3D printing elastomers: Recent advances in structure, properties, and printing.” In: *Progress in Polymer Science* 97 (2019), p. 101144.

[36] Sadiya Anjum et al. “Design and development of trivalent aluminum ions induced self-healing polyacrylic acid novel hydrogels.” In: *Polymer* 126 (2017), pp. 196–205.

[37] Si Yu Zheng et al. “Metal-coordination complexes mediated physical hydrogels with high toughness, stick–slip tearing behavior, and good processability.” In: *Macromolecules* 49.24 (2016), pp. 9637–9646.

[38] Ewelina Basiak, Andrzej Lenart, and Frederic Debeaufort. “How glycerol and water contents affect the structural and functional properties of starch-based edible films.” In: *Polymers* 10.4 (2018), p. 412.

[39] Tatauko Hatakeyama, Kunio Nakamura, and Hyoe Hatakeyama. “Determination of bound water content in polymers by DTA, DSC and TG.” In: *Thermochimica Acta* 123 (1988), pp. 153–161.

[40] German Ayala, Ana Agudelo, and Ruben Vargas. “Effect of glycerol on the electrical properties and phase behavior of cassava starch biopolymers.” In: *Dyna* 79.171 (2012), pp. 138–147.

[41] Tianyu Zhu and Chuanbing Tang. “Crosslinked Metallo-Polyelectrolytes with Enhanced Flexibility and Dimensional Stability for Anion-Exchange Membranes”. In: *Polymer Chemistry* 11 (2020), pp. 4542–4546.

[42] I. Quijada-Garrido et al. “The role played by the interactions of small molecules with chitosan and their transition temperatures. Glass-forming liquids: 1, 2, 3-Propantriol (glycerol).” In: *Carbohydrate Polymers* 68.1 (2007), pp. 173–186.

[43] Dimitri Wilms et al. “Elastic modulus distribution in poly(N-isopopylacrylamide) and oligo(ethylene glycol methacrylate)-based microgels studied by AFM.” In: *Soft Mat.* 17 (2021), pp. 5711–5717.

[44] Pak Man Yiu et al. “Strain rate and thickness dependences of elastic modulus of free-standing polymer nanometer films.” In: *ACS Macro Letters* 9.11 (2020), pp. 1521–1526.

[45] Guorong Gao et al. “Self-healable, tough, and ultrastretchable nanocomposite hydrogels based on reversible polyacrylamide/montmorillonite adsorption.” In: *ACS Applied Materials & Interfaces* 7.8 (2015), pp. 5029–5037.

[46] Nan Nan Xia et al. “A seawater triggered dynamic coordinate bond and its application for underwater self-healing and reclaiming of lipophilic polymer.” In: *Chemical Science* 7.4 (2016), pp. 2736–2742.

[47] Rajendra P Chhabra. “Non-Newtonian fluids: An introduction.” In: *Rheology of Complex Fluids*. Springer, 2010, pp. 3–34.

[48] Jeannine E. Elliott et al. “Structure and swelling of poly (acrylic acid) hydrogels: effect of pH, ionic strength, and dilution on the crosslinked polymer structure.” In: *Polymer* 45.5 (2004), pp. 1503–1510.

[49] Vincenzo Costanza et al. “Effect of glycerol on the mechanical and temperature-sensing properties of pectin films”. In: *Applied Physics Letters* 115 (2019), p. 193702.

[50] Mark A. Ward and Theoni K. Georgiou. “Thermoresponsive polymers for biomedical applications.” In: *Polymers* 3.3 (2011), pp. 1215–1242.

[51] Md Mohosin Rana and Hector De la Hoz Siegler. “Tuning the properties of PNIPAm-based hydrogel scaffolds for cartilage tissue engineering.” In: *Polymers* 13.18 (2021), p. 3154.

[52] Jia Liu et al. “Recent progress in PNIPAM-based multi-responsive actuators: A mini-review.” In: *Chemical Engineering Journal* (2021), p. 133496.

[53] Amylynn C. Chen, Zane W. Taylor, Akash Dhawan, and Julia R. Greer. "Additive manufacturing enabled thermally responsive double network hydrogels (*In preparation*)." 2022.

[54] W.M. Huang et al. "Shape memory materials." In: *Materials Today* 13.7-8 (2010), pp. 54–61.

[55] Changdeng Liu, Haihu Qin, and P.T. Mather. "Review of progress in shape-memory polymers." In: *Journal of Materials Chemistry* 17.16 (2007), pp. 1543–1558.

[56] Byeongmoon Jeong, Sung Wan Kim, and You Han Bae. "Thermosensitive sol–gel reversible hydrogels." In: *Advanced Drug Delivery Reviews* 64 (2012), pp. 154–162.

[57] Falko Doberenz et al. "Thermoresponsive polymers and their biomedical application in tissue engineering: A review." In: *Journal of Materials Chemistry B* 8.4 (2020), pp. 607–628.

[58] Jinhua Li et al. "3D printing of hydrogels: Rational design strategies and emerging biomedical applications." In: *Materials Science and Engineering: R: Reports* 140 (2020), p. 100543.

[59] Jan Seuring and Seema Agarwal. *Polymers with upper critical solution temperature in aqueous solution: Unexpected properties from known building blocks.* 2013.

[60] IC Sanchez and MT Stone. "Statistical thermodynamics of polymer solutions and blends." In: *Polymer Blends* 1 (2000), pp. 15–53.

[61] Erno Karjalainen, Vladimir Aseyev, and Heikki Tenhu. "Upper or lower critical solution temperature, or both? Studies on cationic copolymers of N-isopropylacrylamide." In: *Polymer Chemistry* 6.16 (2015), pp. 3074–3082.

[62] Anton A. Smith et al. "Controlling properties of thermogels by tuning critical solution behaviour of ternary copolymers." In: *Polymer Chemistry* 12.13 (2021), pp. 1918–1923.

[63] Marek Radecki et al. "Temperature-induced phase transition in hydrogels of interpenetrating networks of poly (N-isopropylacrylamide) and polyacrylamide." In: *European Polymer Journal* 68 (2015), pp. 68–79.

[64] E. Diez-Pena et al. "Thermal properties of cross-linked poly (N-isopropylacrylamide)[P (N-iPAAm)], poly (methacrylic acid)[P (MAA)], their random copolymers [P (N-iPAAm-co-MAA)], and sequential interpenetrating polymer networks (IPNs)." In: *Macromolecules* 35.7 (2002), pp. 2667–2675.

[65] Gloria G Chan, Clarissa M Koch, and Lawreen H Connors. "Blood proteomic profiling in inherited (ATTRm) and acquired (ATTRwt) forms of transthyretin-associated cardiac amyloidosis." In: *Journal of Proteome Research* 16.4 (2017), pp. 1659–1668.

[66] Xiaobing Liu et al. “Effect of Ca2+ ion and temperature on association of thermally sensitive PAA-b-PNIPAM diblock chains in aqueous solutions.” In: *Macromolecules* 45.11 (2012), pp. 4830–4838.

[67] Jae-Hyung Park et al. “Preparation and properties of thermoresponsive P (N-Isopropylacrylamide-co-butylacrylate) hydrogel materials for smart windows.” In: *International Journal of Polymer Science* 2019 (2019).

[68] Muhammad Abdul Haq, Yunlan Su, and Dujin Wang. “Mechanical properties of PNIPAM based hydrogels: A review.” In: *Materials Science and Engineering: C* 70 (2017), pp. 842–855.

[69] Xingyi Zhou et al. “Atmospheric water harvesting: A review of material and structural designs.” In: *ACS Materials Letters* 2.7 (2020), pp. 671–684.

[70] Syang-Peng Rwei et al. “Synthesis and characterization of pH and thermo dual-responsive hydrogels with a semi-IPN structure based on N-isopropylacrylamide and itaconamic acid.” In: *Materials* 11.5 (2018), p. 696.

[71] Daniel J. Phillips and Gibson Matthew I. “Towards being genuinely smart: ‘isothermally-responsive’ polymers as versatile, programmable scaffolds for biologically-adaptable materials.” In: *Polymer Chemistry* 6 (2015), pp. 1033–1043.

[72] Zheyu Shen et al. “Synthesis and phase behavior of aqueous poly (N-isopropylacrylamide-co-acrylamide), poly (N-isopropylacrylamide-co-N, N-dimethylacrylamide) and poly (N-isopropylacrylamide-co-2-hydroxyethyl methacrylate).” In: *Colloid and Polymer Science* 284.9 (2006), pp. 1001–1007.

[73] Seon Jeong Kim, Sang Jun Park, and Sun I Kim. “Synthesis and characteristics of interpenetrating polymer network hydrogels composed of poly (vinyl alcohol) and poly (N-isopropylacrylamide).” In: *Reactive and Functional Polymers* 55.1 (2003), pp. 61–67.

[74] Herman Feil et al. “Effect of comonomer hydrophilicity and ionization on the lower critical solution temperature of N-isopropylacrylamide copolymers.” In: *Macromolecules* 26.10 (1993), pp. 2496–2500.

[75] Stephen Don Sarkar et al. “Mechanically tough and highly stretchable poly (acrylic acid) hydrogel cross-linked by 2D graphene oxide.” In: *RSC Advances* 10.18 (2020), pp. 10949–10958.

[76] Xuefeng Li et al. “Dual physically crosslinked double network hydrogels with high toughness and self-healing properties.” In: *Soft Matter* 13.5 (2017), pp. 911–920.

[77] Hui Li et al. “Recent advances in metal-containing polymer hydrogels.” In: *Macromolecular Rapid Communications* 38.14 (2017), p. 1700109.

[78] Hui Guo et al. "Thermoresponsive toughening in LCST-type hydrogels: Comparison between semi-interpenetrated and grafted networks." In: *Macromolecules* 49.24 (2016), pp. 9568–9577.

[79] Ranee A. Stile and Kevin E. Healy. "Poly (n-isopropylacrylamide)-based semi-interpenetrating polymer networks for tissue engineering applications. 1. Effects of linear poly (acrylic acid) chains on phase behavior." In: *Biomacromolecules* 3.3 (2002), pp. 591–600.

[80] Xueyang Wang et al. "An interfacial solar heating assisted liquid sorbent atmospheric water generator." In: *Angewandte Chemie* 131.35 (2019), pp. 12182–12186.

[81] Alina LaPotin et al. "Adsorption-based atmospheric water harvesting: impact of material and component properties on system-level performance." In: *Accounts of Chemical Research* 52.6 (2019), pp. 1588–1597.

[82] Lisa J. Mauer and Lynne S. Taylor. "Water-solids interactions: deliquescence." In: *Annual Review of Food Science and Technology* 1 (2010), pp. 41–63.

[83] Seong-Min Kim et al. "Influence of PEDOT: PSS crystallinity and composition on electrochemical transistor performance and long-term stability." In: *Nature Communications* 9.1 (2018), pp. 1–9.

[84] Hyunho Kim et al. "Water harvesting from air with metal-organic frameworks powered by natural sunlight." In: *Science* 356.6336 (2017), pp. 430–434.

[85] Yanping Yuan et al. "Inorganic composite sorbents for water vapor sorption: A research progress." In: *Renewable and Sustainable Energy Reviews* 54 (2016), pp. 761–776.

[86] Byung Chunl Shin et al. "pH/temperature dependent phase transition of an interpenetrating polymer network: anomalous swelling behavior above lower critical solution temperature." In: *European Polymer Journal* 34.11 (1998), pp. 1675–1681.

[87] Dongyu Zhu et al. "Effect of adamantyl methacrylate on the thermal and mechanical properties of thermosensitive poly (N-isopropylacrylamide) hydrogels." In: *Journal of Applied Polymer Science* 124.1 (2012), pp. 155–163.

[88] Xiaofeng Yi et al. "Highly efficient removal of uranium (VI) from wastewater by polyacrylic acid hydrogels." In: *RSC Advances* 7.11 (2017), pp. 6278–6287.

[89] Naoya Sagawa and Toshiyuki Shikata. "Are all polar molecules hydrophilic? Hydration numbers of nitro compounds and nitriles in aqueous solution." In: *Physical Chemistry Chemical Physics* 16.26 (2014), pp. 13262–13270.

[90] Leslie Howard Sperling. *Interpenetrating polymer networks and related materials.* Springer Science & Business Media, 2012.

[91] Bruno C. Hancock et al. “The powder flow and compact mechanical properties of two recently developed matrix-forming polymers.” In: *Journal of Pharmacy and Pharmacology* 53.9 (2001), pp. 1193–1199.

[92] Natalia Tarasova et al. “The new approach to the preparation of polyacrylamide-based hydrogels: initiation of polymerization of acrylamide with 1, 3-dimethylimidazolium (phosphonooxy-) oligosulphanide under drying aqueous solutions.” In: *Polymers* 13.11 (2021), p. 1806.

[93] Chi-Ta Yang et al. “The bonding nature and adhesion of polyacrylic acid coating on Li-metal for Li dendrite prevention.” In: *ACS Applied Materials & Interfaces* 12.45 (2020), pp. 51007–51015.

[94] Temoor Ahmed et al. “Biodegradation of plastics: Current scenario and future prospects for environmental safety.” In: *Environmental Science and Pollution Research* 25.8 (2018), pp. 7287–7298.

[95] AliReza Rahimi and Jeannette M. Garcıa. “Chemical recycling of waste plastics for new materials production.” In: *Nature Reviews Chemistry* 1.6 (2017), pp. 1–11.

[96] Industry Agenda. “The New Plastics Economy: Rethinking the future of plastics.” In: *World Economic Forum*. 2016, p. 36.

[97] Jasim Ahmed and Sunil K. Varshney. “Polylactides—chemistry, properties and green packaging technology: A review.” In: *International Journal of Food Properties* 14.1 (2011), pp. 37–58.

[98] Daoyang Fan et al. “Progressive 3D printing technology and its application in medical materials.” In: *Frontiers in Pharmacology* 11 (2020), p. 122.

[99] Mohammad Reza Khosravani and Tamara Reinicke. “On the environmental impacts of 3D printing technology.” In: *Applied Materials Today* 20 (2020), p. 100689.

[100] Laura O. Duncan et al. “Changes in mandibular incisor position and arch form resulting from Invisalign correction of the crowded dentition treated nonextraction.” In: *The Angle Orthodontist* 86.4 (2016), pp. 577–583.

[101] Hao Sun et al. “Degradable polymers via olefin metathesis polymerization.” In: *Progress in Polymer Science* 120 (2021), p. 101427.

[102] Junyang Shan et al. “Design and synthesis of free-radical/cationic photosensitive resin applied for 3D printer with liquid crystal display (LCD) irradiation.” In: *Polymers* 12.6 (2020), p. 1346.

[103] Theo Pesenti and Julien Nicolas. “100th anniversary of macromolecular science viewpoint: Degradable polymers from radical ring-opening polymerization: Latest advances, new directions, and ongoing challenges.” In: *ACS Macro Letters* 9.12 (2020), pp. 1812–1835.

[104] Antoine Tardy et al. “Radical ring-opening polymerization: Scope, limitations, and application to (bio) degradable materials.” In: *Chemical Reviews* 117.3 (2017), pp. 1319–1406.

[105] George Odian. *Principles of polymerization*. John Wiley & Sons, 2004.

[106] Antoine Tardy et al. “Radical copolymerization of vinyl ethers and cyclic ketene acetals as a versatile platform to design functional polyesters.” In: *Angewandte Chemie* 129.52 (2017), pp. 16742–16747.

[107] Elise Guégain et al. “Tunable degradation of copolymers prepared by nitroxide-mediated radical ring-opening polymerization and point-by-point comparison with traditional polyesters.” In: *Macromolecules* 51.3 (2018), pp. 724–736.

[108] Johanna Tran et al. “Efficient synthesis of 2-methylene-4-phenyl-1, 3-dioxolane, a cyclic ketene acetal for controlling the NMP of methyl methacrylate and conferring tunable degradability.” In: *Polymer Chemistry* 7.26 (2016), pp. 4427–4435.

[109] G. Evan Roberts et al. “Radical ring-opening copolymerization of 2-methylene 1, 3-dioxepane and methyl methacrylate: experiments originally designed to probe the origin of the penultimate unit effect.” In: *Macromolecules* 32.5 (1999), pp. 1332–1340.

[110] Mark Van Den Brink et al. “Nonlinear regression by visualization of the sum of residual space applied to the integrated copolymerization equation with errors in all variables. II. Application to the system methyl methacrylate-α-methylene-γ-butyrolactone using on-line Raman spectroscopy.” In: *Journal of Polymer Science Part A: Polymer Chemistry* 37.20 (1999), pp. 3804–3816.

[111] Brian J. Green and C. Allan Guymon. “Modification of mechanical properties and resolution of printed stereolithographic objects through RAFT agent incorporation.” In: *Additive Manufacturing* 27 (2019), pp. 20–31.

[112] Jeremy J. Weigand et al. “3D printing of dual-cure benzoxazine networks.” In: *Polymer* 189 (2020), p. 122193.

[113] Hubert Gojzewski et al. “Layer-by-layer printing of photopolymers in 3D: How weak is the interface?” In: *ACS Applied Materials & Interfaces* 12.7 (2020), pp. 8908–8914.

[114] Vianney Delplace et al. “A ring to rule them all: a cyclic ketene acetal comonomer controls the nitroxide-mediated polymerization of methacrylates and confers tunable degradability.” In: *Chemical Communications* 51.64 (2015), pp. 12847–12850.

[115] Antoine Tardy et al. “Radical copolymerization of vinyl ethers and cyclic ketene acetals as a versatile platform to design functional polyesters.” In: *Angewandte Chemie* 129.52 (2017), pp. 16742–16747.

[116] Antonina Simakova, Caroline Arnoux, and Krzysztof Matyjaszewski. “Degradable copolymers with incorporated ester groups by radical ring-opening polymerization using atom transfer radical polymerization.” In: *Polimery* 62.4 (2017), p. 262.

[117] Amanda L. Jenkins, Richard A. Larsen, and Timothy B. Williams. “Characterization of amino acids using Raman spectroscopy.” In: *Spectrochimica Acta Part A: Molecular and Biomolecular Spectroscopy* 61.7 (2005), pp. 1585–1594.

[118] Satoru Yamada and Yasutomo Goto. “Reduction of oxygen inhibition in photopolymerization of cyclic allylic sulfide monomer.” In: *Journal of Photopolymer Science and Technology* 23.1 (2010), pp. 109–114.

[119] Scott C. Grindy et al. “Control of hierarchical polymer mechanics with bioinspired metal-coordination dynamics.” In: *Nature Materials* 14.12 (2015), pp. 1210–1216.

[120] Katie J. Hogan and Antonios G. Mikos. “Biodegradable thermoresponsive polymers: Applications in drug delivery and tissue engineering.” In: *Polymer* 211 (2020), p. 123063.

[121] Feichen Yang, Vaibhav Tadepalli, and Benjamin J. Wiley. “3D printing of a double network hydrogel with a compression strength and elastic modulus greater than those of cartilage.” In: *ACS Biomaterials Science & Engineering* 3.5 (2017), pp. 863–869.

[122] Alice J. Sophia Fox, Asheesh Bedi, and Scott A. Rodeo. “The basic science of articular cartilage: structure, composition, and function.” In: *Sports Health* 1.6 (2009), pp. 461–468.

[123] Duncan K. Temple et al. “Viscoelastic properties of human and bovine articular cartilage: a comparison of frequency-dependent trends.” In: *BMC Musculoskeletal Disorders* 17.1 (2016), pp. 1–8.

[124] Carmelo Corsaro et al. “Acrylate and methacrylate polymers’ applications: Second life with inexpensive and sustainable recycling approaches”. In: *Materials* 15.1 (2021), p. 282.

Appendix A

ISOTHERMAL TITRATION CALORIMETRY FOR DETERMINING METAL ION BINDING AFFINITY TO POLY(ACRYLIC ACID)

Isothermal titration calorimetry (ITC) provides quantitative thermodynamic information of binding and dissociation reactions in solution. An ITC instrument consists of two cells; the compounds to be studied are placed in the sample cell, whereas the other cell is used as a control and contains the buffer in which the sample is dissolved (Figure A.1a). The titration process is illustrated in Figure A.1b. As the first injecting is made, all injected ligand is bound to the sample. The ITC system detects the heat change showing a sharp peak as seen in Figure A.2. The signal returns to baseline before the next inject and the next injection is made. As the injections continues, the sample becomes saturated with ligand, so less binding events would occur and the heat changes start to decrease. The experiment is completed when only the heat of dilution can be detected. After integrating each heat change peaks, the relationship of molar enthalpy and the molar ratio can be plotted (Figure A.2). Thermogram appears to be sigmoidal and the slope at the inflection point of the curve is the association constant, K_a. The enthalpy change (Δ) is determined as the height of the curve (Figure A.2). Gibbs free energy change (ΔG) and entropy changes (ΔS) can be determined using the following relationship:

$$\Delta G = \Delta H - T\Delta S = -RTln(K_a) \tag{A.1}$$

where K_a is binding affinity, R is the gas constant, and T is the absolute temperature.

To determine the binding affinity of the Fe^{3+} ion and Al^{3+} ion to poly(acrylic acid) (PAA), the ITC titration is carried out in the following steps. A $Fe(NO_3)_3$ solution (12.2 mM) is titrated into a PAA solution (3.1 mM with respect to the repeat unit) in a 100 mM pH 5 acetate buffer. ITC experiment consists of 25 injections with each injection being approximately 2 μL of Fe^{3+} solution into 175 μL of the PAA solution at 25 °C. For control titrations, Fe^{3+} solution is titrated into a pH 5 buffer solution and a titration of the pH 5 buffer solution into the PAA solution is also conducted to account for any ΔH ascribed to dilution effects. The same experiment is conducted for a 12.2 mM $Al(NO_3)_3$ solution.

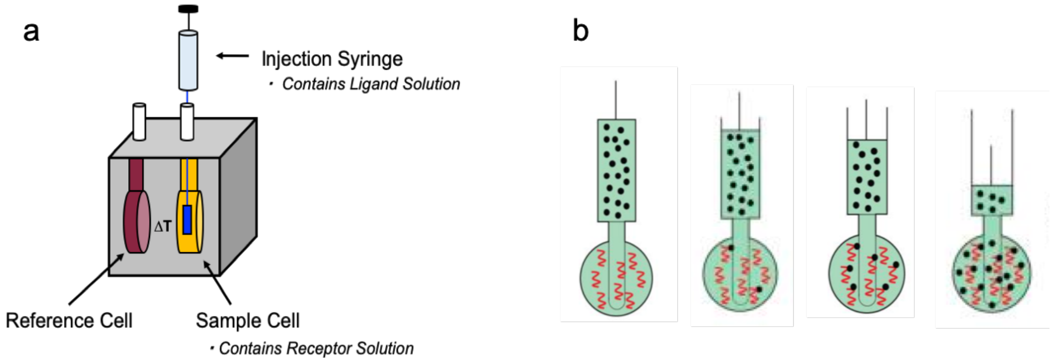

Figure A.1: Schedmetic of isothermal titration calorimetry's a) experimental set up and the b) binding process.

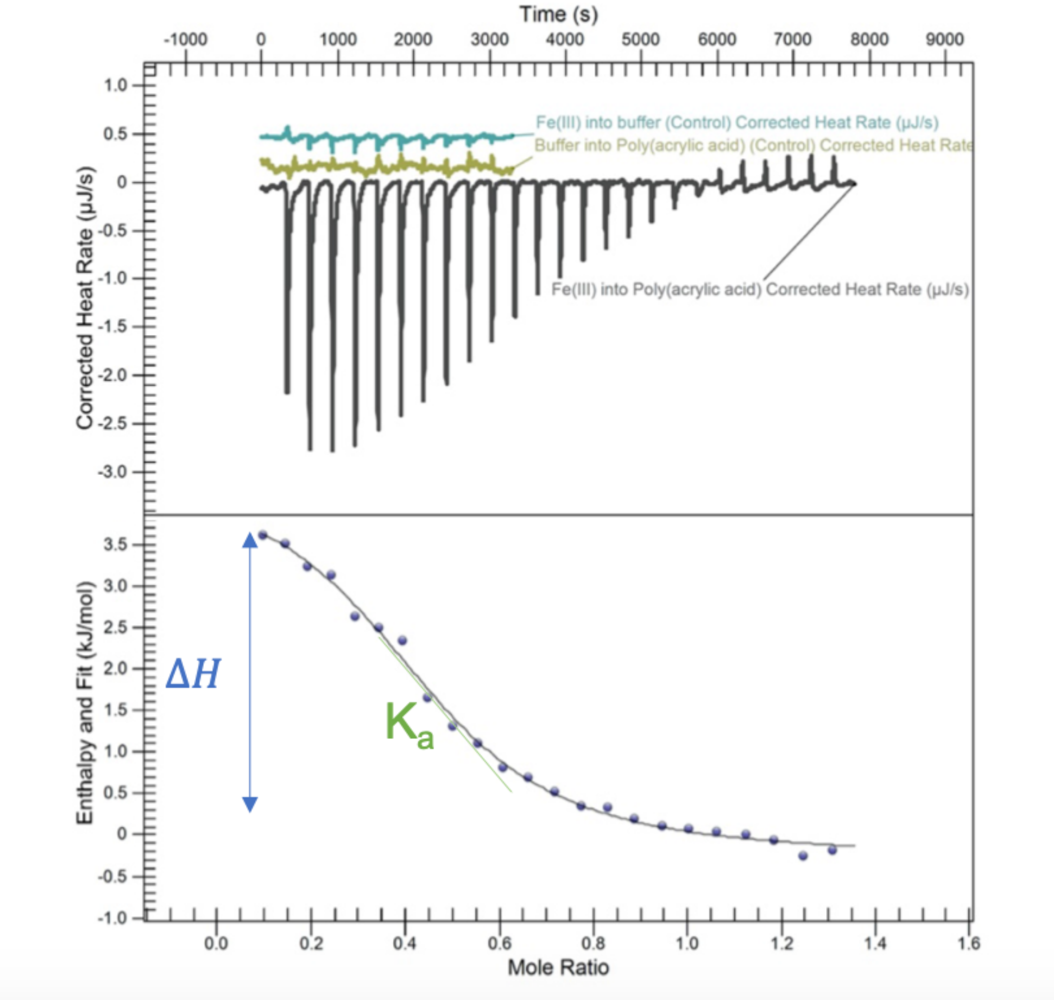

Figure A.2: ITC data for titration of Fe^{3+} binding to PAA solution at 25^o.

The ITC experiments reveal that the binding affinity of Al^{3+} to PAA is much greater that that of Fe^{3+}, with the K_a of Fe^{3+} to PAA being $5X10^3M^{-1}$ and the K_a of Al^{3+} to PAA being $3X10^8M^{-1}$. Given these differences, both Al^{3+} and Fe^{3+} ions were used for fabricating the MPEC samples to study the effect of metal ion binding affinity on the mechanical properties of the 3DP MPEC materials.

The ITC experiments were conducted by Ryan Archer in collaboration with Professor Michael Schulz's group.

Appendix B

FAILURE ANALYSIS OF 3DP MPECS

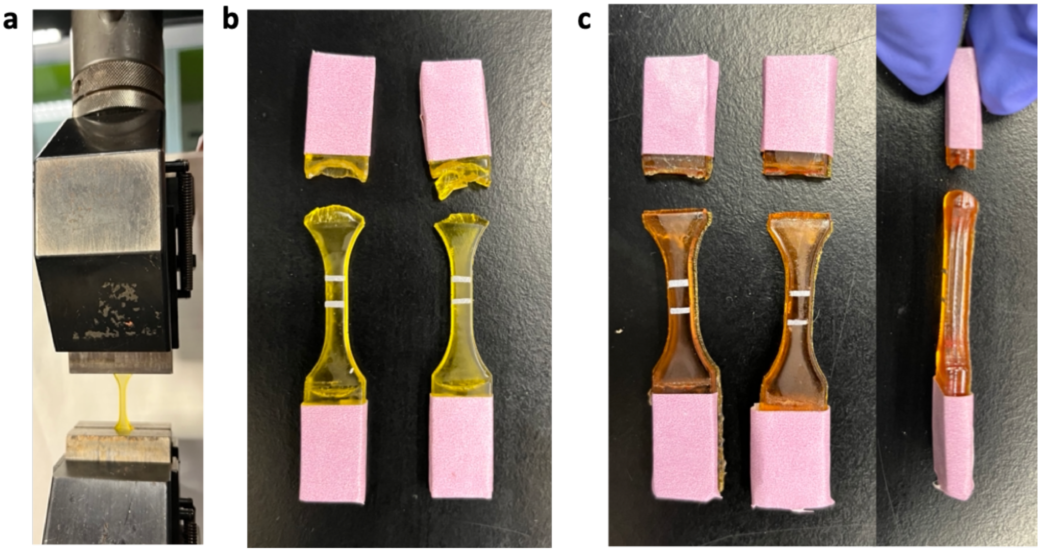

Figure B.1: Image of a) heavy duty grip used during tensile to failure testings and sample images of post tensile to failure testing of b) 5% glycerol MPEC-Al and c) 5% glycerol MPEC-Al.

During tensile to failure testing, we noticed that there is a significant amount of samples that failed at the edge of the grip. An image of the heavy duty grip can be found in Figure B.1a. This number is particularly high for tougher samples (the lower glycerol content samples). Out of the 10 MPEC samples with 5% glycerol reported in Figure 2.10, 7 have failed at the grip. Some images of these samples are shown in Figure B.1b and c. For the 10% glycerol, 5 out of 14 samples failed at the grip and only one sample had such failure for the 14 samples with 20% glycerol content. Although we have a limited sample number here, the trend is clear. When looking at the shape of failure surfaces, it resembles a cup and cone fracture. We suspect that the grip pins down the surface of the samples tightly resulting two shear planes to intersect. The stress that concentrates at the intersection of the two shear planes then propagates along the triangle portion of the sample causing it to ultimately reach the cup and cone failure. This suggests that over-cramping the grip onto the samples can cause defects and premature failures; thus, the ultimate tensile strength and failure strain values we have obtained can be even higher for the tougher samples. However, when we loosened the grip even just slightly, the samples ended up slipping from the grip(s) and made the data unusable. So the tightness we applied on the grips was necessary to conduct the measurements. This kind of failure is inevitable given the experimental setup and accessories we have. Pneumatic grips would be more appropriate for these samples since they can provide a constant and repeatable lateral force on the sample specimen by actuating the grip jaws with air. The rest of the samples all failed in the narrow region of the dogbone tensile samples with clear failure surfaces, as shown in Figure 2.9c.

Appendix C

CHEMICAL COMPOSITION OF DEVELOPED PHOTORESIN

C.1 Photoresin Composition for Metal Coordinated Polymers

A few example resin formulations for 3D printed MPECs are listed below:

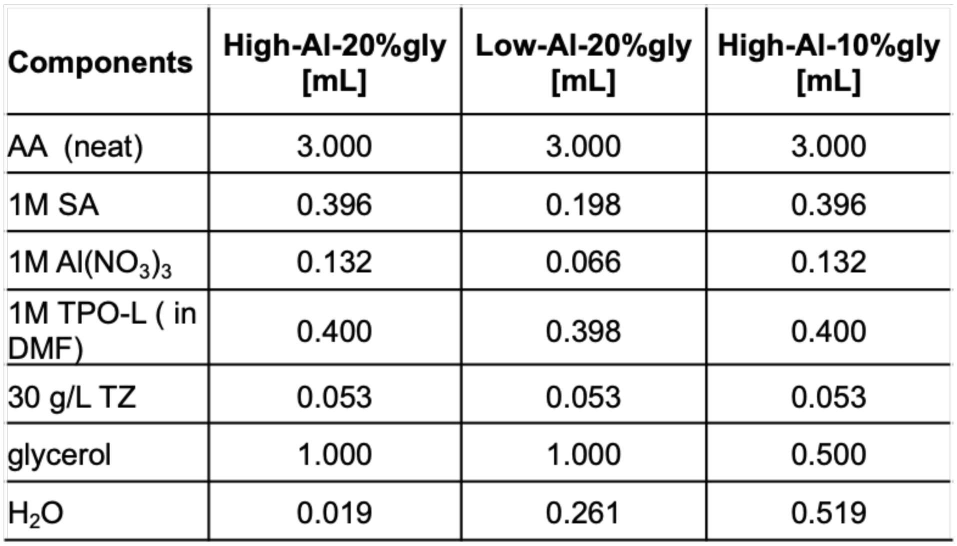

Components	**High-Al-20%gly [mL]**	**Low-Al-20%gly [mL]**	**High-Al-10%gly [mL]**
AA (neat)	3.000	3.000	3.000
1M SA	0.396	0.198	0.396
1M $Al(NO_3)_3$	0.132	0.066	0.132
1M TPO-L (in DMF)	0.400	0.398	0.400
30 g/L TZ	0.053	0.053	0.053
glycerol	1.000	1.000	0.500
H_2O	0.019	0.261	0.519

Table C.1: Photoresin formulations for 3DP MPECs.

Appendix D

ADDITIONAL MATERIAL SYSTEMS INVESTIGATED FOR THERMORESPONSIVE IPNS

Besides P(AM-co-AM)/PNIPAM, several other material systems have been investigated to search for better performing thermoresponsive IPNs. PAA/PNIPAM is the first system we have explored, because PAA have stronger interactions with deliquescent salts through metal-polymer coordination bonding. We considered it a good polymer candidate to combine with deliquescent salts as moisture absorbents for AWH. As we explored further to optimize the water release behavior, we discovered that several other first network polymers have better compatibility with PNIPAM than PAA for improved water release behavior, such as P(AM-co-AA), PAM, and P(AM-co-SA). The P(AM-co-AM)/PNIPAM have been discussed in details in Chapter 3. Some of the highlights of the other materials explored are summarized in the sections below.

D.1 Investigation of PAA/PNIPAM IPNs

As a comparison to the P(AM-co-AA)/PNIPAM IPNs, PAA/PNIPAM IPNs have also been fabricated with the same monomer concentration for 1st and 2nd network. All PAA/PNIPAM IPNs are significantly stiffer than the corresponding P(AM-co-AA)/PNIPAM IPNs, which is characterized by DMA. The water release performance of PAA/PNIPAM IPNs are dramatically worse than all the other material systems that we have explored. This is likly due to the high crosslinking density of the PAA gels. The crosslinking density of the 1.5M AM 1st network is close to that of the 2.5M AM 1st network gel, which could be the reason that only the DSC curves of Figure D.1a have LCST near 32^oC. When the 1st network AA concentration is increased to 3.5M, the LCST is shifted substantially to $48\text{-}49^oC$ (Figure D.1b). Figure D.1b shows some interesting peaks in the DSC curves that we have not observed in any other materials systems we have explored. No reporting of the exothermic peaks on PAA-PNIPAM IPNs has been found in literature.We suspect that some kind of water transfer mechanism occurred from PNIPAM to PAA near LCST. Water binding events can be energetically favorable which give rise to that exothermic peak.

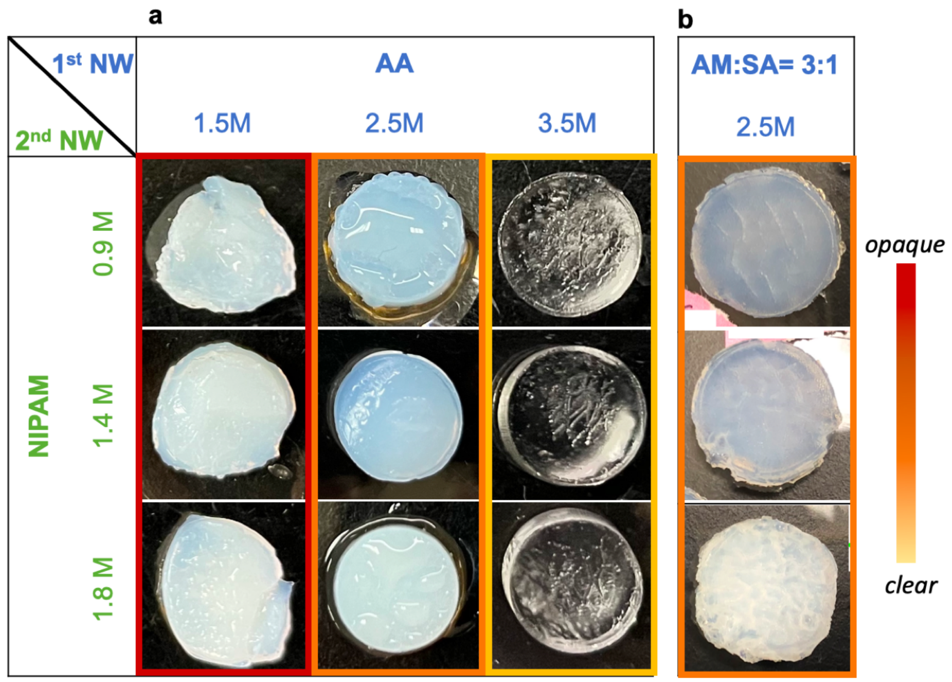

Table D.1: Sample formulations and optical images of a) PAA/PNIPAM and b) P(SA-co-AA)/PNIPAM IPNs for DSC.

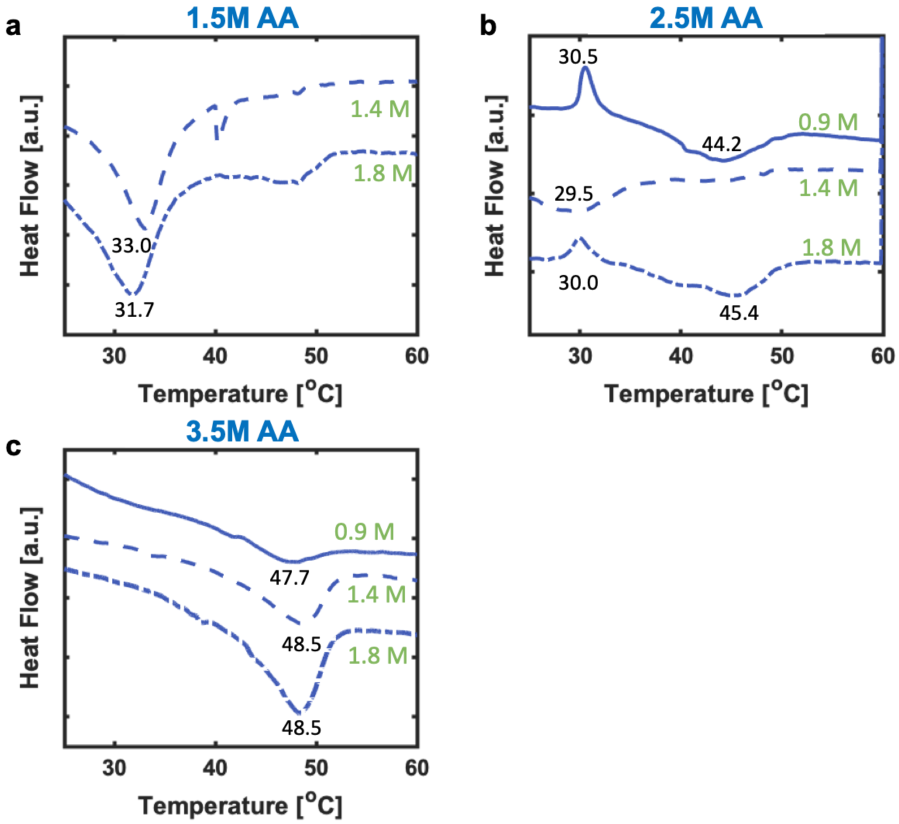

Figure D.1: Investigation of PAA/PNIPAM IPNs using a) DSC of PAA/PNIPAM IPNs with 1st network monomer (AA) concentration of 2.5 M and b) volumetric change measurements of IPNs.

D.2 Investigation of PAM/PNIPAM IPNs

PAM/PNIPAM IPNs have also been fabricated to compare with the P(AM-co-AA)/PNIPAM system. While keeping a 1st network monomer (AM) concentration of 2.5M, the samples have similar semi-opaqueness and LCST values as the P(AM-co-AA)/PNIPAM ones. In the PAM/PNIPAM set, the largest volumetric change, 46% ± 4%, occurs with the lowest 2nd network monomer (NIPAM) concentration, 0.9M; whereas, in the 2.5M P(AM-co-AA)/PNIPAM set, the largest volumetric change, 43% ± 1% occurs with 2nd network monomer (NIPAM) concentration of 1.4M.

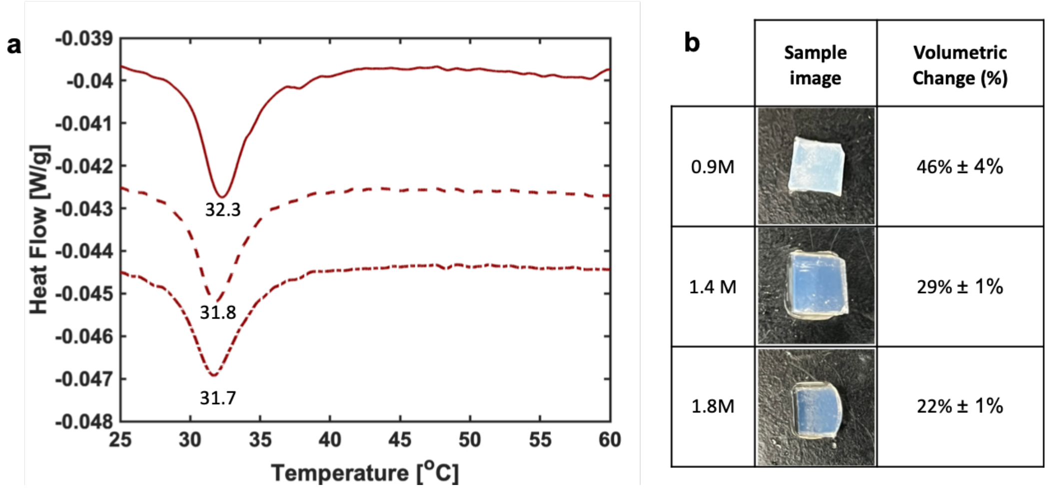

	Sample image	Volumetric Change (%)
0.9M		46% ± 4%
1.4 M		29% ± 1%
1.8M		22% ± 1%

Figure D.2: Investigation of PAM/PNIPAM IPNs using a) DSC of PAM/PNIPAM IPNs with 1st network monomer (AM) concentration of 2.5 M while varying the 2nd network (NIPAM) concentrations and b) mean volumetric change measurements of four IPN samples.

D.3 Investigation of P(AM-co-SA)/PNIPAM IPNs

The last IPN material systems we have looked at is P(AM-co-SA)/PNIPAM. By replacing the AA with SA (sodium acrylate) we hope to increase the hydrophilicity of the 1st network, thus to improve the swelling in the process for the 2nd network. However, P(AM-co-SA) are PNIPAM not compatible with each other at 2.5M 1st network concentration. Although the LCSTs appear consistently near 32 ^{o}C, the samples show clear phase separation upon UV exposure during the 2nd network fabrication, which can be seen in Figure D.3a. The highly hydrophilic nature of P(AM-co-SA) also posts challenges for the 2nd network formation. P(AM-co-SA) gels obtained with 2.5M monomer solution can swell to 16 times of their original size. Another challenge of using P(AM-co-SA) as the 1st network is the solubility limitation of SA. At 2.5M total 1st network comonomer concentration, we almost reach the limit of the comonomers. It is difficult to obtain designed features in 3D printing using diluted solutions, because of the fast diffusion of radicals diffusing out of the 3D printing voxels.

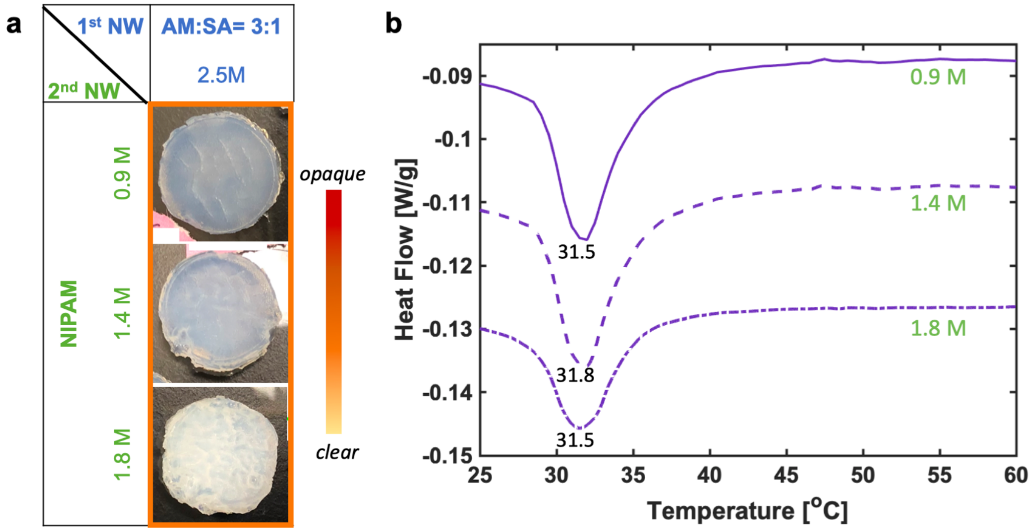

Figure D.3: Investigation of a) P(AM-co-SA)/PNIPAM IPNs using b) DSC of PAM/PNIPAM IPNs. In the 1st network (AM-co-SA) formulation, the total comonomer concentration is 2.5 M with the mole ratio of AM:SA = 3:1.

Appendix E

UV DOSAGE COMPARISON BETWEEN EMBER AND ELEGOO 3D PRINTERS

Table E.1 shows the comparisons we have made when choosing an additional 3D printer to complement the Ember 3D printer. Ultimately, because of the large build volume, competitive price and similarity of x, y, z resolution and wavelength of light source to Ember, we decided to use the ELEGOO printer to fabricate the MPEC samples.

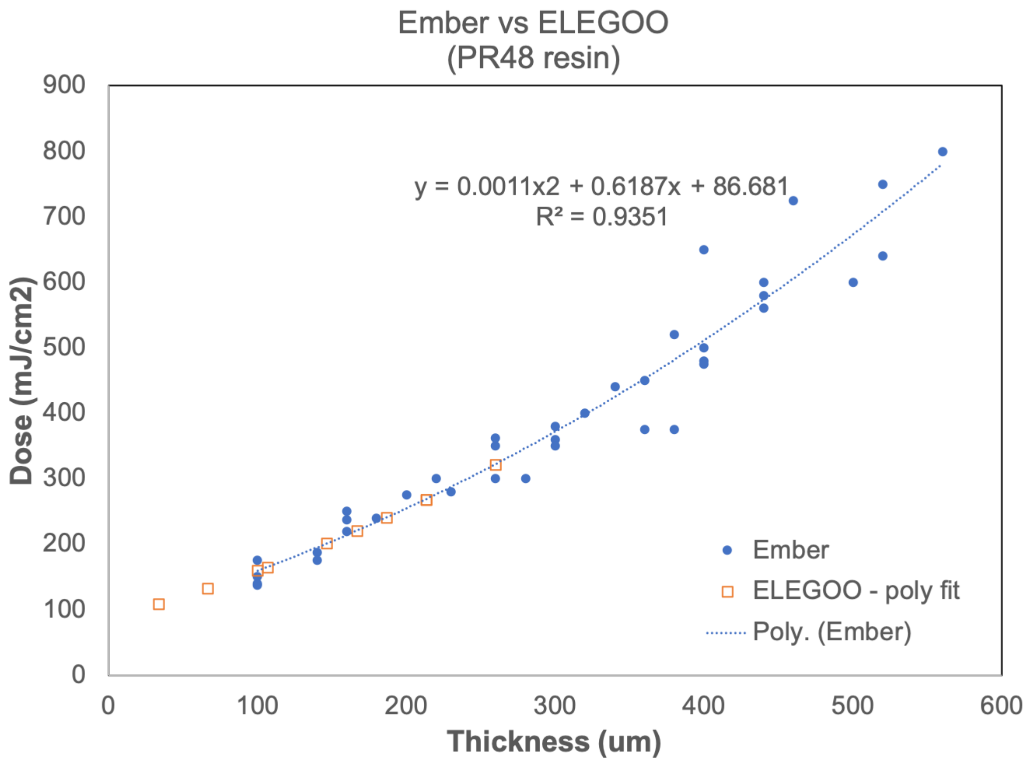

Figure E.1: Working curve for Ember 3D printer to determine exposure of ELEGOO using PR48 photoresin. y is the dosage and x is the measured thickness.

During the resin development process, we discovered that the curing time of ELEGOO is a magnitude longer than that of the Ember printer. To better compare the two printing systems, we plotted a working curve, a characterization known by the 3D printing community, using Ember 3DP printer and the standard clear PR48 resin, shown in Figure E.1. We assume that the irradiance of Ember is consistent at

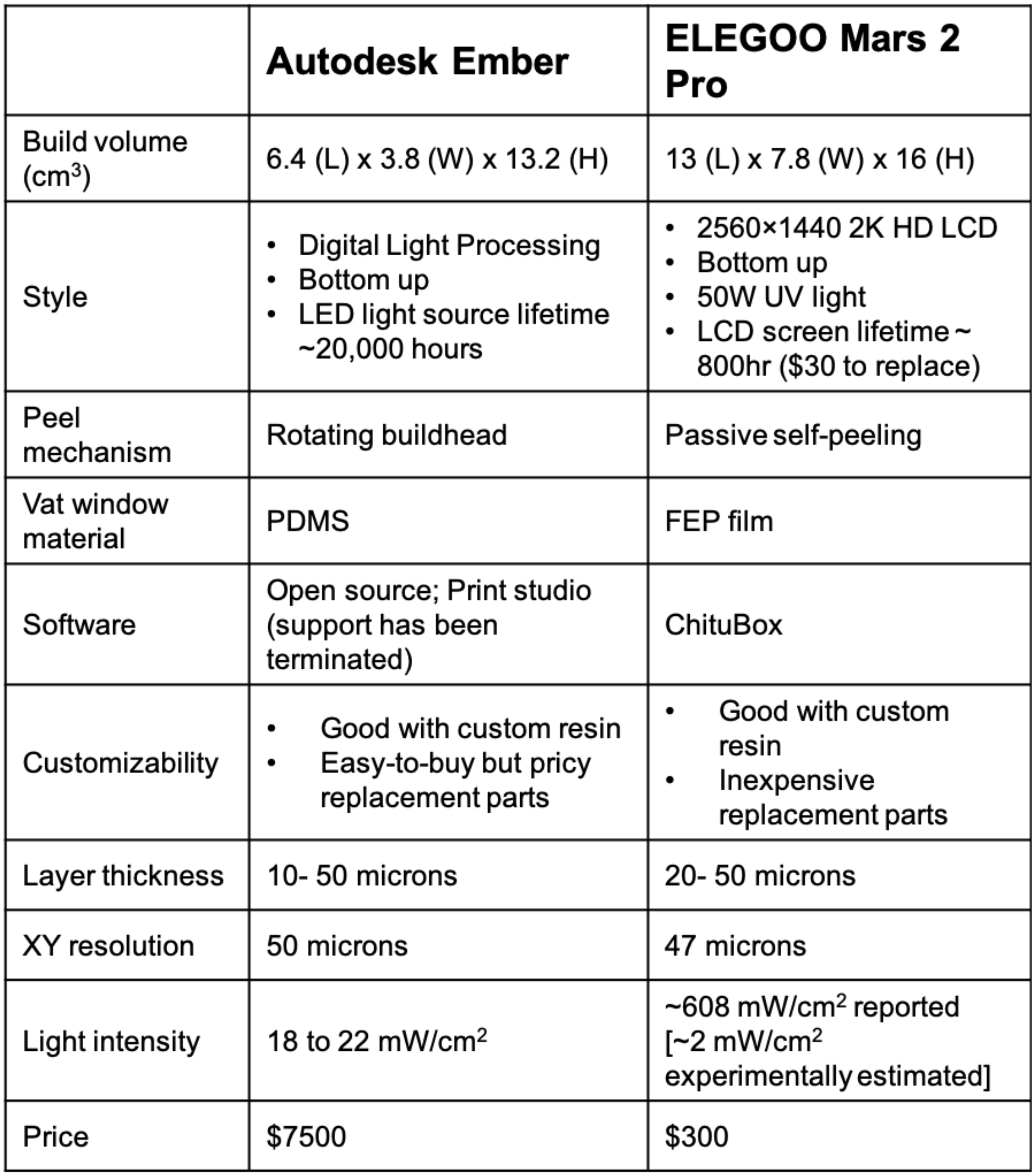

	Autodesk Ember	**ELEGOO Mars 2 Pro**
Build volume (cm^3)	6.4 (L) x 3.8 (W) x 13.2 (H)	13 (L) x 7.8 (W) x 16 (H)
Style	• Digital Light Processing • Bottom up • LED light source lifetime ~20,000 hours	• 2560×1440 2K HD LCD • Bottom up • 50W UV light • LCD screen lifetime ~ 800hr ($30 to replace)
Peel mechanism	Rotating buildhead	Passive self-peeling
Vat window material	PDMS	FEP film
Software	Open source; Print studio (support has been terminated)	ChituBox
Customizability	• Good with custom resin • Easy-to-buy but pricy replacement parts	• Good with custom resin • Inexpensive replacement parts
Layer thickness	10- 50 microns	20- 50 microns
XY resolution	50 microns	47 microns
Light intensity	18 to 22 mW/cm^2	~608 mW/cm^2 reported [~2 mW/cm^2 experimentally estimated]
Price	$7500	$300

Table E.1: Comparison between Ember and ELEGOO 3D printers.

25 mW/cm^2, which is the value provided by the manufacturer. The working curve characterization is simple. First, we generate a CAD file with square patterns and randomly sign different layer number (N) to each square. Second, we upload the CAD file to the printer and set an exposure time per layer (t), then the PR48 resin is poured onto the vat window. XX and completed the exposure of the square pattern with the rotation mechanism turned off and without a buildhead attached. This is known as a window print. The location of the square patterns are chosen randomly on the projection screen of PμSL printer to avoid any biases. We then measured

the thickness of each square pattern with known amount of dosage, which can be calculated as

$$Dosage = I \cdot N \cdot t \tag{E.1}$$

where dosage in the unit of mJ$\cdot cm^{-2}$. By plotting the calculated dosage and the measured thickness of the cured PR48 at each location on the square pattern, a working curve can be fitted to be a polynomial, as shown in Figure E.1. Then, perform the same experiment with the square pattern print file using ELEGOO. From entering the thickness values obtained using ELEGOO we can back calculate the irradiance of the printer, which is found to be 2.41 ± 0.07 mJ$\cdot cm^{-2}$. This irradiance value is 250 times less than the value calculated using the LED voltage and the LCD display area provided on the company website, 608 mW/cm^2, which explains the reason that we need to dramatically increase the exposure time for the same resin to print in ELEGOO. Although, the printing set up to obtain these measurement via a window print differ from the normal printing process, it still provide us a rough estimate for the exposure per layer that is needed for a particular resin, which is very useful metric during resin development.